Photon asymmetry of the $\overrightarrow{\gamma}p \rightarrow \pi^+ n$ reaction in the region of the $\Delta(1232)$ resonance

Richard F. B. Codling

Master of Science by Research

Nuclear Physics Experimental Research Group

Department of Physics and Astronomy

University of Glasgow

> "But there was one Elephant – a new Elephant – an Elephant's Child – who was full of 'satiable curtiosity, and that means he asked ever so many questions..."
>
> Rudyard Kipling, 'The Elephant's Child' from 'The Just-So Stories'.

This thesis is dedicated to my mother in recognition of the unwavering efforts she made in bringing me up to be a responsible member of society.

And for everyone who asked, "When will it be finished?": here it is...

Abstract

The photon asymmetry, Σ, of the $\overrightarrow{\gamma}p \rightarrow \pi^+ n$ reaction was measured for incident linearly polarised photons with coherent peak energies of 400 and 440 MeV, corresponding to the upper region of the $\Delta^+(1232)$ resonance. The measurements show the energy and angular dependence of Σ over the range $30^\circ < \theta_{\pi^+} < 170^\circ$ in the Centre of Mass frame in five bins of varying width. Each of these $\theta_{\pi^+}^{CM}$ bins is subdivided into five E_γ bins over the 100 MeV range up to the coherent peak energy, each E_γ bin having a width of 20 MeV. This gave some overlap between the two experimental data sets which thus allowed for comparisons to be made between them for the expected internal consistency of the experiment.

The measurements were made as part of the A2 collaboration's photo-nuclear research programme using the Glasgow tagged photon spectrometer in conjunction with the CB and TAPS detectors at the MAMI-B electron beam facility. Data was collected between July and October 2004 and yielded approximately 130 hours of data for the 400 MeV data set and 460 hours for the 440 MeV data set.

The presented experimental results for Σ will eventually provide additional data points for the MAID and SAID databases used to test and consolidate current photo-production models and fits in a currently sparsely populated experimental data region. In addition, this first round of experiments with the CB and TAPS detectors represents the first use of the CB for the detection of charged pions. This has applications for future experiments at MAMI involving the measurement of polarisation observables relying on charged-meson final states. The output of the newly upgraded GEANT-4 simulation of the apparatus setup in A2 was also compared to the experimental results for consistency.

Declaration

The data presented in this thesis was collected as part of the first round of experiments with the CB and TAPS detectors performed by the A2 collaboration based at the Intituit Für Kernphysik at the Johannes Gutenberg Universität in Mainz, Germany. I participated fully in the setup and data collection phases of the experiment where appropriate. The analysis of the experimental data presented was performed by myself at the University of Glasgow, as was the writing of this thesis.

Richard F. B. Codling, August 2008

Contents

List of Figures

List of Tables

Chapter 1

Introduction and Background

Over the last hundred years, the field of sub-atomic Physics has grown rapidly from its beginnings in the realm of inorganic Chemistry into modern High Energy Physics. This is a broad field of which Nuclear Physics, while highly diverse in its own right, is but a small part. Nuclear Physics is concerned with Strong Force interactions described by the Standard Model of Particle Physics.

1.1 The Standard Model and Nuclear Physics

The Standard Model of Partcle Physics describes the composition, structure and behaviour of sub-atomic matter and is based on experimental observations. It requires the existence of two families of particles; fermions and bosons. The former contains both the six flavours of quark: up, down, strange, charm, bottom and top, and the three leptons: electrons, muons, tauons and their associated neutrinos - Fig. 1.1. Fermions are characterised by the fact they all have half-integral spin. Bosonic particles are the 'force carriers' of each of the fundamental interactions - Strong, Weak, Electro-Magnetic and Gravitational - and have integral spin. Only the spin-1 interactions are included in the Standard Model, the gravitational interaction having no effect on a sub-atomic level (the as-yet undiscovered graviton is predicted to have a spin of 2). Nuclear, and specifically Hadron Physics, is concerned with only the subset of the Standard Model that deals with the strong interaction; the most powerful but shortest ranged fundamental force (Table 1.2). This force, mediated by the gluon, holds atomic nuclei

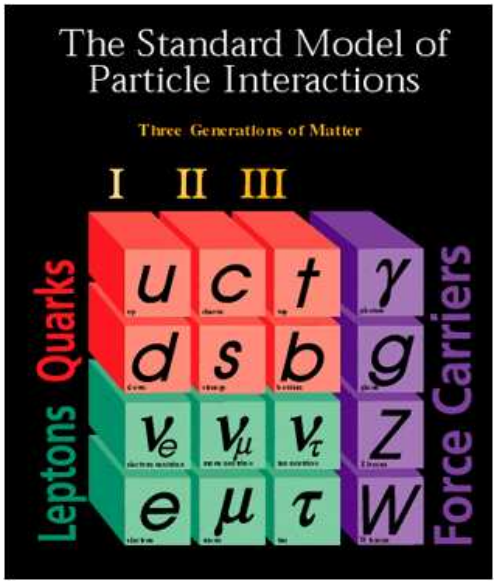

Figure 1.1: Diagram showing the fundamental entities described by the Standard Model.

Quark	Mass (MeV/c^2)	Charge (q_{e^-})
u	$1 \leq m_u \leq 4$	$+\frac{2}{3}$
d	$4 \leq m_d \leq 8$	$-\frac{1}{3}$
s	$80 \leq m_s \leq 130$	$-\frac{1}{3}$
c	$1.15 \times 10^3 \leq m_c \leq 8 \times 10^3$	$+\frac{2}{3}$
b	$4.1 \times 10^3 \leq m_b \leq 4.4 \times 10^3$	$-\frac{1}{3}$
t	$(174.3 \pm 5.1) \times 10^3$	$+\frac{2}{3}$

Table 1.1: The masses and charges of the six flavours of quark. Their associated anti-quarks have the same mass but exactly opposite quantum numbers.
Information from [1].

Interaction	Relative Strength	Range (m)	Exchange Boson
Strong	1	10^{-15}	Gluon
Electro-magnetic	10^{-2}	∞	Photon
Weak	10^{-5}	10^{-18}	Z^0, $W^{\pm}$
Gravitational	10^{-38}	∞	Graviton

Table 1.2: A comparison of the four fundamental forces of nature.

Meson	Quark Content	Mass $(/MeV/c^2)$	Baryon	Quark Content	Mass $(/MeV/c^2)$
π^0	$u\bar{u}$ or dd	134.977	p	uud	938.272
π^+	ud	139.570	n	udd	939.565
π^-	$d\bar{u}$	139.570	Λ^0	uds	1115.68
η	$d\bar{u}$	547.750	Σ^0	uds	1192.64
K_0	$d\bar{s}$	497.648	Σ^+	uus	1189.37
$\overline{K}_0$	$s\bar{d}$	497.648	Σ^-	dds	1197.45
K^+	$u\bar{s}$	493.677	Ξ^0	uss	1314.83
K^-	$s\bar{u}$	493.677	Ξ^-	dss	1321.31

Table 1.3: Summaries of the ground state octets of the Hadrons containing first generation quarks. Those containing strange quarks are generally referred to as hyperons, whereas those containing no s quarks are the nucleons.
Information from [1].

together and confines quarks to their baryonic and mesonic bound states. Baryons are comprised of three quarks: qqq and the lightest of these is the proton, composed of two 'up' quarks and one 'down' quark: uud. Mesons consist of quark - anti-quark pairs - $q\bar{q}$ - the lightest of these being the π^0: $u\bar{u}$ or $d\bar{d}$. The full sets of baryons and mesons are illustrated in Table 1.1, their quark content and masses (in MeV/c^2) being given. One of the first questions that should arise from the perusal of Tables 1.1 and 1.1 is that of the mass anomaly; the fact that the mass of any given Hadron cannot be wholly accounted for by simply summing the masses of the quarks seen to be its constituents. This is a major challenge in the understanding and modelling of nucleon structure. In order to address it, one needs to look further at the internal structure and dynamics of the nucleon.

1.1.1 QCD-Based Hadronic Models

Quantum Chromo-Dynamics is the theory of the strong force. QCD allows certain combinations of bound states to be produced in particle reactions provided that certain rules are adhered to; energy, charge, baryon number for example must be conserved. It also requires that bound states are colour neutral when viewed externally.

QCD cannot be solved at hadronic distance scales - perturbative treatment is impossible as the force at a range of $d \sim$ 1fm is so great - one has to find effective interactions and effective degrees of freedom which can predict accurately the properties of hadrons. Currently there are a plethora of QCD-inspired hadronic-structure models, all of which have limited applicability. These models are assessed on their ability to predict experimental observables. For example, the excitation spectrum

of a nucleon is a basic manifestation of its structure and, therefore, any worthwhile model must yield accurate predictions of that spectrum and of the properties of any excited states associated with it.

1.2 Nucleon Resonances

It is worth saying a few words at this stage about the Baryon resonance that is present in the energy range in which the $\overrightarrow{\gamma}p \rightarrow \pi^+ n$ experiment was performed. The incident photon energies of between 300 and 440 MeV used in the experiment correspond to some of those capable of exciting the proton from its ground state into a $\Delta(1232)$, its first resonance state. The experiment was run in parallel with one to measure $\overrightarrow{\gamma}p \rightarrow \pi^0 p$, the analysis of which is not covered here. Each of these channels has somewhat different resonant and non-resonant contributions to the reaction amplitude and thus makes investigating both channels a worthwhile task. These differing contributions are discussed further in Section 3.2.2.

The Baryon Decuplet is the set of resonances that can be produced by exciting any member of the Baryon Octet (the set of ground-state Baryons) into a resonant state. Both the Baryon Octet and Decuplet are shown in Fig. 1.2, which also gives some other information about these states.

Baryon resonances are predicted by QCD, specifically constituent quark models, and are the result of excitation by some incident entity; experimentally a photon, electron or pion beam which affects the quarks that comprise the baryon. We cannot split the nucleon - QCD prevents us from seeing its constituents in isolation - and so we must glean information about its structure by the investigation of its resonant properties; how it behaves when we excite it using some form of stimulus in the form of an experimental probe. Observing the excitation spectrum of a Baryon allows the practical testing of predictive models, which in turn can be used to refine these models. The first of the Baryon resonances to be observed after its initial existence was predicted was the $\Delta(1232)$ state. It remains an interesting proposition for experimental study because it possesses some unique features and properties, which are outlined below.

The $\Delta(1232)$, also referred to as the $P_{33}(1232)$, is the first nucleon excited state and the lightest member of the baryon Decuplet. Depending on the target material and incident particle, four charge states are possible, illustrated in the bottom plot of figure 1.2. Whatever the charge, each Δ has similar basic

properties; a lifetime of around 10^{-24}s and thus a large Breit-Wigner with: $\Gamma \sim 120$MeV at FWHM. The Δ^+ can be viewed, in terms of 'naive' quark models, as having the same quark configuration as the proton (the described experiment was performed with hydrogen as the target material), but with the spin of the constituent d quark effectively flipped, giving the resonance an overall spin of $\frac{3}{2}$, whereas the proton has the overall spin of $\frac{1}{2}$. Mass separations for the states depicted in Fig. 1.2 are approximately 125 to 250 MeV for the Baryon Octet and 150 MeV for the Decuplet, as Y decreases. As can be seen in Fig. 1.2, the $\Delta(1232)$ is isolated from other baryon resonances, its peak at 1232 MeV is below the production threshold for the other resonances. As such, experiments can be performed in the region of the Δ resonance with relatively little interference from the effects of higher energy resonance states.

1.3 Phenomenological Analyses of Experimental Data

All the theory in existence is no good if real-world observations do not match these predictions. To this end, there are various fits that can be made to experimental data to check and refine the accuracy of the motivating theory. Pion photo-production measurements (the subject matter of this work) have been analysed in terms of 'Effective Lagrangian' (MAID) or 'Partial-Wave Analysis' (SAID) approaches. The parameters in each are adjusted and thus phenomenology can then guide more fundamental treatments.

MAID and SAID agree fairly well with their fits to pion production data from threshold, but start to differ as incident gamma energies approach 1 GeV. This however is well above the energy range being investigated for the purpose of the analysis being presented here, and so comparing experimental findings to both MAID and SAID should be a valuable exercise in this instance.

1.3.1 MAID

With expertise based in Mainz at the Johannes Gutenberg Universität [4], MAID [5] is a Unitary Isobar Model taking into account the various nucleon resonances produced by both real and virtual photons, vector meson and non-resonant Born terms up to 1GeV. The influence of individual resonances may

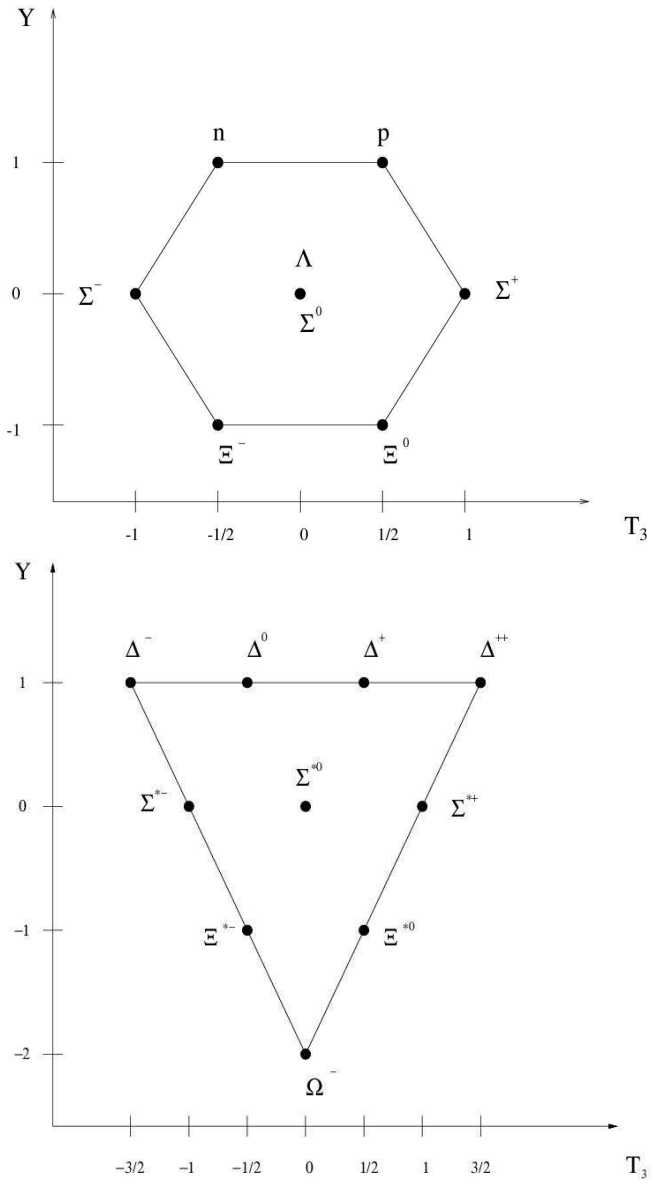

Figure 1.2: The Baryon Octet (ground states, top) and Decuplet (excited states, bottom). These are represented on a Cartesian plane of hyper-charge, Y, versus Isospin, I_3, where $Y = B + S$ (baryon number plus strangeness) and $I_3 = Q - \frac{Y}{2}$ (total charge minus half of the hyper-charge).

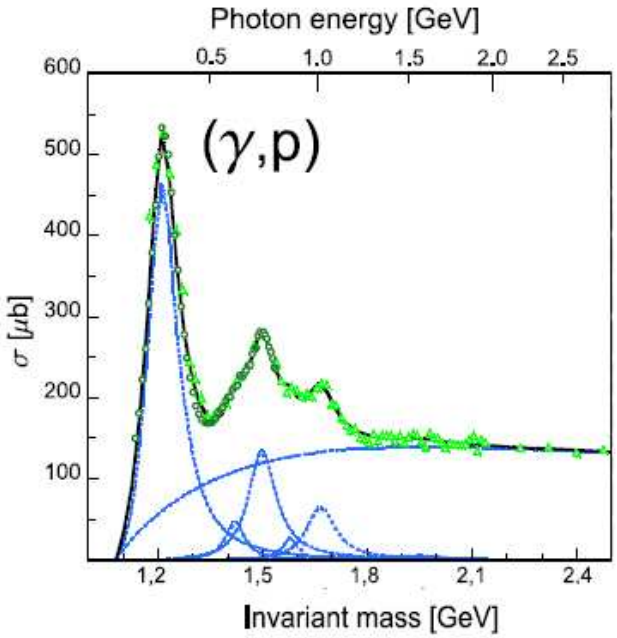

Figure 1.3: A plot of the total Hadronic Photo-absorption cross-section on the proton. The blue lines show the relative contributions of the (l to r) $P_{33}(1232)$, $P_{11}(1440)$, $D_{13}(1520)$, $S_{11}(1535)$ and $F_{15}(1680)$ resonances and an estimated background. From [2] and [3].

be fitted to the data or manipulated by hand, thus making MAID a comprehensive model with which to fit a wide range of experimental data.

1.3.2 SAID

SAID [6], c/o the Center for Nuclear Studies (CNS) at the George Washington University's Virginia Campus [7], is an example of a so-called 'Partial Wave Analysis' (PWA). The idea of performing this type of analysis is to extract scattering amplitudes from experimental data at incident photon energies of up to a few GeV. The phrase 'partial wave' refers to the fact that it is the particle's wave functions that are expanded, by parameterising them with complex amplitudes. It should be noted that, in most cases, reaction dependent assumptions must be made, due to the fact that information extracted from fits to data can be ambiguous, and so any output from a PWA should be used as a guide to the overall shape of an expected distribution rather than for absolute quantification. In this way, PWA is a good example of an ongoing effort as each new experiment contributes more data to the fits, meaning that as time goes by, the predictions made by databases such as SAID become more and more accurate. PWA techniques require fitting to high statistics angular distributions and so performing experiments

with large solid-angle detectors is important. The CB@MAMI detector setup, as used in this work, provides this facility and so the data produced will be of great value in refining SAID.

1.4 Electro-Magnetic (EM) Probes

In Nuclear Physics experiments, the aim is often to investigate the internal properties of the target material and to do this a suitable experimental probe must be chosen. In this case an EM probe - an electron or real photon - is used. This is because their interaction is extremely well understood, being wholly governed by QED. EM probes have the ability to probe the entire volume of the atomic nucleus and are therefore ideal for investigating deep internal features of both nuclei and individual nucleons. However, making accurate measurements on this scale is difficult as the cross-sections for these reactions are small, of the order of tens of nanobarns (nb, where 1nb = 10^{-28}m^2).

Using high luminosity, high duty-factor photon and electron beams, many previously inaccessible reaction channels may be investigated quantitatively. This is especially true for polarisation observables which are crucial to unravelling the nucleon's excitation spectrum. Reference [8] gives a comprehensive general introduction to the topic of the use of EM probes.

1.4.1 A Question of Scale

When choosing the most suitable EM probe with which to perform any given experiment, the types of quantities that can be accessed by each of the two types of EM probe need to be considered. Electron scattering experiments, for example, let internal features of nuclei be investigated; radii, form factors and matter distributions, whereas quark or nucleon interactions are better investigated using real photons. The experiment described herein used real photons as the experimental probe.

Coupled with the fact that a gamma ray interacts weakly with a nuclear target, the energy of a real photon dictates what level of spatial resolution can be achieved. An atom in its ground state can be probed using photons with $E_\gamma \sim$ few eV; ground state nuclei require $E_\gamma \sim$ few MeV, while looking at the internal structure of an individual nucleon requires $E_\gamma \sim 10^{-1}$ GeV. Roughly speaking, there is an inverse relationship between the energy of the probing photon and the size of the entity being

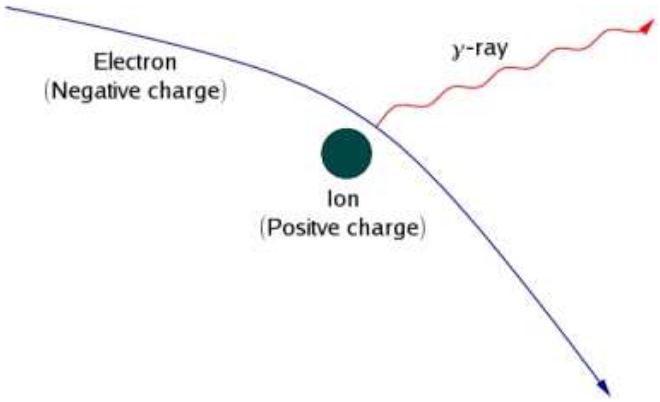

Figure 1.4: The process responsible for producing Bremsstrahlung photons.

investigated: a nucleon is $\sim 10^{-15}$m across whilst an atom is 10^5 times larger than this, having a diameter of the order of 10^{-10} m.

1.4.2 Real Photon Production

The experiments performed by the A2 Collaboration use real photons as the experimental probe, employing the Glasgow photon tagging spectrometer to energy-tag Bremsstrahlung radiation. Real photons can be produced using a variety of techniques. These techniques are presented below in chronological order of their development and use in Nuclear Physics experiments.

1.4.2.1 Bremsstrahlung

Bremsstrahlung, or 'breaking radiation' is produced when an electron decelerates in the field of a nucleus, emitting electromagnetic radiation in the form of a photon in order to conserve energy and momentum. The now reduced-energy electron is left to continue onwards on a trajectory slightly deviated from its original path. The basic process is illustrated in figure 1.4, while a typical Bremsstrahlung spectrum is shown in figure 1.5. It should be noted that the highest cross-section for Bremsstrahlung production is as the low photon energy end of the spectrum - this becomes important when using energy-tagged Bremsstrahlung photons as experimental probes.

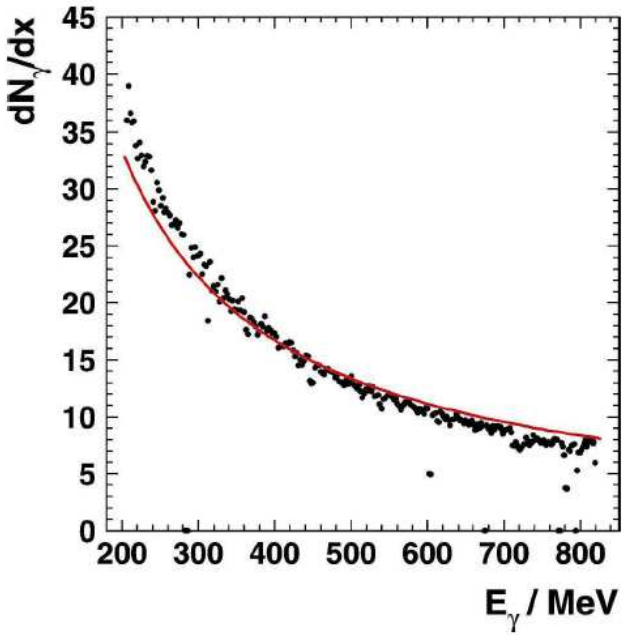

Figure 1.5: A typical Bremsstrahlung photon energy spectrum from the MAMI-B electron beam. Photons are energy-tagged by the Glasgow tagger.

1.4.2.2 Tagged Photons

Energy tagging Bremsstrahlung photons produces quasi-mono-energetic beams of particles. The procedure was first suggested in the 1950s with the aim of performing accurate photo-production experiments. Photon tagging techniques have developed steadily to the point where there are now several laboratories worldwide including these types of experiments in their Physics programmes. Current examples of facilities conducting this kind of research are MAMI (Mainz, Germany), ELSA (Bonn, Germany), MAX-lab (Lund, Sweden), KEK (Tsukuba, Japan), SPring-8 (Aioi, Japan) and Jefferson Laboratory (Newport News, USA) to name a few. Each facility generally adds its own uniqueness to the world's data set for any particular reaction or physical process, be it differing beam-energy ranges, angular acceptances etc. A comprehensive introduction to Photon Tagging is given in [9].

By measuring the energy of the scattered electrons, one can determine the energy of the associated photon if the incident beam energy is known. To do this, a magnetic spectrometer is used to bend the electrons after they encounter a radiating material. Electrons that have interacted with the radiator will have lost some of their energy - having had to impart some momentum to the material in order to produce a Bremsstrahlung photon - and so will be deflected more than electrons which have not

undergone an interaction. By observing the positions at which energy degraded electrons leave the field of the deflecting magnet, their energies can be calculated and thus the energies of the associated Bremsstrahlung photons can be deduced. It is this process that is known as Photon Tagging.

The apparatus required for photon tagging comes in two parts, a magnetic spectrometer to bend the electrons, and a focal plane detector placed just outside the magnet to determine the position at which an electron strikes it. This is fully described in section 4.3, which discusses the actual Tagger used in experiments in the A2 collaboration in Mainz.

1.4.2.3 Polarised Photons

The experiment was performed using linearly polarised photons which can be produced in two different ways: utilising the Coherent Bremsstrahlung method or by Compton Backscattering from a polarised laser. Both of these are outlined below, the Coherent Bremsstrahlung being the process employed for the experiment presented here.

Coherent Bremsstrahlung. While being fully discussed in section 4.4, it is fitting to compare and contrast this method of polarised photon production with others here. Coherent Bremsstrahlung photon beams are produced by scattering from crystals. By carefully adjusting the orientation of the crystal planes relative to the incident electron beam it is possible to make use of the crystal structure to greatly enhance the Bremsstrahlung cross-section at discrete values of momentum transfer which correspond to the reciprocal lattice vectors of the crystal. This produces polarised photons. Originally observed at energies of around 200MeV, it was subsequently noticed that the effect could be observed down to electron energies of as low as 35 keV. Reference [10] describes the general principles of producing coherent bremsstrahlung at these kinds of energies, with reference to then-available experimental data.

Compton (Laser) Backscattering. The scattering of polarised laser light from high-energy electrons ($E_{e^-} > 1$GeV) can produce highly polarised photon beams ($\sim$99%) with energies of the order of hundreds of MeV with resolutions of a few percent. They are produced by illuminating an electron beam head-on with a laser, the actual energy of the resultant photons being dependent on both the

electron energy and the wavelength of the laser light. The polarisation of the laser is transferred to the photon beam with very high efficiency and tagging is performed by measuring the scattered electron energy. Another advantage of γ beams produced in this way is that they tend to have low background contributions from effects such as interactions with pumping fluids in the vacuum chamber ($\sim$1%) and low energy x-rays produced by synchrotron radiation which, while not inducing spurious reactions, will cause experimental apparatus to accrue radiation damage. These effects will however be negligible at a well-designed facility. One major disadvantage of beams produced by Compton Backscattering is that their intensity is much lower, of the order of 10^3 less than those produced by Bremsstrahlung. Reference [11] offers a brief history of Compton Backscattered photon beam generation, outlining their production and use in Nuclear Physics experiments.

1.5 Experimental Observables

In all branches of Physics the information required from an experiment is not usually directly accessible. For example, when J.J. Thomson performed his famous e/m experiments he inferred his results from readings of the currents and voltages being applied to his equipment, calculating his electric and magnetic field strengths from the geometries of his apparatus setup. Similarly, in Nuclear Physics, any of the so-called 'observables': cross-section, Photo- or Electro- absorption, Asymmetry etc. are subsequently deduced from the resulting distributions of reaction products in terms of quantity, energy, or angle of emission. From these measurements, actual physical processes can be isolated and their effects quantified. The physics measurement this thesis is based on is an asymmetry, which belongs to the group of observables that relies on one of the experimental entities being polarised in some way.

1.5.1 Polarisation Observables

There are several types of polarisation observable accessible at the Glasgow/Mainz tagged photon facility. Any, some, or all of which can be used to produce an asymmetry measurement: beam, target, reaction products. If certain combinations are measured, a so-called 'complete' measurement can be made [12]. The phrase 'complete experiment' refers to having the required number (three) of double polarisation measurements to complement the information gleaned from single polarisation

Symbol	Transversity representation	Experiment required	Type
$d\sigma/dt$	$\|b_1\|^2 + \|b_2\|^2 + \|b_3\|^2 + \|b_4\|^2$	$\{-;-;-\}$	S
$\Sigma d\sigma/dt$	$\|b_1\|^2 + \|b_2\|^2 - \|b_3\|^2 - \|b_4\|^2$	$\{L(\frac{1}{2}\pi, 0); -; -\}$	
$T d\sigma/dt$	$\|b_1\|^2 - \|b_2\|^2 - \|b_3\|^2 + \|b_4\|^2$	$\{-; y; -\}$	
$P d\sigma/dt$	$\|b_1\|^2 - \|b_2\|^2 + \|b_3\|^2 - \|b_4\|^2$	$\{-; -; y\}$	
$G d\sigma/dt$	$2\ \mathrm{Im}(\mathrm{b_1 b_3^* + b_2 b_4^*})$	$\{L(\pm\frac{1}{4}\pi); z; -\}$	BT
$H d\sigma/dt$	$-2\ \mathrm{Re}(\mathrm{b_1 b_3^* - b_2 b_4^*})$	$\{L(\pm\frac{1}{4}\pi); x; -\}$	
$E d\sigma/dt$	$-2\ \mathrm{Re}(\mathrm{b_1 b_3^* + b_2 b_4^*})$	$\{C; z; -\}$	
$F d\sigma/dt$	$2\ \mathrm{Im}(\mathrm{b_1 b_3^* - b_2 b_4^*})$	$\{C; x; -\}$	
$O_x d\sigma/dt$	$-2\ \mathrm{Re}(\mathrm{b_1 b_4^* - b_2 b_3^*})$	$\{L(\pm\frac{1}{4}\pi); -; x'\}$	BR
$O_z d\sigma/dt$	$-2\ \mathrm{Im}(\mathrm{b_1 b_4^* + b_2 b_3^*})$	$\{L(\pm\frac{1}{4}\pi); -; z'\}$	
$C_x d\sigma/dt$	$2\ \mathrm{Im}(\mathrm{b_1 b_4^* - b_2 b_3^*})$	$\{C; -; x'\}$	
$C_z d\sigma/dt$	$-2\ \mathrm{Re}(\mathrm{b_1 b_4^* + b_2 b_3^*})$	$\{C; -; z'\}$	
$T_x d\sigma/dt$	$2\ \mathrm{Re}(\mathrm{b_1 b_2^* - b_3 b_4^*})$	$\{-; x; x'\}$	TR
$T_z d\sigma/dt$	$2\ \mathrm{Im}(\mathrm{b_1 b_2^* - b_3 b_4^*})$	$\{-; x; z'\}$	
$L_x d\sigma/dt$	$2\ \mathrm{Im}(\mathrm{b_1 b_2^* + b_3 b_4^*})$	$\{-; z; x'\}$	
$L_x d\sigma/dt$	$2\ \mathrm{Re}(\mathrm{b_1 b_2^* + b_3 b_4^*})$	$\{-; z; z'\}$	

Figure 1.6: Complete list of possible pseudo-scalar meson photo-production observables.

measurements. Some such 'complete' experiments are currently at the proposal stage. Figure 1.6 gives a full list of the observables that can be combined to make a 'complete measurement'.

A polarised photon beam is required to measure the photon beam asymmetry, Σ. Other observables - beam-target, target-recoil and beam-recoil - can be measured, but making these measurements would involve also knowing the polarisations of the target and outgoing reaction products. Double polarisation experiments are therefore harder to perform but ultimately can yield more information than just measuring single-polarisation observables. An asymmetry, *Asym.*, is defined as being the ratio of the difference in magnitude of two quantities, A and B, divided by their sum:

$$Asym. = \frac{A - B}{A + B} \tag{1.1}$$

In the case of the described experiment, the asymmetry is the photon beam asymmetry, Σ, and the quantities A and B are the cross-sections of the angular distributions of the emitted pion with respect to the two orthogonal polarisation orientations of the incident photons. Thus eqn. (1.1) becomes:

$$\Sigma = \frac{\sigma_{\parallel} - \sigma_{\perp}}{\sigma_{\parallel} + \sigma_{\perp}}. \tag{1.2}$$

The process of constructing this asymmetry from experimental data is rather more complicated and is described in full in section 5.4.4.

1.5.2 Why Measure Photon Asymmetries?

The photon asymmetry Σ is very sensitive to the internal mechanisms of a reaction. Photon asymmetries are measured as they can give access to interference terms not seen in measurements of other observables such as total cross-section or photo-absorption. These interferences manifest themselves as changes in the structure functions when comparing the unpolarised and polarised cross-sections, σ_0 and σ_{pol}, respectively. These differences can be observed by noting the angles of emission of the products from any given reaction and constructing the asymmetry between the cross-sections of the two orientation planes. In the case of linearly polarised photons as used in the described experiment, these planes are those parallel and perpendicular to the electric field vector of the incident photon beam. Together with measuring other polarisation observables, a complete understanding of any given reaction can be achieved.

Chapter 2

Motivation for This Experiment

Performing this measurement of Σ is advantageous as the experimental setup in Mainz gives access to angular and energy ranges over which data is currently sparse; many measurements have been made of $\overrightarrow{\gamma} + p \rightarrow p + \pi^0$ while relatively few have been made of $\overrightarrow{\gamma} + p \rightarrow n + \pi^+$. The energy ranges chosen for the described experiment - enhanced polarisation peaks situated at incident photon energies of 400 and 440 MeV - are in an energy region where where the upper tail of the $\Delta(1232)$ resonance just begins to overlap with the other, higher energy nucleon resonances. The detector setup - the CB and TAPS - gives almost complete coverage of the full solid angle which is advantageous

The angular ranges of most interest are where the photon asymmetry drops to zero, a phenomenon which occurs at upper and lower ranges of θ. θ is the angle between the emitted pion and the incident photon in the Centre of Mass frame, hereafter referred to as $\theta_{\pi^+}^{CM}$. The energy range that the experiment was performed in was also one of significant interest. Again, data in this region is sparse; there have been many experiments performed around the pion threshold and many performed around the two-pion threshold but not so many performed in the region where this work was based. It is intended to submit our results for inclusion in the World-wide database from which fits to data are made. It is hoped that our measurement will enable the increased accuracy of such fits in the future. Section 2.1 summarises the current status of measurements made of Σ for the $\overrightarrow{\gamma} p \rightarrow \pi^+ n$ reaction.

2.1 Previous Experimental Work

The majority of pion photo-production experimentation has focused on the neutral pion channel, the $\pi^0 + p$ final state. Historically this was to investigate the resonance terms that contribute to the total cross-sections of these reactions. This was understandable given the newness of this type of research and the desire to observe the resonances predicted by burgeoning theoretical advances: $\pi^0 + p$ was predicted to couple strongly to the resonance terms comprising its total cross-section. Neutral pion reactions are easily reconstructed using photon detectors as the proton missing mass is readily obtained from the highly efficient detection of the pion's two decay photons, whereas charged pions and neutrons are harder to detect using photon spectrometers. Asymmetry measurements require as large a solid angle coverage as possible in order to maximize the detector acceptance. Photon detectors tend to do be designed with this specification - another reason that $\pi^0 + p$ has been the reaction of choice in the past.

Investigating the $\pi^+ + n$ channel is instructive as it offers complementary information to that provided by $\pi^0 + p$ analysis as the charged-pion final state tends to couple to the non-resonant Born terms. As a result, performing the $\overrightarrow{\gamma} p \rightarrow \pi^+ n$ experiment in the region of the Δ resonance will mean that some insight is gained into what is happening underneath the spectral enhancement: analyses of both the $\pi^0 + p$ and $\pi^+ + n$ final states can be used to help unravel the reaction mechanisms. A handful of experiments to measure Σ for the $\overrightarrow{\gamma} p \rightarrow \pi^+ n$ reaction have been performed previously and as such, the most significant ones related to the areas of interest covered by the CB@MAMI energy and angular ranges are outlined below, in chronological order of their performance and analysis. Any notable run conditions have also been highlighted and commented upon. Their results are presented in Figure 2.1 for posterity.

- Taylor and Mozley's polarized Bremsstrahlung experiment at the Stanford Linear Accelerator (SLAC) [13] performed in 1960 used E_γ= 242, 296, 337 and 376 MeV, at $\theta_{\pi^+}^{CM}$= 90deg.
- Smith and Mozley's 1963 experiment [14] - also performed at SLAC - used polarised X-Rays at similar energies to those of Taylor; at E_γ= 227, 240, 342 and 373 MeV respectively. On this occasion however, three values of $\theta_{\pi^+}^{CM}$ were investigated: θ = 45, 90 and 135 degrees.
- Getman et al.'s experiment [15] was performed at the Kharkov 2 GeV electron linear accelerator in

1981 using coherent Bremsstrahlung. Their data analysis procedures required that only the pions were detected at energies and angles $280 < E_\gamma < 420$ MeV and $30^\circ < \theta_{\pi^+}^{CM} < 150^\circ$ respectively.

- An experiment using MAMI-B in 2000 with the DAPHNE detector [16] produced Σ for incident energies of $270 < E_\gamma < 420$ MeV and angles of $21^\circ < \theta_{\pi^+}^{CM} < 159^\circ$ [17]. The results of that experiment are reproduced here in full (Fig. 2.2) due to the fact that it was performed at the same facility as the current work.

- The most recent experiment of relevance to this work had its results published in 2001 and was performed by Blanpied et al. [18] using the LEGS facility at the Brookhaven National Laboratory in the USA. The experiment was designed to focus on $N \rightarrow \Delta$ transition effects. It utilised photons produced by backscattering laser light at energies of between 213 and 333 MeV at $60 < \theta_{\pi^+}^{CM} < 180$ degrees. The analysis primarily focussed on the reaction cross-sections with secondary emphasis on photon beam asymmetries.

2.2 Fits to Current Experimental Data

The current A2 experimental setup allows laboratory θ angles from around 5° to 157° to be investigated, substantially extending the experimental data both in terms of E_γ dependence and $\theta_{\pi^+}^{CM}$. Predictions for the expected variance of Σ with $\theta_{\pi^+}^{CM}$ at E_γ= 400 and 440 MeV - the polariastion peak energies used in the experiment - are shown in Figures 2.3 and 2.4. These come from the MAID and SAID models discussed in section 1.3.

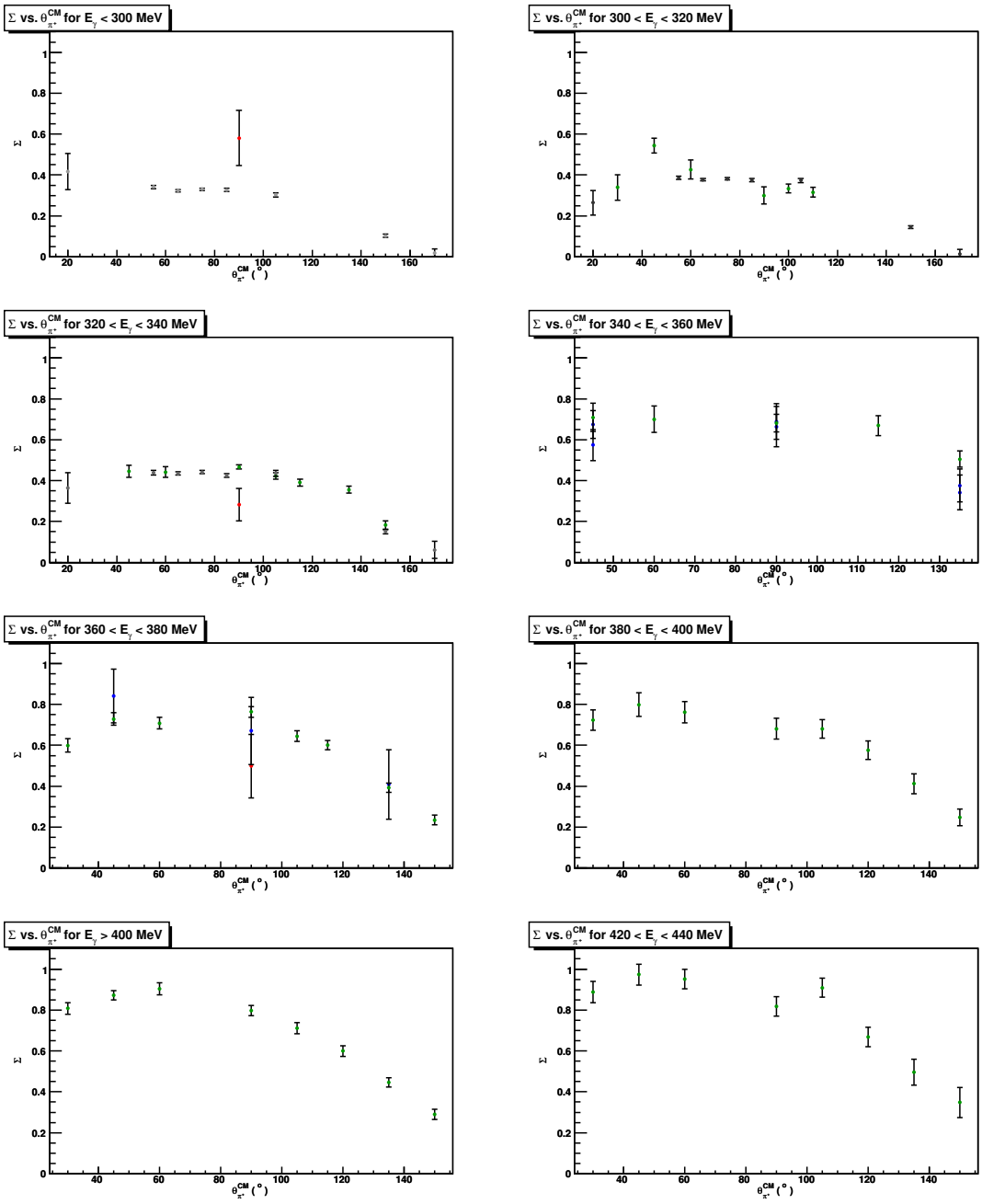

Figure 2.1: Plots showing previous results of Σ vs $\theta^{CM}_{\pi^+}$ for $p(\gamma,\pi^+)$ for various incident E_γ ranges. Data taken from [13] (red points), [14] (blue points), [15] (green points) and [18] (grey points). Different shades of a colour show different data sets from the same work.

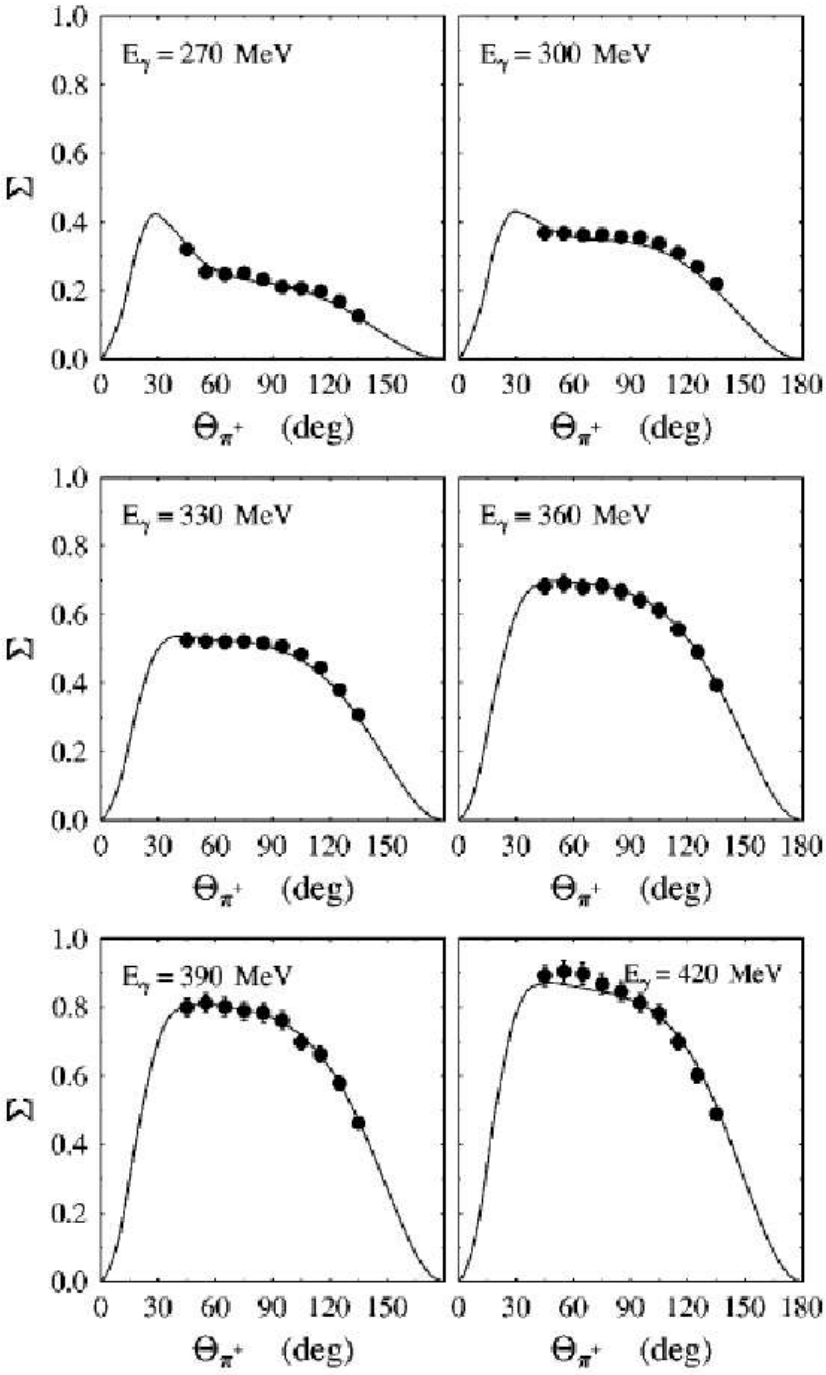

Figure 2.2: Plots showing Σ for $p(\gamma, \pi^+)$.
From [17].

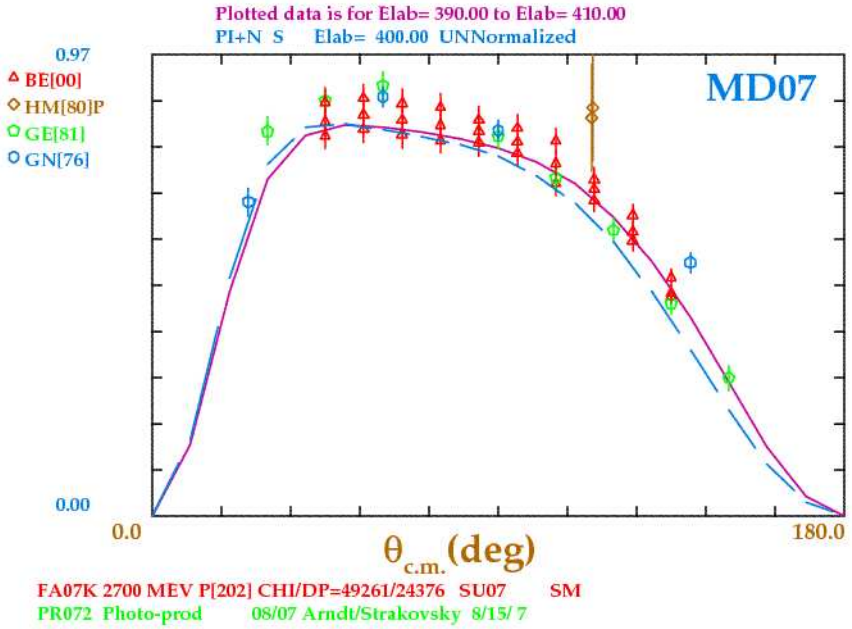

Figure 2.3: A fit to relevant experimental results showing Σ for $\theta_{pi^+}^{CM}$ in 10-degree increments at $E_\gamma = 400 \pm 10$ MeV. Fits are from the current solutions of both SAID (solid purple line) and MAID (dashed blue line).

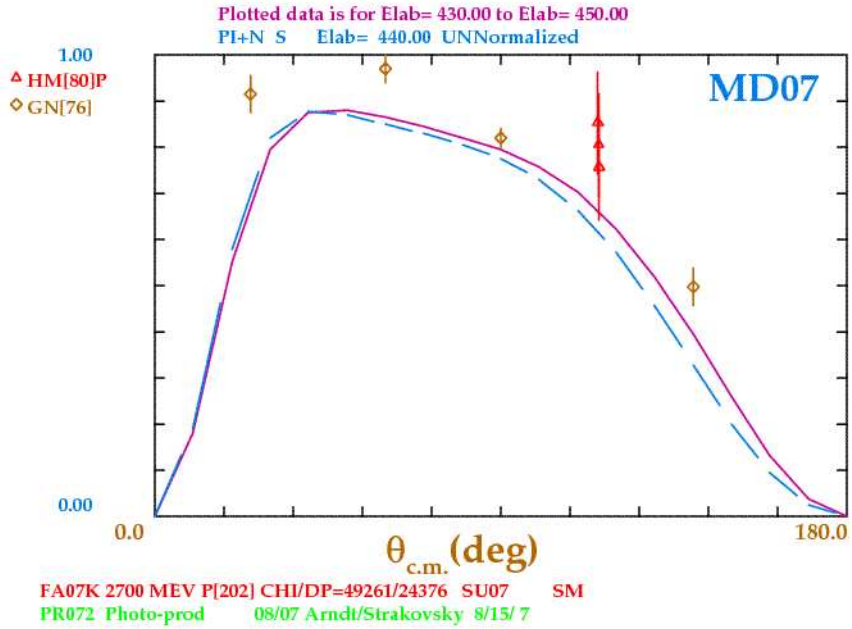

Figure 2.4: A fit to relevant experimental results showing Σ for $\theta_{pi^+}^{CM}$ in 10-degree increments at $E_\gamma = 440 \pm 10$ MeV. Fits are from the current solutions of both SAID (solid purple line) and MAID (dashed blue line).

Chapter 3

Contributing Processes in Pion Photo-production

3.1 Pion Photo-production

At the incident photon energies available at MAMI, possible directly observable single-pion final-state reactions - given a stationary proton target - are:

$$\gamma + p \rightarrow p + \pi^0 \tag{3.1}$$

$$\gamma + p \rightarrow n + \pi^+ \tag{3.2}$$

3.1.1 The Pion Threshold

The threshold for a real-photon induced pion production reaction is given - in natural units - by

$$E_{threshold} = \frac{E_{CM}^2 - m_{target}^2}{2m_{target}} \tag{3.3}$$

For the case of threshold pion photo-production on the proton $m_{target} = m_p$ and $E_{CM} = (m_{\pi^+} + m_n)$, thus giving

$$E_{threshold} = \frac{(m_{\pi^+} + m_n)^2 - m_p^2}{2m_p} \tag{3.4}$$

Eqn. 3.4 yields a value of $E_{threshold} = 151.4$ MeV for the $\gamma + p \rightarrow n + \pi^+$ reaction. For comparison, the value of $E_{threshold}$ for the $\gamma + p \rightarrow p + \pi^0$ reaction is 144.7 MeV, the lower value being due to the fact that $m_{\pi^+} > m_{\pi^0}$. A full treatment of the derivation of eqn. 3.4 is given in Appendix A.

3.2 Pion Photo-production Amplitudes

The total cross-section for pion production, in the CM frame is given by

$$\sigma_{tot.} = 4\pi \frac{|k|}{|q|}(A_0 + \frac{1}{3}A_1) \tag{3.5}$$

where A_0 and A_1 are contributions from the photo-production amplitudes given below, in equations (3.6) and (3.7):

$$A_0 = |E_{0+}|^2 + \frac{1}{2}|2M_{1+} + M_{1-}|^2 + \frac{1}{2}|3E_{1+} - M_{1+} + M_{1-}|^2 \tag{3.6}$$

$$A_1 = 2Re[E_{0+}^*(3E_{1+} + M_{1+} - M_{1-})] \tag{3.7}$$

Equations (3.5) to (3.7) relate $\sigma_{tot.}$to the Electric and Magnetic multipole amplitudes associated with pion production on the nucleon - see section 9.2 of [19]. The notation associated with the E and M multipoles, X_{lj}, relates to the following: X is the type of multipole, Electric or Magnetic (E or M); l is the angular momentum associated with the multipole and $j = \pm$ denotes the total spin of the πN system and is equal to $l \pm \frac{1}{2}$. In the energy range in question, the multipole contributions can be summarised as being the Electric dipole s- and d-waves - the former being dominant - and the Magnetic p-wave and resonance (Δ) terms. Electric quadrupole contributions are small enough to be considered negligible (Sec. 8.2 of [20]). Given this, the total unpolarised cross-section is given by the following approximation:

$$\sigma_{tot.} = 4\pi \frac{|\mathbf{q}|}{|\omega|}[|E_{0+}|^2 + 2|M_{1+}|^2 + |M_{1-}|^2] \tag{3.8}$$

with $\omega = E_\gamma$ and $\mathbf{q} = m_\pi \mathbf{v}_\pi$.

photon M-pole	initial state (L^P_γ, J^P_N)	interm. state $J^P_{N^\star}$	final state (J^P_N, L^P_η)	multi-pole	$(k^\star/q^\star)d\sigma/d\Omega$
E1	$(1^-,\frac{1}{2}^+)$	$\frac{1}{2}^-$	$(\frac{1}{2}^+,0^-)$	E_{o+}	$\lvert E_{o+}\rvert^2$
		$\frac{3}{2}^-$	$(\frac{1}{2}^+,2^-)$	E_{2-}	$\frac{1}{2}\lvert E_{2-}\rvert^2(5-3x^2)$
M1	$(1^+,\frac{1}{2}^+)$	$\frac{1}{2}^+$	$(\frac{1}{2}^+,1^+)$	M_{1-}	$\lvert M_{1-}\rvert^2$
		$\frac{3}{2}^+$	$(\frac{1}{2}^+,1^+)$	M_{1+}	$\frac{1}{2}\lvert M_{1+}\rvert^2(5-3x^2)$
E2	$(2^+,\frac{1}{2}^+)$	$\frac{3}{2}^+$	$(\frac{1}{2}^+,1^+)$	E_{1+}	$\frac{9}{2}\lvert E_{1+}\rvert^2(1+x^2)$
		$\frac{5}{2}^+$	$(\frac{1}{2}^+,3^+)$	E_{3-}	$\frac{9}{2}\lvert E_{3-}\rvert^2(1+6x^2-5x^4)$
M2	$(2^-,\frac{1}{2}^+)$	$\frac{3}{2}^-$	$(\frac{1}{2}^+,2^-)$	M_{2-}	$\frac{9}{2}\lvert M_{2-}\rvert^2(1+x^2)$
		$\frac{5}{2}^-$	$(\frac{1}{2}^+,2^-)$	M_{2+}	$\frac{9}{2}\lvert M_{2+}\rvert^2(1+6x^2-5x^4)$

Table 3.1: Summary of the Multipoles which contribute to the unpolarised cross-section. Information from [21].

3.2.1 Feynman Representation

The Feynman diagrams corresponding to pion photo-production reactions on the nucleon are shown in figure 3.2.1. The pion photo-production amplitude has both the Born or non-resonant terms and resonance contributions. Measurement of the $\pi^+ n$ final state will contain contributions form all of the possible processes illustrated in figure 3.2.1. Diagrams (a) to (c) describe pion production above threshold but below the first resonance region and are predicted by so-called Low Energy Theorems (LETs) for which a general introduction is given in [22]. To summarise here: LETs are expansions of Chiral Perturbation Theory and are useful in the study of threshold behaviour of pion photo-production by their approach; de-composing the reactions into a series of multipoles. However, their predictions begin to fail as the incident photon energies increase above the threshold region. These failings are of interest as they offer insights into phenomena that appear only at threshold, where many terms normally significant in production above threshold with become negligible. Further discussion of the principles of LETs specific to electro- and photo-production is given in [23].

Diagram (d) is specific to charged pion production due to the fact that it relies on the Nuclear exchange current - the Kroll-Rudermann term - rather than a magnetic interaction, and is dominant at threshold. Diagrams (e) contains the Δ resonance contributions to the total cross-section. The process described by diagram (f) also appears when the energy of the incident photon allows the $N \rightarrow \Delta$ excitation but will require a higher incident photon energy than that in diagram (e). This is because of the requirement that a π and ρ/ω be produced at the same vertex, whereas diagram (e) only requires the energy discrepancy between the proton and Δ to be bridged.

It should also be noted that diagrams (c) and (f) also feature the appearance of exchange currents [24]. Exchange currents are the explanation of inter-nucleon forces by particle exchange between them. The two cases illustrated here show a pion and a ρ or ω meson exchange and both show the meson being emitted due to its interaction with the incident experimental probe (a photon in this case) rather than being re-absorbed as would usually be the case.

3.2.2 Resonant Terms

In the region of the $\Delta(1232)$ resonance, the analysis of the two different pion photo-production channels (as described by eqns. (3.1) and (3.2)) allows the investigation of different resonance contributions.

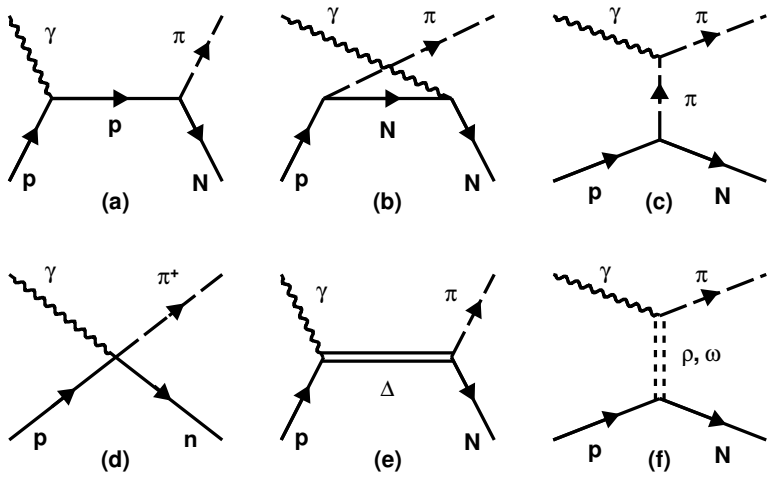

Figure 3.1: Feynman diagrams contributing to pion photo-production on the proton. Diagrams (a) to (c) illustrate Born terms, (d) the Kroll-Rudermann term, (e) the $\Delta(1232)$ resonance contribution and (e) the vector meson exchange term.

The main difference between charged and neutral pion production is the relative coupling strengths to the $\Delta(1232)$ resonance. For charged pion production there is also a contribution from the non-resonant Born terms, whereas π^0 production is more Δ-dominated. Observing the effects of the non-resonant contributions on the asymmetry can be investigated by using a database such as MAID (see Section 1.3.1 for an introduction to MAID) to add or remove resonance contributions. This was done in figure 3.2.2 which illustrates this for each of the two πN final-state channels, showing the effects of removing Born and Δ contributions from the total cross-section. See also Section 9.2.2 of [19] and Section 2 of [25] for further discussions of this.

In terms of the Feynman diagrams for the $\gamma p \rightarrow N\pi$ reaction, the process that includes an excitation of the proton to the $\Delta(1232)$ is given by diagrams (e) as shown in Fig. 3.2.1. The Delta will decay, via the strong force, to produce the final states as given in eqns. (3.1) and (3.2).

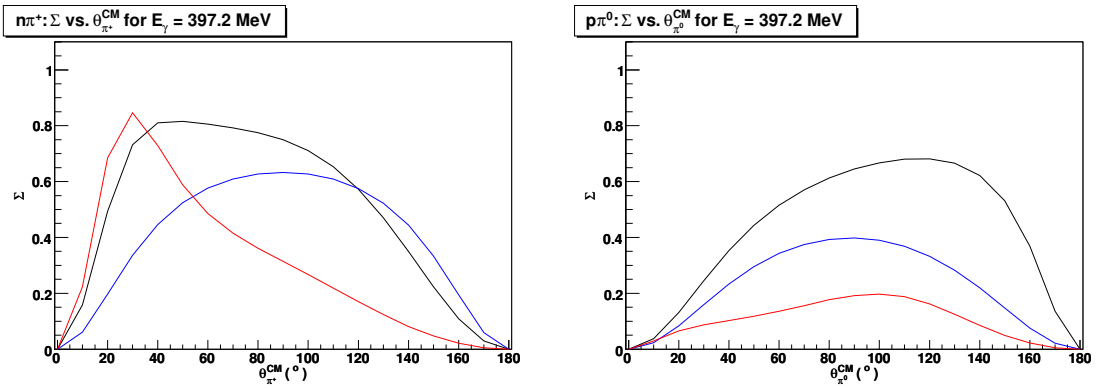

Figure 3.2: The effects on Σ of removing the $\Delta(1232)$ (red) and the Born terms (blue) from the total of all cross-section contributions (black). This is shown for the for the $\pi^+ n$ (l) and $\pi^0 p$ (r) final states. The fits are from MAID [4].

3.3 The Polarised Cross-section

The cross-section for a single pion photo-production experiment, given a beam of linearly polarised incident photons on an unpolarised target, is related to the unpolarised cross-section by:

$$\sigma_{pol} = \sigma_0 \left[1 + A \cos\left(2\phi - \phi_0\right)\right] \tag{3.9}$$

A is the amplitude of the experimentally observed $\cos 2\phi$ distribution, ϕ is the angle between the production plane and the reaction plane (see Fig. 3.3) and ϕ_0 is the initial phase of this distribution. The photon asymmetry Σ is related to A by

$$A = \Sigma P \tag{3.10}$$

with P being the degree of linear polarisation of the incident γ beam.

Fig. 3.3 shows the various angles involved, in the lab. reference frame. θ_{π^+} and ϕ are the polar and azimuthal angles of the emitted pion, taken with respect to the electric field vector of the incident photon and ϕ_0 is the initial phase of the angular distribution. The ϕ distributions of the outgoing particles are used to construct the asymmetry, as a function of θ_{π^+} in the CM frame. Equation 3.9 implies that experimental investigation using a linearly polarised photon beam allows the direct investigation of the cross-section's dependence on emitted pion angle and incident beam energy. The amplitude of the $\cos\left(2\phi\right)$ distribution, when normalised as in section 5.4.4 gives access to the asymmetry, Σ, which

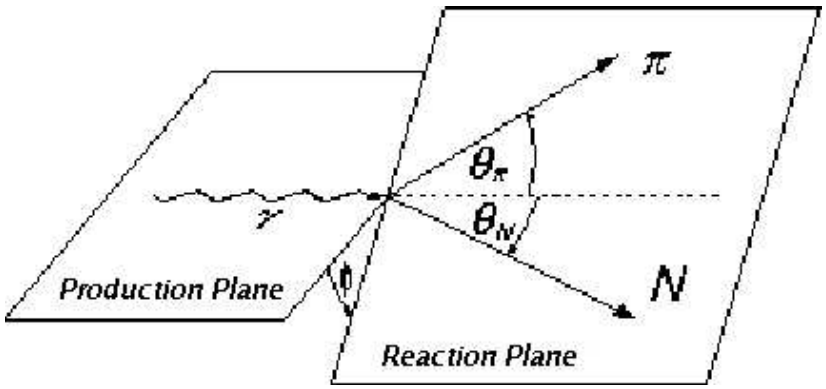

Figure 3.3: Schematic of a typical $\overrightarrow{\gamma}p \rightarrow \pi N$ reaction.

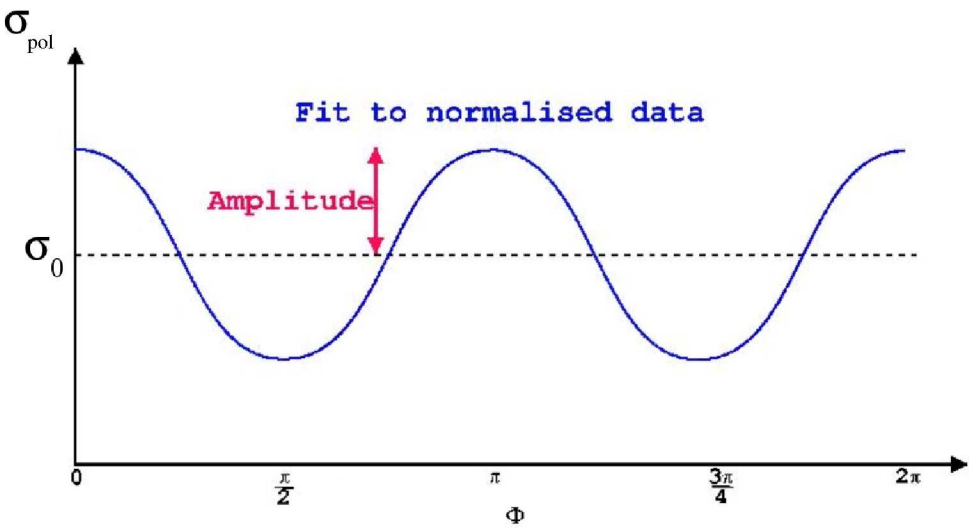

Figure 3.4: Sample graph of a $\cos(2\phi)$ distribution arising from polarised photon production. Σ is extracted from the amplitude of the distribution as described above.

contains the Nuclear Physics information of interest. This process is illustrated schematically in Fig. 3.4.

Chapter 4

Experimental Apparatus

The collection of data was performed during two periods of experimental beam-time: 20 July to 16 August 2004 and 14 September to 4 October 2004. The experimental setup remained unchanged throughout these times, general maintenance excepted, and is described below.

4.1 Experiment Overview

Located 8.5m below ground in the Rhineland-Pfalz region of Germany, the experimental setup consisted of the MAMI-B e^- accelerator and various apparati located within the A2 experimental hall. These are:

- The Glasgow Tagger comprising its magnetic dipole electron spectrometer and Focal Plane Detector (FPD)
- The Crystal Ball (CB) photon spectrometer which houses the target apparatus (lH_2, cryogenically cooled liquid hydrogen), a Particle Identification Detector (PID) as well as two Multi-Wire Proportional Chambers (MWPCs) for allowing the selection of electrically charged reaction products and their subsequent tracking, respectively.
- The TAPS photon spectrometer.

The discussion of the experimental apparatus is presented in the order in which each piece of equipment appears along the beam-line: the Mainzer Mikrotron (MAMI) electron accelerator, the Glasgow photon tagger and polarised Bremsstrahlung production, the lH_2 target and finally the main experimental detectors: the CB - incorporating the PID and the MWPCs, - and TAPS.

4.2 The MAinzer MIkrotron (MAMI) Electron Accelerator

MAMI provides a continuous wave (100% duty factor) e^- beam of between 180 and 883 MeV to any of the three experimental halls that comprise the Instituit Für Kernphyisik at the Johannes Gutenberg Universität in Mainz, Germany. Proposed in the mid 1970s [26], MAMI's realisation came in several stages [27]. The first incarnation of MAMI consisted of a 2.5 MV Van de Graaf generator injector and a single Race-Track Microtron (RTM). Known as MAMI-A1, it came online in November 1979 and could provide an electron beam with an energy of 14MeV. MAMI-A1 was subsequently upgraded to MAMI-A in July 1983 by the addition of a second RTM which increased E_{e^-} to 180MeV. This had the significant benefit of allowing experiments to be performed above the pion threshold for the first time with MAMI. A further upgrade was performed between October 1987 and August 1990 which enabled a beam energy of up to 855 MeV, in 15 MeV increments, to be extracted with the addition of a third RTM. Also during this upgrade, the original 2.5MV Van de Graaf injector was replaced with a 4MeV Linear Accelerator (LINAC) which proved to have much better energy stability [28]. This upgrade was known as MAMI B and it was this accelerator that was used in the work described herein, albeit with a slightly higher beam energy, 883 MeV, due to some improvements in the accelerator's operation since the major upgrade from MAMI-A. At the time of writing, MAMI has recently undergone a further upgrade - to MAMI-C - which will allow electrons to be accelerated to 1.5 GeV. This beam energy will allow studies involving η' and strange meson (Λ, Σ and K) production at MAMI. A plan view of the accelerator complex, including the section added in the MAMI-C upgrade, is shown in Fig. 4.1. All experiments within the A2 collaboration are performed with a beam of real photons. The mono-energetic MAMI-B electron beam is incident on a thin Bremsstrahlung radiator thus creating a continuous spectrum of real photons. The basic principles involved in the Bremsstrahlung process was outlined in section 1.4.2 and further discussion, focusing on Coherent Bremsstrahlung is given in section 4.4.

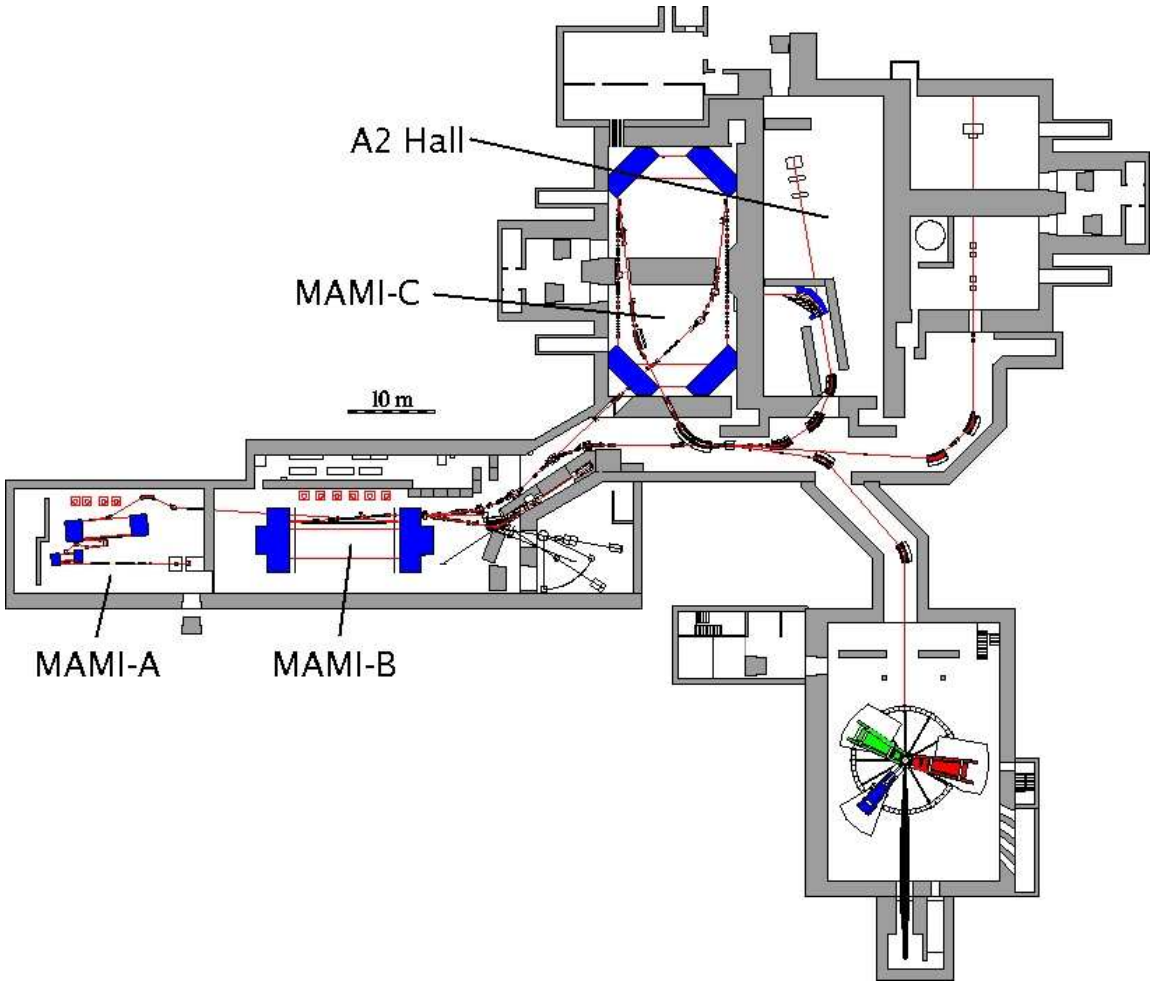

Figure 4.1: MAMI floorplan showing the various acceleration stages of MAMI-A, MAMI-B and MAMI-C . The A2 experimental hall can be seen to the right of the hall housing MAMI-C.

4.3 Photon Tagging and the Glasgow Tagger

The energies of the Bremsstrahlung photons have to be determined in order that they can be correlated with subsequent reaction products to reconstruct the kinematics of individual events. In this case the reaction of interest involves a π^+ and a neutron being detected together, correlated in energy and time. To do this, a technique called 'Photon Tagging' is used. Photon tagging involves momentum analysing the energy-degraded post-Bremsstrahlung electron using its degree of deflection in the magnetic field of the electron spectrometer. The position at which this electron hits the Focal Plane Detector (FPD) by way of a calibration procedure relating this degree of deflection, the incident MAMI beam energy and the magnetic field in the spectrometer - to the energy of the electron. Once this electron energy is known, the energy of the photon that corresponds to it is easily calculable using

$$E_\gamma = E_o - E_{e^-} \tag{4.1}$$

The Glasgow Tagger was used for tagging the photons used in the experiment described herein. The Glasgow Tagger is located within the A2 hall and is comprised of two main elements, the dipole magnet and Focal Plane Detector which are shown in Fig. 4.2. Due to the geometry of the spectrometer magnet and the spatial coverage of the focal plane detector, the energy range covered by the Glasgow Tagger is 40 MeV $< E_\gamma <$ 800 MeV with $\delta E \sim$2 MeV and it is this energy tagged photon beam that continues down the evacuated beam-line towards the experimental target.

4.3.1 The Electron Spectrometer

The e^- spectrometer is essentially a large dipole magnet capable of maintaining a magnetic field strength of around 1T between its two pole faces [29]. The magnetic field strength between the poles of the magnet is monitored at all times using an NMR probe. The field strength is set so as to steer the MAMI electron beam into a lead-shielded beam dump which is fitted with a Faraday Cup to monitor the beam current by way of the charge deposited. Those electrons that interact with the radiator (situated before the dipole magnet) to produce a Bremsstrahlung photon will be bent more severely than the full-energy MAMI beam due to their lower residual energy. These energy-degraded electrons impinge on the Focal Plane Detector which allows the determination of this electron's energy. The

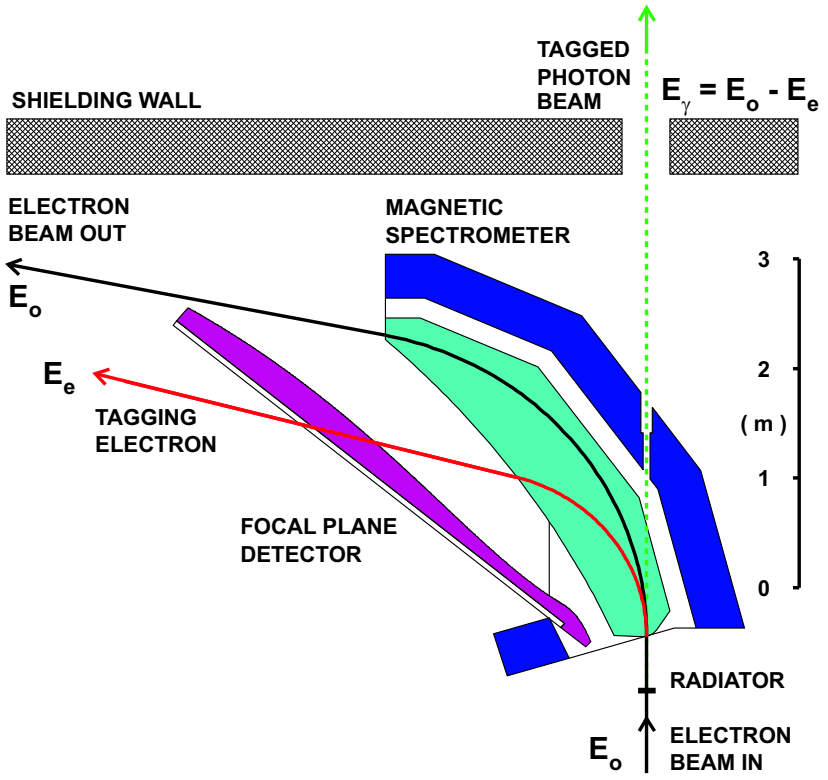

Figure 4.2: The Glasgow Photon Tagging Spectrometer. The MAMI-B electron beam enters at the bottom right of the picture and passes through the radiator where it may interact to produce a Bremsstrahlung photon. If it does, the energy-degraded electron (red line) is bent by the field of the magnetic spectrometer (green) and detected in the Focal Plane Detector (purple) and the photon travels down the beam line (green dashed line) through the shielding wall towards the target material. If no Bremsstrahlung interaction occurs, the MAMI electron beam (black line) is bent into the beam dump with its full incident energy, following the 'Electron Beam Out' trajectory on the diagram.

FPD returns the energy of an incident electron by way of the tagger energy calibration dependent on the magnetic field strength in the electron spectrometer's dipole magnet. The calibration is discussed in the Analysis chapter, in Section 5.2.1.1.

4.3.2 The Focal Plane Detector (FPD)

This consists of a 352 channel plastic scintillator array that deduces the energy of an incident electron by the position upon which it hits the focal plane detector [30]. The individual detectors that comprise the Focal Plane Detector are each 1cm x 5cm x 0.2cm NE111 plastic scintillator detectors, each individually wrapped in 8μm thick aluminised mylar. 353 of these, placed normal to the electron beam trajectories, are used to make 352 detector channels. This is achieved by overlapping each with its neighbours in such a way that an incident electron coming on a trajectory from the spectrometer magnet will pass through two adjacent scintillators. Each FPD channel is a hard-wired OR of two such scintillators and so any instance of only one scintillator being fired will be discarded as not being related to the production of a Bremsstrahlung photon. This type of effect would be due to a background process, most likely a photon or neutron from the beam-line itself or the beam-dump. Figure 4.3 illustrates the setup and orientation of the FPD's plastic scintillators.

The plastic scintillators are optically attached to Hamamatsu R1635 Photo-Multiplier Tubes (PMTs) which are in turn plugged into E1761-04 bases with connections for high voltage supply and signal output. From each PMT the signal goes, via a delay of $\sim$450ns, to the readout electronics: Scaler, Latch and TDC modules. The delay is required due to the fact that any signal from a FPD channel will appear before a trigger from the experimental detectors in 'real time'. The delay allows decisions on whether the event is to be kept or not, having considered the triggers received from the detectors. An OR of the logic signals from all 352 FPD channels is also made for use in trigger coincidence logic. The electronics interface with the VME readout and data acquisition computers by way of FASTBUS data transfer connections (Fig. 4.4). If it is decided to keep the event information, a second trigger from the experimental detectors causes the Scaler, Latch and TDC information to be read out by the VMEbus and then merged with the data from other detector system components. When read-out is complete, a 're-arm' signal is sent, readying the system for the next event. If no second trigger is received, then only the reset signal is sent, thus deleting the non-event.

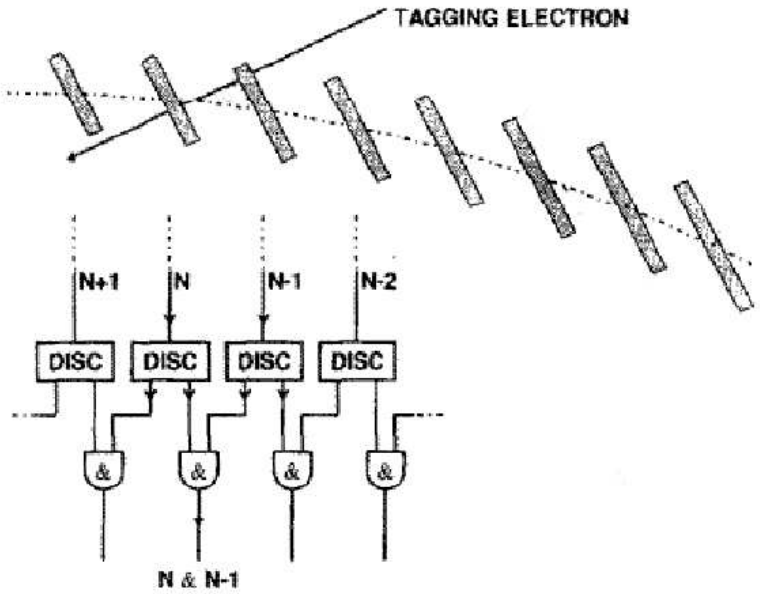

Figure 4.3: A diagram showing the layout of the Focal Plane Detector scintillators and how they create an FPD channel. The dotted line through the scintillators describes a curve parallel to the Focal Plane of the Spectrometer Magnet.

It should be noted that only timing and positional information for the tagger is recorded whereas the actual energy deposited in a Focal Plane Detector element is not. Information regarding an incident electron's energy and thus the Bremsstrahlung photon associated with that particular electron is inferred by the position at which it strikes the focal plane. This position is then associated with an energy via the energy calibration procedure, described in section 5.2.1.1, which requires the magnetic field strength - provided by the NMR probe - and the incident MAMI beam energy.

4.4 Coherent Bremsstrahlung and Linearly Polarised Photons

Scattering from a crystalline radiating material can cause electrons (and thus the resulting tagged photons) to become aligned along planes of the crystal, thus polarising them. In the case of the described experiment, a 10 μm thick diamond crystal radiator was used and the alignment of this diamond with respect to the electron beam was performed. Reference [31] describes the production of Bremsstrahlung from crystals.

The diamond crystal is aligned using the [100] reciprocal lattice vector; the normal to the plane

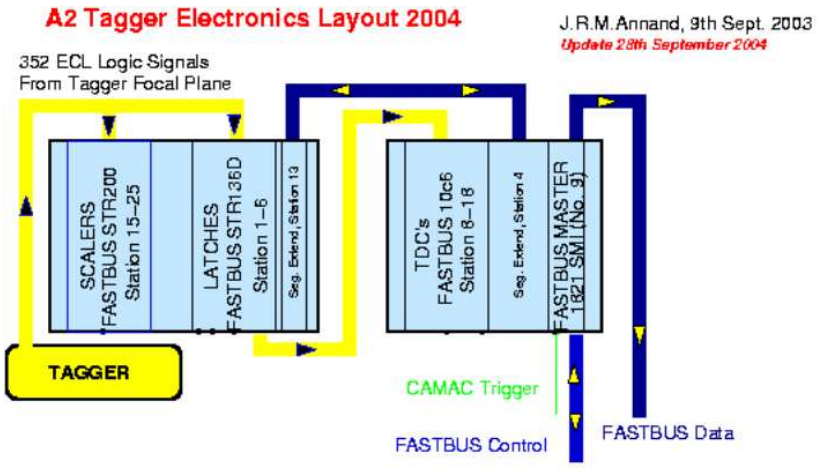

Figure 4.4: A schematic of the Focal Plane Detector electronics.

described by the [022] and [02$\bar{2}$] reciprocal lattice vectors. This plane is chosen as the [022] and [02$\bar{2}$] vectors are orthogonal, and as such are the ones chosen to provide the coherent scattering required for the two linear orientations of the polarised photons. The diamond crystal was rotated between these two planes using a goniometer, a device that can rotate around horizontal, vertical and azimuthal axes and is capable of fine tuning on the μrad. scale. Fig. 4.5 shows a schematic of the goniometer-mounted crystal together with the degrees of movement available to each of the axes of the device. The origin of the system is defined by $\theta_h = \theta_v = 0$ which should correspond to the electron beam direction. In practice, the electron beam is usually displaced by small offset angles θ_{hb} and θ_{vb}. The crystal axis defined by the [100] reciprocal lattice vector will have offsets θ_t and ϕ_t with respect to the origin. By measuring the various offsets it is possible to calculate the goniometer settings (θ_h,θ_v,ϕ) to align the crystal with the beam.

The diamond crystal was aligned using a process known as the 'Stonehenge Technique' [32]. The first stage of the process is to perform an *hv scan*. The crystal axis is swept around in a cone of radius θ_s by incrementally increasing θ_h and θ_v which are given by;

$$\theta_h = \theta_s \sin(\phi) \tag{4.2}$$

$$\theta_v = \theta_s \cos(\phi) \tag{4.3}$$

After each scanning step an E_γ intensity spectrum is measured and as $I = I(E_\gamma, \theta_h, \theta_v)$ a cylindrical plot is produced, an example of which is shown in Figure 4.4. The regions of highest intensity are

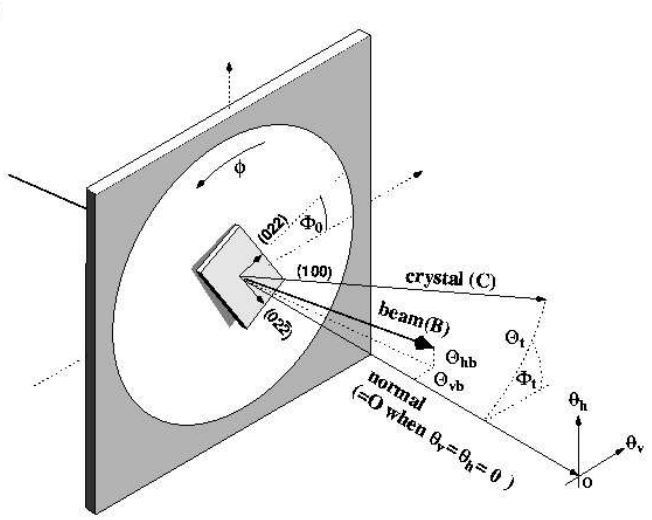

Figure 4.5: A diamond radiator mounted on a typical goniometer. The various vectors, planes and angles are described in the text.

caused by the coherent contributions from the different crystal planes, these described by the [022] and [02$\bar{2}$] reciprocal lattice vectors being the most prominent.

After performing the hv scan, linear fits are made to the points of highest intensity of the [022] and [02$\bar{2}$] reciprocal lattice vectors and the position of the beam axis determined from their intersection (the dashed lines in Fig. 4.4). These offsets between the beam and crystal axes are then applied to the relevant goniometer axes and another scan is performed and its two-fold symmetry checked. When the intensity plot of the scan is symmetrical about both the θ_h and θ_v axes, the goniometer has been correctly aligned. In order to check this, projections of the Stonehenge plot are made onto the θ_v, θ_h plane. Fig. 4.7 shows 'before' and 'after' examples for the alignment procedure.

4.4.1 Determining the Degree of Linear Polarisation.

As mentioned in section 3.3, the amplitude, A, of an asymmetry constructed from the angular distributions of reaction products is dependent on both the photon asymmetry, Σ, a physical property of the reaction, and the degree of linear polarisation of the tagged photon beam, P.

The degree of linear polarisation, P, depends on many parameters, such as the the incident electron energy, the size and divergence of the photon beam. In addition, the atomic numbers of both the

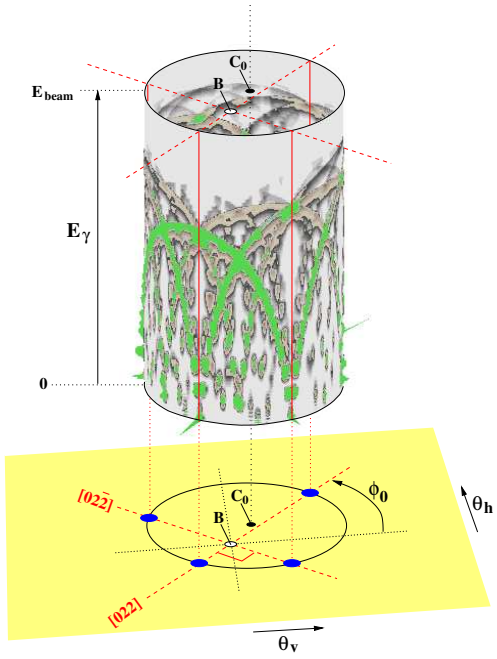

Figure 4.6: Simulation showing a 'Stonehenge' plot produced by scanning on a diamond crystal. B is the direction of the photon beam, C_0 is the direction of the [100] lattice vector in the crystal's default position and ϕ_0 is the default angle of the [022] reciprocal lattice vector with respect to the θ_h axis [33].

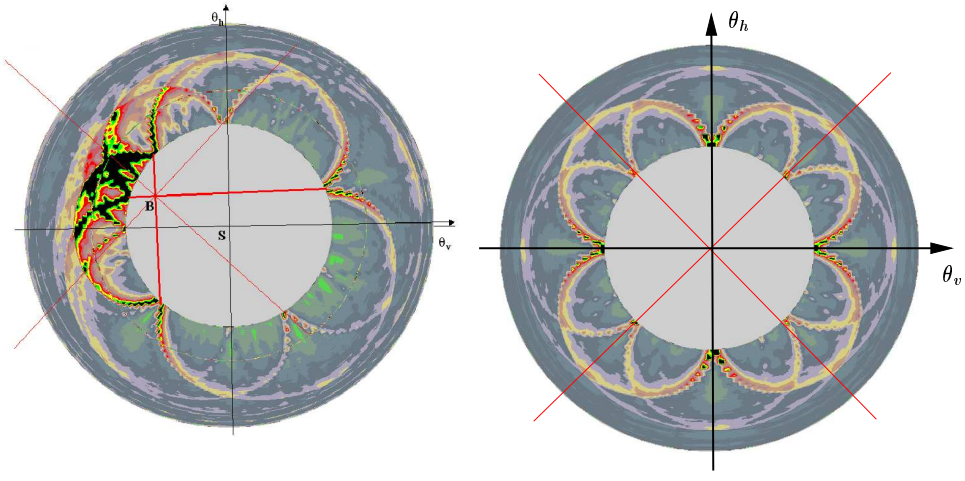

Figure 4.7: 'Stonehenge' plots projected onto the θ_h, θ_h plane for an unaligned (left) and correctly aligned (right) diamond crystal radiator. E_γ increases radially from the centre of the projection.

crystalline radiating material - in this case diamond (Z=6) - and the amorphous reference material - for example Nickel (Z=28) are required. The reference material is required for subtracting the incoherent Bremsstrahlung background from the coherent spectrum produced by e^- scattering from a crystal.

An example of subtracting this background leaving only the coherent spectrum as can seen in plots such as that displayed in Fig. 4.4.1. For a given beam energy, the most accessible way to adjust the degree of linear polarisation is to change the size of the collimator. However, while using a narrower collimator can yield a higher degree of linear polarisation, it will also reduce the tagging efficiency, the measure of how many tagged photons actually make it down the beam-line to be incident upon the target material. Because of the fact that the lower the tagging efficiency the longer it will take to build up event statistics, a suitable compromise has to be reached between these two parameters.

The effects of using a different-sized collimator on the degree of linear polarsation achieved can also be seen in Figure 4.4.1. For the described experiment, the collimators used were 4mm for the 440MeV data and 3mm for the 400MeV data, the change being made as the degree of linear polarisation observed at 440 MeV with a 4mm collimator was deemed to be not high enough. Changing to a 3mm collimator for subsequent running at a polarisation peak energy of 400 MeV did not reduce the tagging efficiency drastically. During experimental running the polarisation orientation was changed automatically approximately every fifteen minutes to ensure that similar amounts of data were gathered for both polarisation orientations.

4.5 The Liquid Hydrogen Target

The target material used during the running of the experiment was liquid Hydrogen, cryogenically cooled using He_4. The apparatus used to house and regulate the target material [36] consisted of a refurbished pumping system and a completely new target cell made from 125μm of Kapton and 8 layers of Aluminium coated Mylar (1 layer = 8μm of Mylar plus 2μm of Al) surrounded by a 1mm thick CFK vacuum tube. This new target cell minimises the density of material between the lH_2 and the experimental detectors. Due to the potentially hazardous nature of hydrogen, the target environment was constantly monitored to ensure that it remained stable in particularly the temperature and pressure. During the running of the experiment the target material was unpolarised. The length

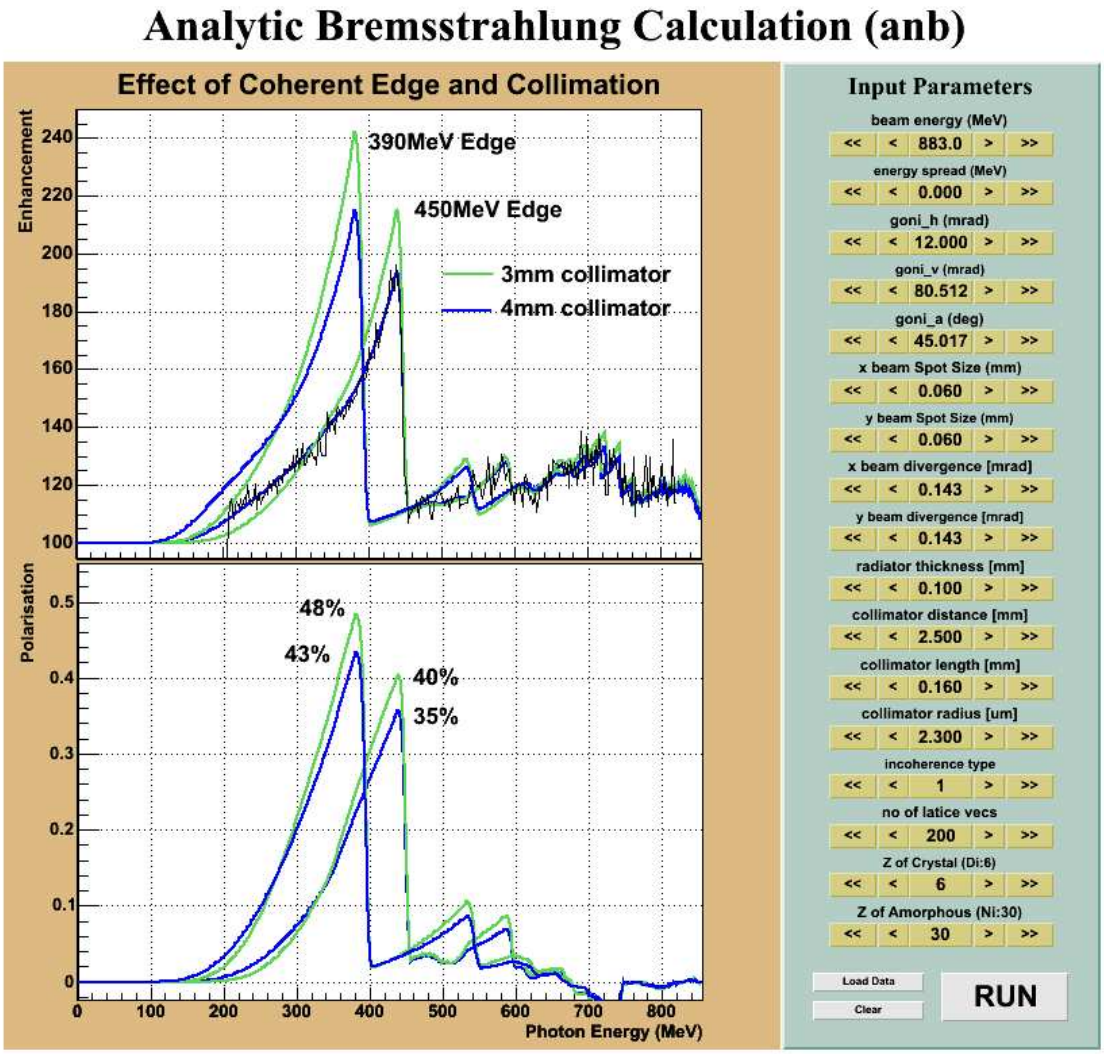

Figure 4.8: Effects of collimation on the degree of linear polarisation achievable. Average values are quoted (bottom) for given photon energies (top).
These effects are discussed further in references [34] and [35]. The ANB calculation is discussed in [33].

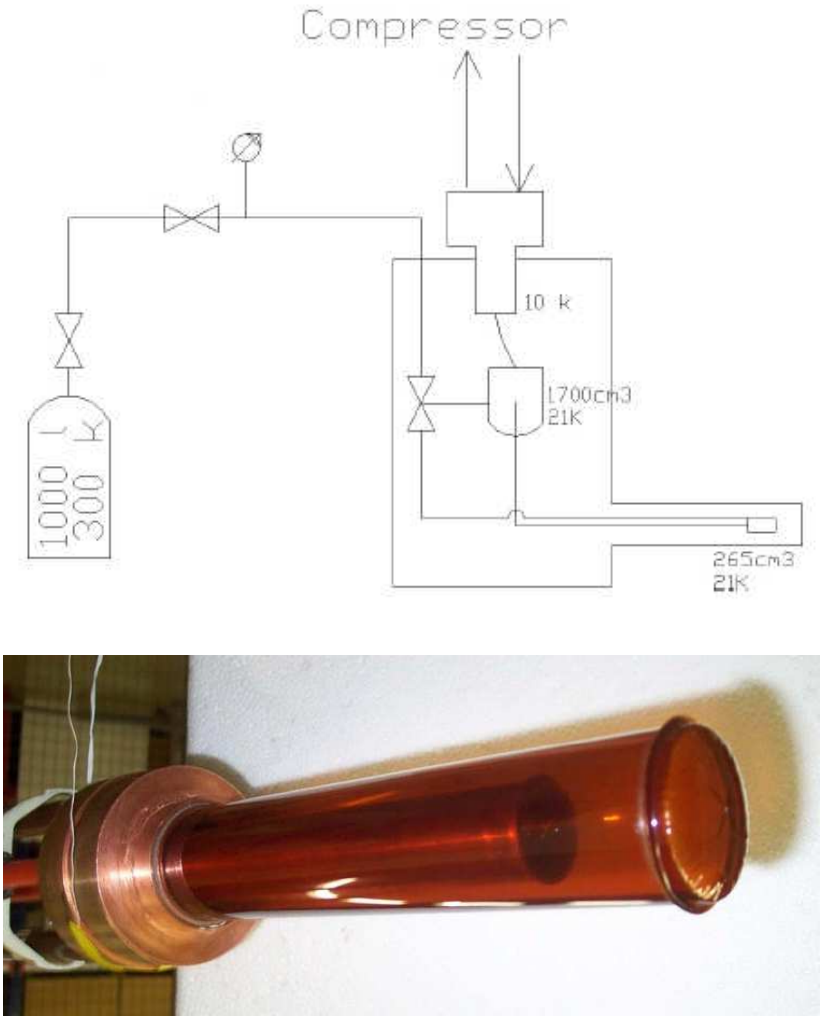

Figure 4.9: Schematic of the plumbing used in the liquid hydrogen circuit (top) and the target cell as used in the experiment (bottom).

of the target cell was measured to be 4.76±0.03 cm long on the beam axis when $T_{lH_2} = 21$K. The pressure was maintained at 1080±10mbar. This yields a target density of 2.02951×10^{23} protons/cm^2 [37].

4.6 Experimental Detectors

A schematic overview of the detector setup used can be seen in Fig. 4.10, while the actual detectors can be seen in Fig. 4.11. They are presented here in the order in which particles will hit them: radially from the centre of the CB, then the forward wall provided by TAPS.

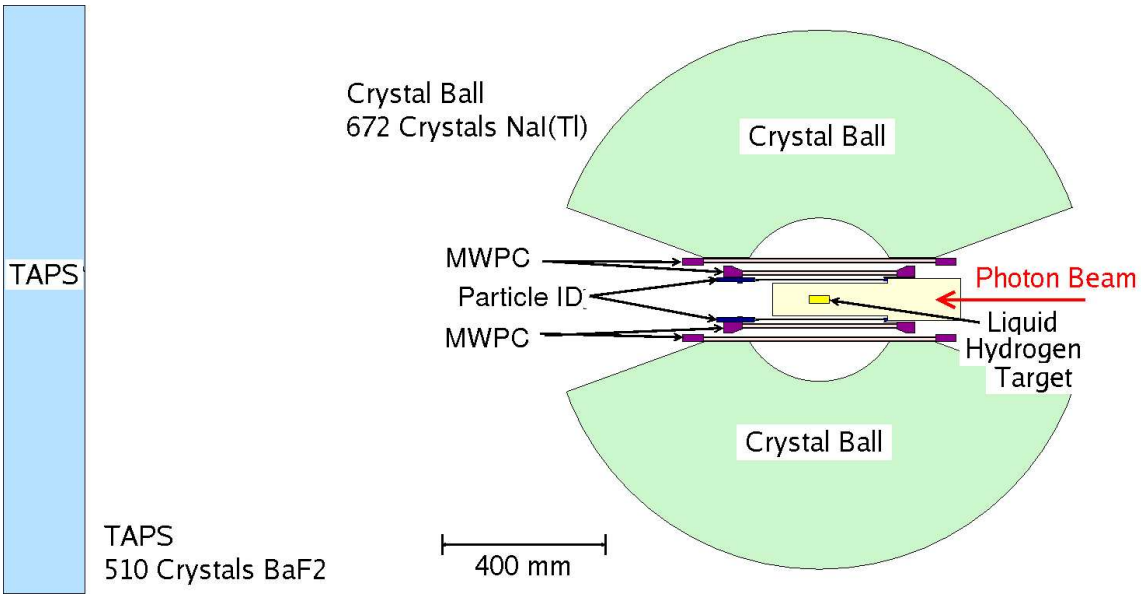

Figure 4.10: Schematic of the target and detectors used in the experiment.

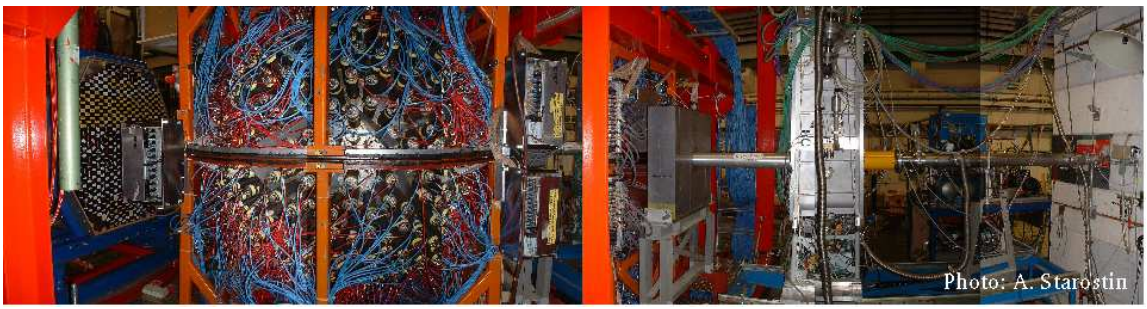

Figure 4.11: Panorama of the tagged-photon beam-line and main experimental detectors, picture by A. Starostin, UCLA.

4.6.1 The Particle Identification Detector (PID)

The detector located closest to the hydrogen target was the Particle Identification Detector (PID). Designed and built by Glasgow in 2003 and installed in the A2 experimental hall in Mainz just prior to experimental running commencing in the summer of 2004, its function is to provide particle identification by differentiating between electrically charged reaction products.

The detector itself is cylindrical in nature, being 10.7cm in external diameter and consists of 24 optically isolated plastic scintillator elements each 31.5 $\times$ 1.2 $\times$ 0.2 cm in size, bevelled along one edge to facilitate the forming of a circular cross-section when assembled. Together with a light guide, photomultiplier tube (PMT) and base, the overall dimensions of the detector were: length 42cm and external diameter 11cm [38]. The material chosen for the PID elements, EJ204, was chosen for its fast timing characteristics; it has a decay time constant of $\sim$2ns [39]. Optical isolation of each element was achieved by the individual wrapping of each scintillator with 2μm Al foil. In Fig. 4.12, the PID can be seen fully assembled and functioning prior to its installation inside the wire chambers and CB. It should be noted that the PID's PMTs are located downstream thus reducing the forward angular acceptance by $\sim 3^{o}$. This was done simply because of space constraints imposed by pre-existing detector system components. Charged particle identification is done by plotting the energy deposited in any particular PID element against that of any hits in a CB crystal located directly behind the PID element in question.

The PID allows different charged particle species to be identified using so-called $\frac{\delta E}{E}$ methods. Depending on the species of particle, different amounts of energy will be deposited in the PID relative to the CB. When correlated with the energy ultimately deposited in the CB elements directly behind the PID, distinct bands can be seen on a plot of PID energy (δE) vs. CB energy (E) - Fig. 4.13. The lower, more horizontal area shows the energy deposited by charged pions and the upper curved band contains protons. Electrons (and positrons) can also be seen, appearing as the dark spot in the lower left-hand corner of the plot.

Scintillations in the individual PID elements are transmitted via light guides (fashioned from a 12.5mm ELJEN UVT acrylic rod [40]) into the same model of Hamamatsu PMTs and bases as used in the photon tagging spectrometer, namely the R1635. The signal from each PID PMT was first fed through a LeCroy 612 NIM '$\times$10' amplifier. From the amplifier the signal was split. One branch fed the signal

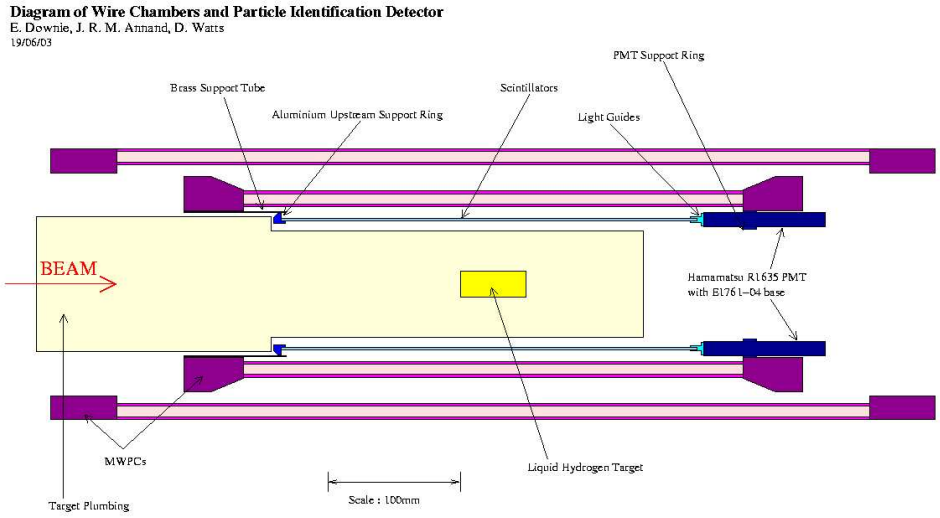

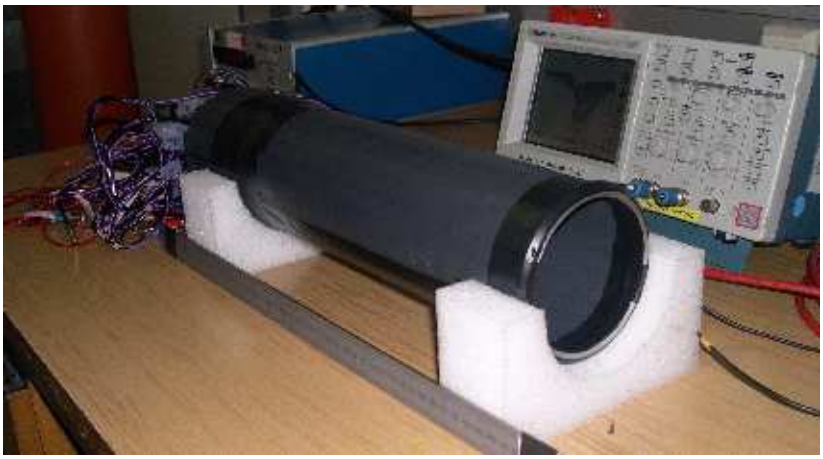

Figure 4.12: Schematic showing the PID as mounted around the target cell inside the CB and wire chambers (top) and the assembled detector just prior to installation (bottom).

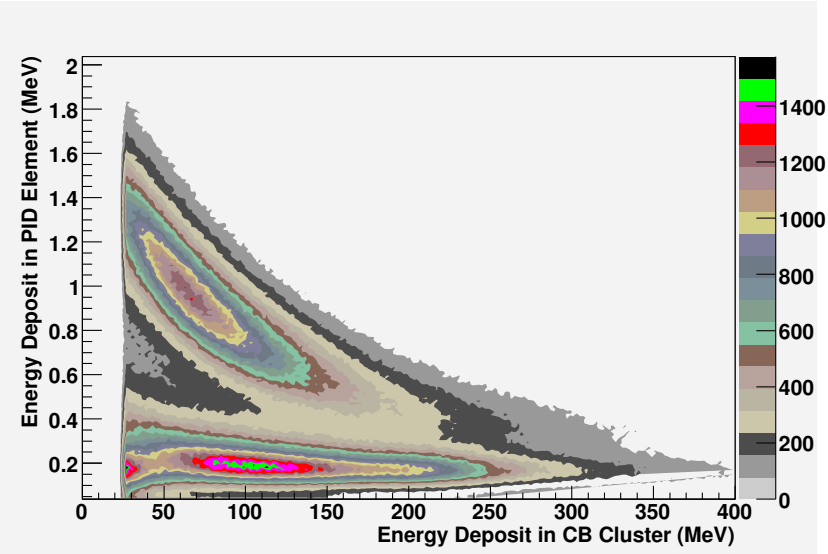

Figure 4.13: Typical 'banana' plot used for particle identification. The regions populated by protons (upper curved band) and charged pions (lower, flatter band) can clearly be seen.

to LeCroy 4413 CAMAC discriminator logic to CATCH TDCs via a LeCroy 4516 CAMAC logic level converter. A logical OR of the discriminator outputs was made to be included as a 'PID Trigger' option in the main experimental triggering system (section 4.8). From the second amplifier output, via 300ns worth of delay cable and an isolating transformer, the signal was fed to a 64-bit Flash ADC to record the PID energy deposits. The delay was required to ensure that the the ADC output time-coincident with the pulse produced by the trigger logic. The ADC was chosen for reasons of speed; the fact that it has only one analogue-to-digital conversion cycle. The PID electronics setup is shown schematically in Figure 4.14, which also shows the integration with the main CB electronics setup.

4.6.2 The Multi-Wire Proportional Chambers (MWPCs)

As the experiment utilised an extended target, some kind of charged particle tracking for event reconstruction is desirable to determine the trajectories of the reaction products. This was done using the two innermost wire chambers from the DAPHNE detector, the large acceptance spectrometer previously used for experiments performed by the A2 collaboration [16].

The MWPCs (Fig. 4.15) each cover 360° in ϕ due to their cylindrical nature and $\theta_{Lab.}$ angles between 21° and 159°. Position resolutions are of the order of 2° in θ and 1.9° in ϕ, while longitudinal, z,

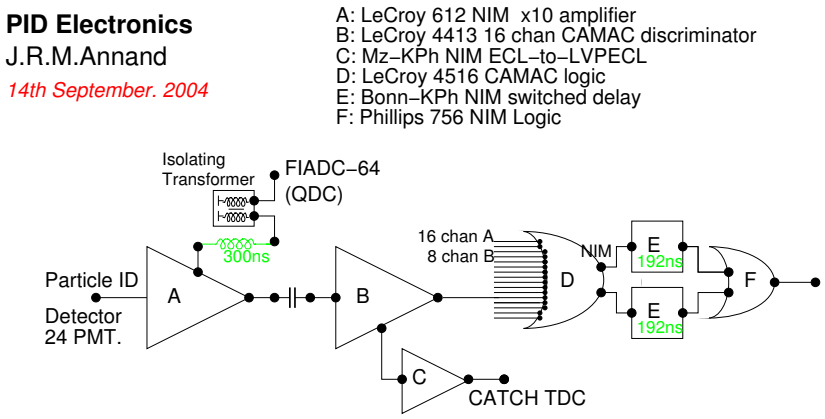

Figure 4.14: The electronics setup for the PID.

resolution depends on the angle of intersection between the particle track and the chamber. As the angle becomes larger with respect to the normal to the beam axis the resolution becomes worse. Track reconstruction efficiencies are around 79.3% [41]. The inner and outer chambers have internal radii 62mm and 92mm respectively and are both constructed from two cylindrical walls of 1mm Rohacell covered in 25μm thick Kapton and are filled with a 149:50:1 mixture of argon, ethane and freon [42].

Each chamber has tungsten anode wires of diameter 2μm located 2mm apart around the circumference and extending along the length of the chamber in question. The inner chamber has 192 wires whereas the outer chamber has 288. Each chamber also two layers of helically wound cathode strips each 4mm wide with 0.5mm between them - one on the inner surface of the cylindrical chamber and one on the outer - at $\pm 45^{o}$ to the anode wires. The inner chamber has 60 and 68 cathode strips on its inner and outer strip layers and the outer chamber has 92 and 100 respectively. The anode-to-cathode spacing for each chamber is 4mm.

The MWPCs are used to pinpoint charged particle locations more accurately than is possible by using just the combination of the PID + CB. The wire chambers reconstruct an event track by using a hit on one of the longitudinal wires to determine the position of a particle in ϕ, and intersections on the helically wound strips to determine its position in θ and z. There ambiguity caused by the fact that each pair of cathode strips crosses the other twice, thus giving two potential θ values, the location of the wire(s) being fired by a particular event is used to remove this uncertainty.

The electronics setup for the MWPCs was comprised of refurbished amplifiers and discriminators and completely new readout components to make it more uniform with respect to the rest of the CB elec-

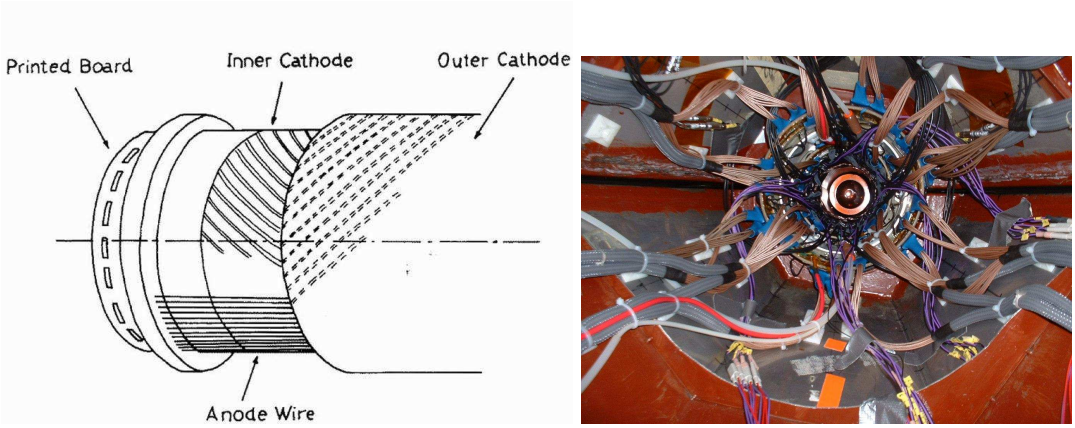

Figure 4.15: A schematic of the Multi-Wire Proportional Chambers showing the strip windings and wires (l) and the MWPCs during installation in the CB, looking upstream (r).

tronics setup. Signals from the cathode strips (longitudinal information) are run through an amplifier to SADCs and the angular information collected by the anode wires goes to an amplifier/discriminator and then to a CATCH TDC. The TDCs were used for removing the angular ambiguity caused by the crossing strips by way of the TDC hit pattern - hit or not. The strips' ADCs allow the hit position to be determined by analysing the sizes of pulses detected. A charged particle track will induce signals on several neighbouring strips and by weighting each strip by the size of signal observed, the mean strip position and thus particle location can be determined.

4.6.3 The Crystal Ball (CB)

The Crystal Ball [43] is a 672 element NaI(Tl) general purpose photon spectrometer, designed at SLAC in the mid 1970s. It was used there, at DESY and then BNL before its transportation to Mainz in the summer of 2002 for use in tagged photon experiments conducted by the A2 collaboration. After being installed in the A2 experimental hall, the electronics were upgraded in order to be able to deal with the higher beam intensity expected in the experiments to be performed during its expected ten year residence in Germany.

The Crystal Ball has spherical geometry, with this sphere being approximated by an icosahedron for reference purposes. The faces are referred to as 'major triangles' which each contain four 'minor triangles' which in turn comprise nine individual detector crystals. This can be seen in figure 4.16.

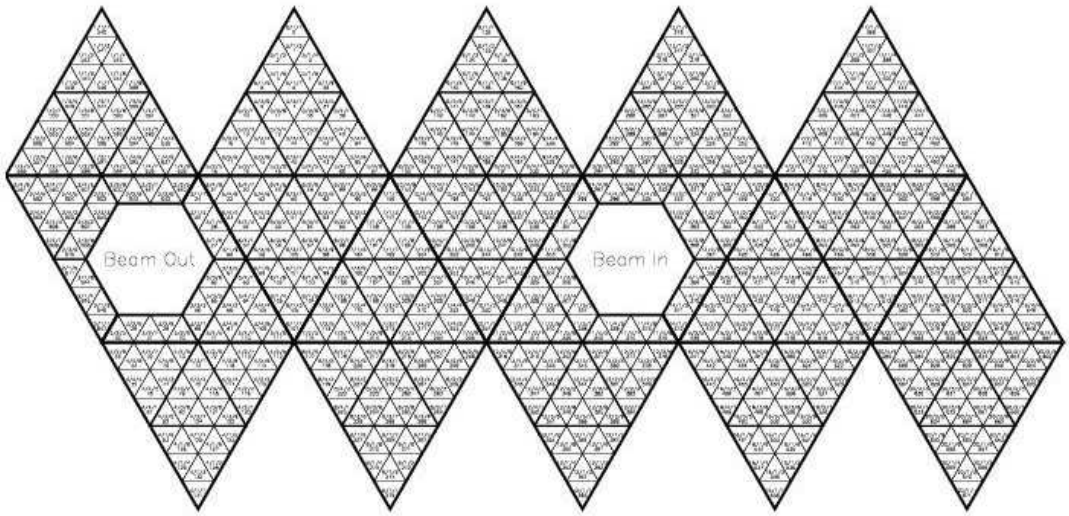

Figure 4.16: Diagram of the Crystal Ball, opened out to show the triangular 'major' and 'minor' subsections as described in the main body of text.

Each crystal is a truncated triangular pyramid 40.6 cm long - equivalent to 15.7 radiation lengths - beginning at a radius of 25.3 cm from the centre of the sphere. Each covers about 0.14% of the full solid angle. Each crystal is optically isolated from its neighbours, being wrapped in reflective paper and Aluminium-coated mylar, viewed by a SRC L50 B01 PMT through a glass window and 5cm air gap. Diagrams of the CB crystals can be seen in figure 4.17. The CB covers $\sim$94.6% of the full 4πsr. solid angle in total. The reduction from full acceptance being due to the entrance/ exit holes and the so-called 'equator region'. The entrance and exit holes exist because the CB was originally designed to be used at colliding beam experimental facilities and account for around 4% of the solid angle acceptance. The equator region is the area where the two halves of the CB are separated and consists of material from the two hemisphere casings (3.6mm of stainless steel $\equiv$ 0.09 radiation lengths) and a 5mm air gap. In total, the equator region accounts for approximately 1.6% of the discrepancy from full solid angle coverage.

As NaI is highly hygroscopic, the environment in which it is contained in must be carefully monitored. Primarily, the two halves of the CB are evacuated to isolate the crystals from the atmosphere. There are however a few small leaks in the CB but these are fairly stable and can be dealt with by regular vacuum pumping. Also, the A2 experimental hall is environmentally controlled to maintain a constant ambient temperature and low humidity levels. Together, these factors help to ensure that the risk of

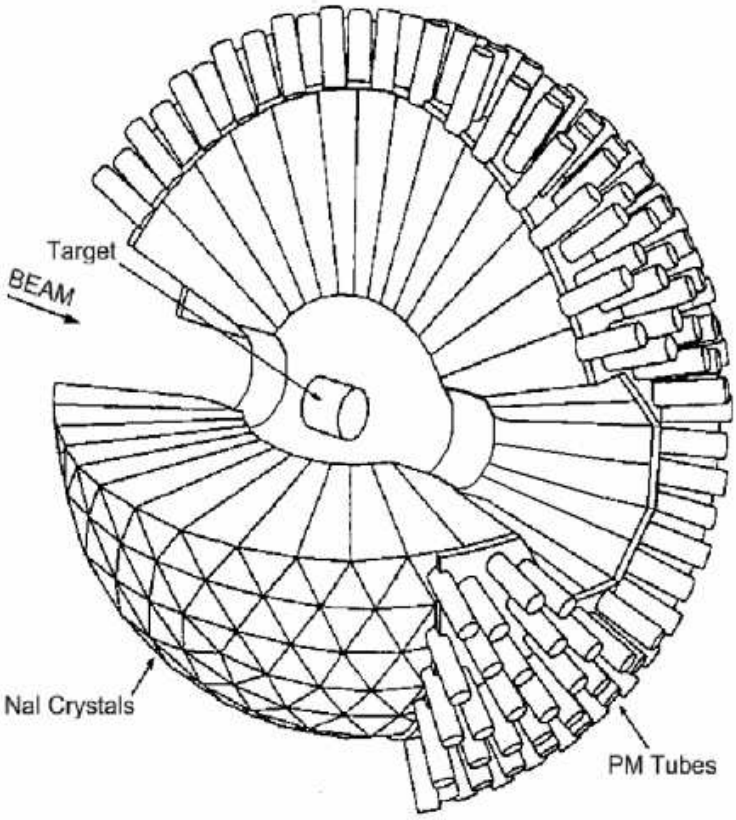

Figure 4.17: Wire-frame schematic of the Crystal Ball showing the triangular nature of the individual crystal elements.

NaI contamination and disintegration is negligible.

It should also be noted that during the detector's lifetime several crystals have become damaged - some more seriously than others - through stress fractures during transportation. The most obvious effect of this damage manifests itself as reduced light collection in the associated channels in the data but this is only significant at very low energies.

The basic requirement for the CB electronics - given that an upgrade was necessary to allow the A2 photon flux to be handled successfully - was that it should be flexible; giving the freedom to select different trigger conditions and to be able to scale these in order to pick out reactions of interest. It was also required that the new system was to be fully integrable with the Data Acquisition (DAQ) system [44]. CB data transfer was provided by was of VMEbus-based LynxOS systems and ACQU software - a well established, tried and tested system in Mainz [45]. The final design [46] consisted of splitting the signal from each NaI crystal's PMT and sending the respective branches to a Sampling ADC (SADC) and an Uppsala-designed dual threshold discriminator. The SADCs have an extremely useful feature: dynamic pedestal subtraction. This enables the pure signal - minus background noise - to be extracted directly from the ADC. From the discriminator the outputs were sent to:

1. A CATCH TDC (from the low threshold - equivalent to an energy of 1MeV).
2. A 16 channel logical OR unit with a high threshold of 10 MeV. The OR was used with LeCroy 4413 16 channel CAMAC distributors to form the CB and TAPS 'Multiplicity 2' and 'Multiplicity 3' Level Two trigger inputs (see Section 4.8 for descriptions of these.

This setup is shown schematically in figure 4.18.

Power for the CB PMTs is supplied by four High Voltage power supply units: two for the 'polar' regions of the ball (the top and bottom), each having 180 NaI crystals and PMTs, and two for the 'equatorials' (the areas either side of the latitudinal centre ball) each comprising 156 crystals/PMTs. Each power supply unit provides a potential difference of -1500V and each PMT draws a current of approximately 0.5mA. As common HV supplies are used for the CB, gain alignment of the individual PMTs is performed by varying the potential on a specific dynode via a potentiometer. If however, the gain for each detector in any one of the bunches needs to be changed by the same amount - an

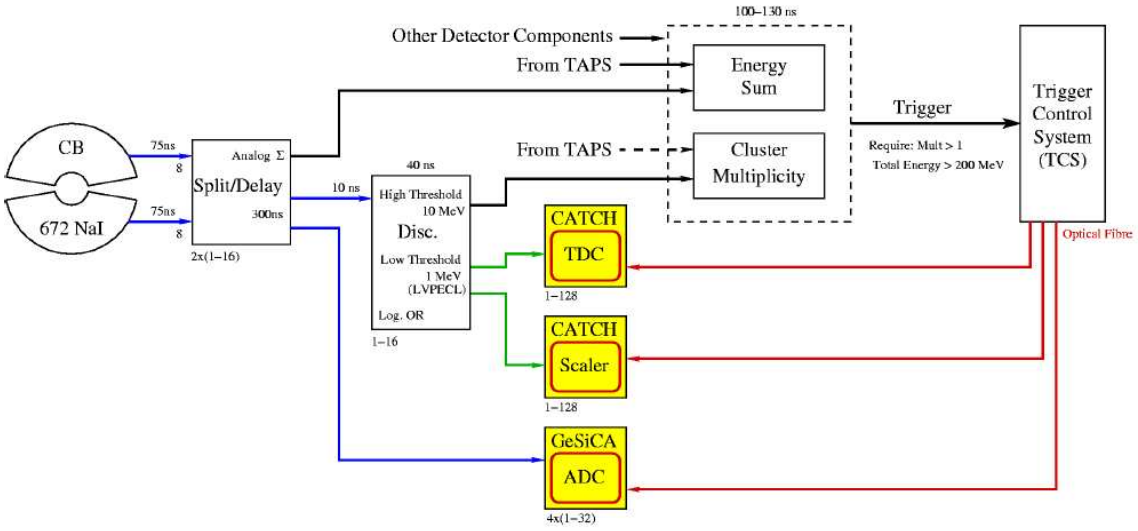

Figure 4.18: Schematic diagram of the Crystal Ball electronics as they were for the running of the experiment.

admittedly unlikely scenario - then this can be done by simply changing the supply voltage to that particular bunch.

4.6.4 TAPS

TAPS, the detector formerly known as the 'Two-Armed Photon Spectrometer' is a BaF_2 based detector designed and built in the late 1980s as a photon and meson spectrometer [47]. For this experiment, TAPS was employed as a forward detector to plug the hole in the forward angular acceptance of the CB. Its modular structure and thus relative portability mean that TAPS can be very easily moved from one laboratory to another and thus the moniker 'Travelling Around Photon Spectrometer' might seem to be more fitting to the TAPS acronym. This is especially true as its capacity as a forward wall in the CB@MAMI experiments is in parallel with more traditional operations at other accelerator facilities.

The TAPS setup used consisted of 510 BaF_2 crystals, each with a Hamamatsu R2058-01 PMT attached to the rear end-face of the crystal. TAPS was built into a flat-faced wall (Fig. 4.19) 1.734m downstream from the liquid hydrogen target cell. Each TAPS crystal is hexagonal in cross section, having an inner radius of 59mm and a length of 250mm ($\sim$12 radiation lengths). In front of each crystal is a hexagonal

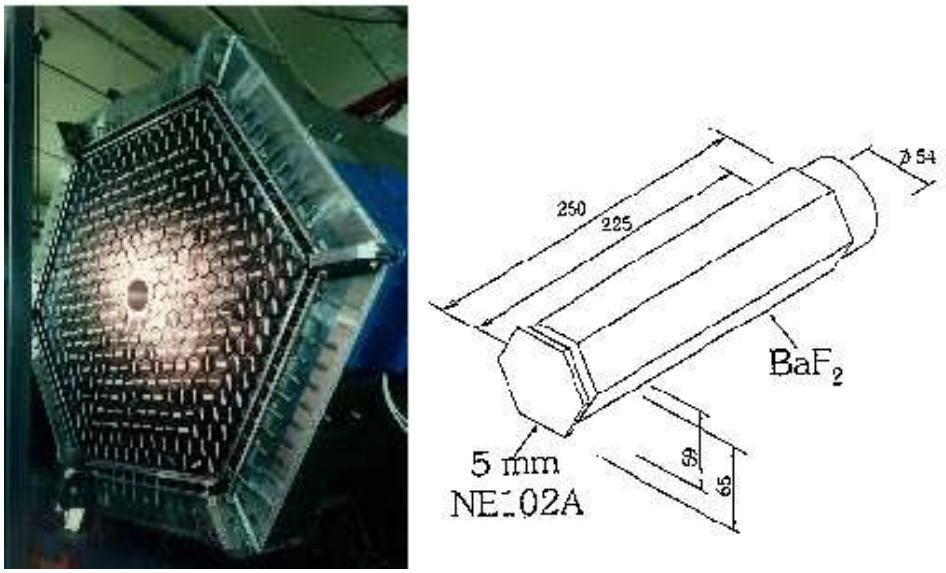

Figure 4.19: The TAPS forward wall (l) and a single BaF_2 element (r). The PMT attaches directly to the rear of the crystal.

charged particle veto detector made from plastic scintillator (5mm thick NE102A) and read out by a separate Hamamatsu H6858 PMT via wavelength-shifting optical fibres - found to be much more efficient than standard optical fibre - of diameter 1mm.

Particle identification for TAPS is more complicated than for the CB. $\delta E/E$ methods are impossible due to the fact that there is no ADC connected to the plastic veto detectors due to the fact that pulse-height resolution in BaF_2 is too poor to use this method successfully. Because of this, particle species discrimination is achieved primarily from pulse-shape analysis (PSA), although time-of-flight methods can also be used. This is discussed fully in section 5.2.5.1.

The TAPS electronics setup consisted of a integrated custom-built suite built in a VME framework [48] which consists of a constant-fraction (CFD) and two leading edge discriminators (LEDs), a TDC and four QDCs for each BaF_2 crystal. A schematic of this is shown below, in Fig. 4.20. The read-out is based on the necessity of having separate information on each of the two scintillation components associated with the detector material, the so-called 'fast' and 'slow' components. These are illustrated in Figure 4.21 along with the schematics of the two signal integration times used for TAPS PID; the 'short' and 'long' gates. The scintillation signals typically occur within a few nanoseconds in the case of the fast component (the large spike near the origin) and within 600 ns (the large 'tail') in the case of the slow component. The amplitudes of the scintillation components are proportional to the ionisation

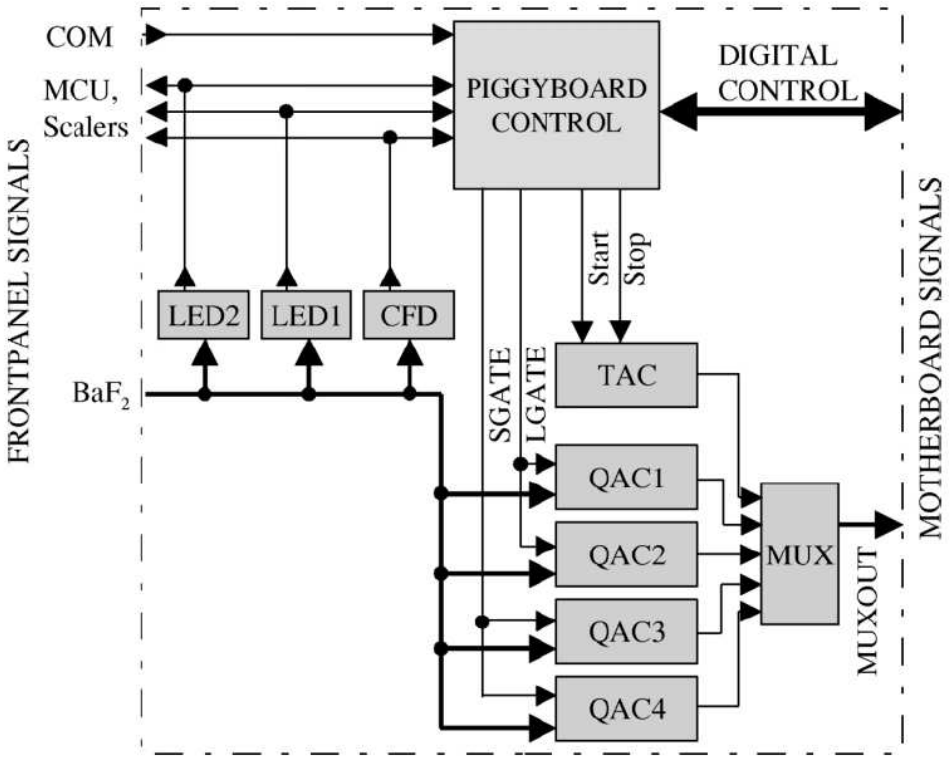

Figure 4.20: Schematic of the TAPS readout electronics.

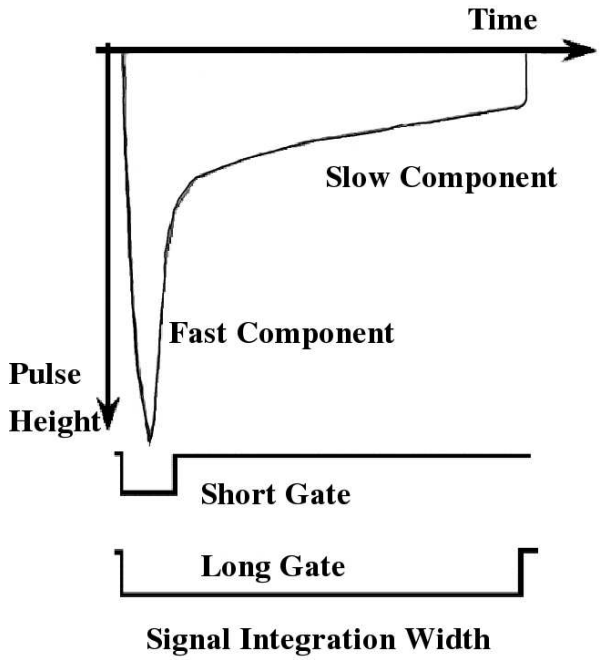

Figure 4.21: Graph of a typical BaF_2 signal.

in the BaF_2 and relate to the velocity of the incident particle. By comparing the charge accumulated during the duration of the two gate widths, short (~20ns) and long (~2μs) particle ID can be achieved. Particle identification for TAPS is further discussed in Section 5.2.5.1. The useful feature of the CFDs and the reason for their inclusion in the TAPS electronics setup is that they remove the need for having to correct for systematic timing offsets known as 'walk' during the data analysis phase as is the case for the CB (walk corrections for the CB are discussed in Section 5.2.4.3). They do this by adding a delayed, inverted component of a pulse height vs time signal to the original signal creating a bipolar pulse whose zero-crossing point is independent of pulse amplitude and as such, should be very similar for each detector element.

4.7 Data Acquisition

The collection of the experimental data was performed using AcquRoot [49] analysis software. AcquRoot has been developed by J.R.M. Annand et al. and builds on an original 'Acqu' software package conceived in 1989. Acqu originated as a DAQ system and was followed by an analysis package based on

CERNLIB [50]. The current version of Acqu has been re-named AcquRoot as Acqu has now evolved to have all the features of the previous software with the added bonus having been integrated with the CERN based 'ROOT' High Energy Physics analysis software package [51]. The latest version of AcquRoot comprises three elements: AcquRoot for general analysis, AqcuMC for Monte-Carlo simulation of detector response and AcquDAQ, an as-yet unused ROOT-integrated DAQ system.

When using AcquRoot for DAQ purposes, the data acquisition procedure is:

1. Event selection by electronic trigger conditions.
2. Read-out of digitised detector signals collected.
3. Data streams from the different detector apparati are collected and written to disk.
4. 'Online' analysis performed to ensure that the detector systems are operating as expected.

During the execution of the DAQ procedures, 'online monitoring' is performed to ensure that the experimental detectors are operating as expected. This monitoring consists of running a speed-configured AcquRoot analysis session in conjunction with ROOT macros to look at various diagnostic detector output spectra as the data accumulates. The bulk of the data analysis - see Chapter 5 - is done 'offline' at the analyst's own institution at their own leisure, reading in data files stored locally on hard disk, having been transported from Mainz on magnetic data tapes.

A complete readout of the CB comes from assimilating all signals from the following: Tagger FASTBUS TDCs and scalers (352 channels), the PID FIADC-64 and CATCH TDCs (24 channels each), SDACs for the MWPC strips and CATCH TDCs for the wires (320 and 480 channels respectively), and the CB's SDACs, CATCH TDCs and scalers (672 channels each). This produces data at an approximate rate of 2GB every 40 minutes.

4.7.1 TAPS DAQ

As the TAPS Data Acquisition can be run independently of the CB it is fitting to discuss it separately here. A schematic overview of the TAPS DAQ setup is shown in Fig. 4.22. Based on VME (for BaF_2 signal processing) and CAMAC systems (the charged particle veto detectors), the TAPS DAQ has its

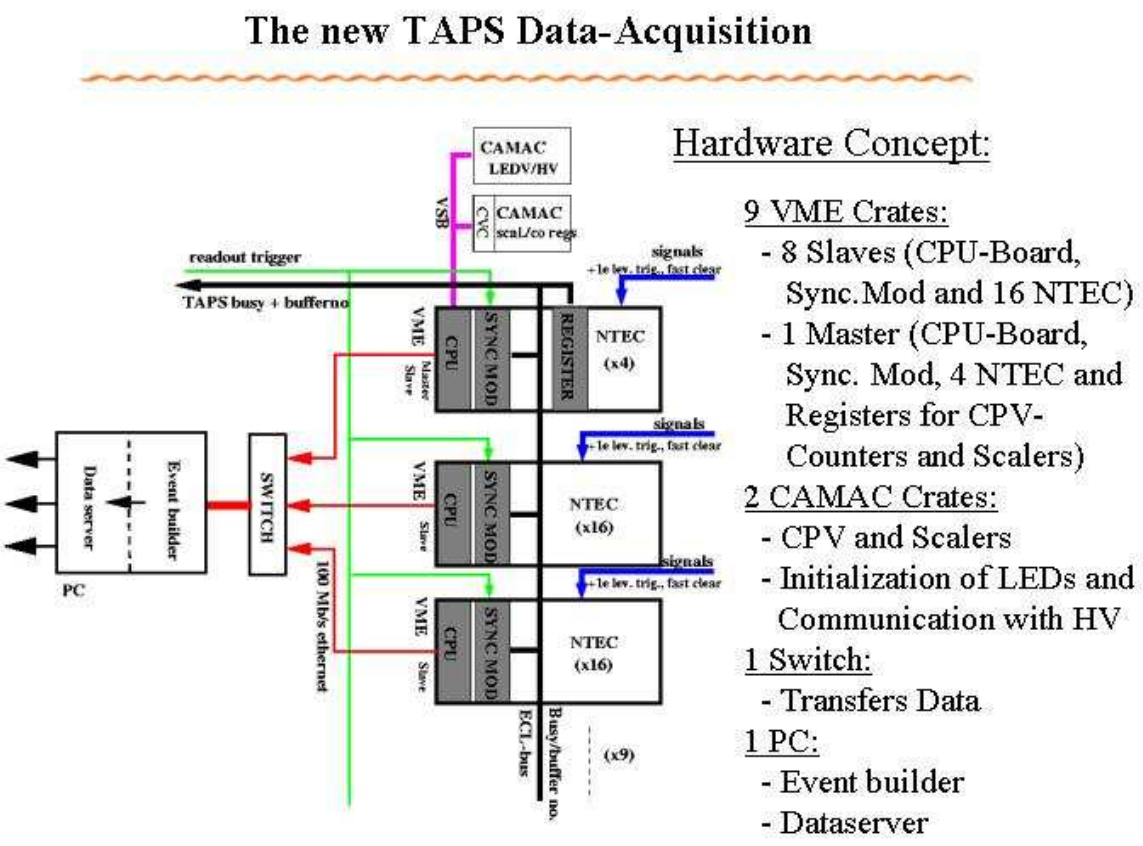

Figure 4.22: Schematic overview of the new TAPS DAQ system.
Its operation is described in reference [52].

own data server and event builders enabling it to run as a stand alone unit, as it has to when used at other experimental facilities. The forward wall itself is divided into eight sections - labelled A to H - for inclusion in the trigger logic. Integration into the CB DAQ is provided by further combining the eight TAPS sections as shown in Fig. 4.23 into four 'sectors'. An OR is then made of these, then used as an input to the Level One trigger - see the bottom left hand portion of Fig. 4.26.

4.7.2 Synchronisation

A major challenge for this experiment was to make the two DAQ systems - CB and TAPS - easily integrable with each other. This was done by taking the output of each of the four sectors then delaying them by 61ns in order to ensure timing coincidence between TAPS and the CB, and then

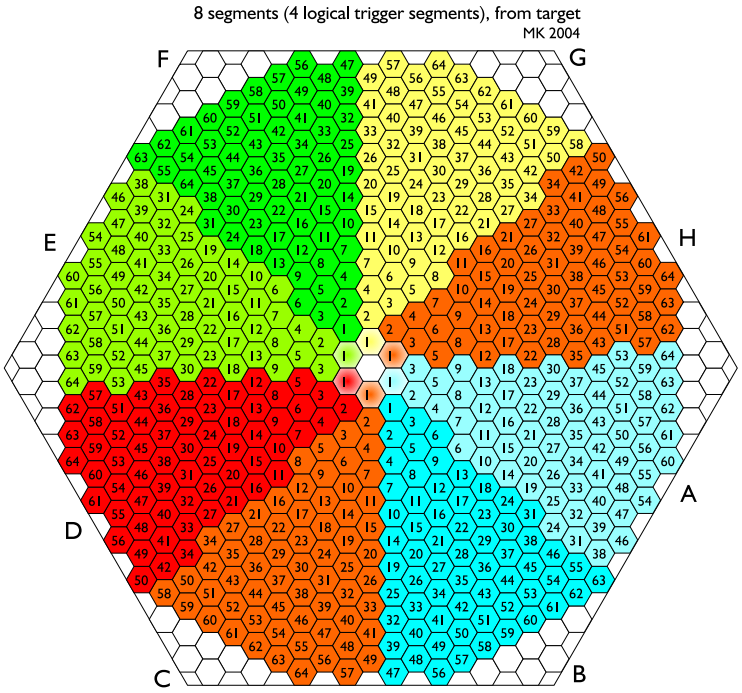

Figure 4.23: The eight sections of TAPS as recognised by the CB DAQ.

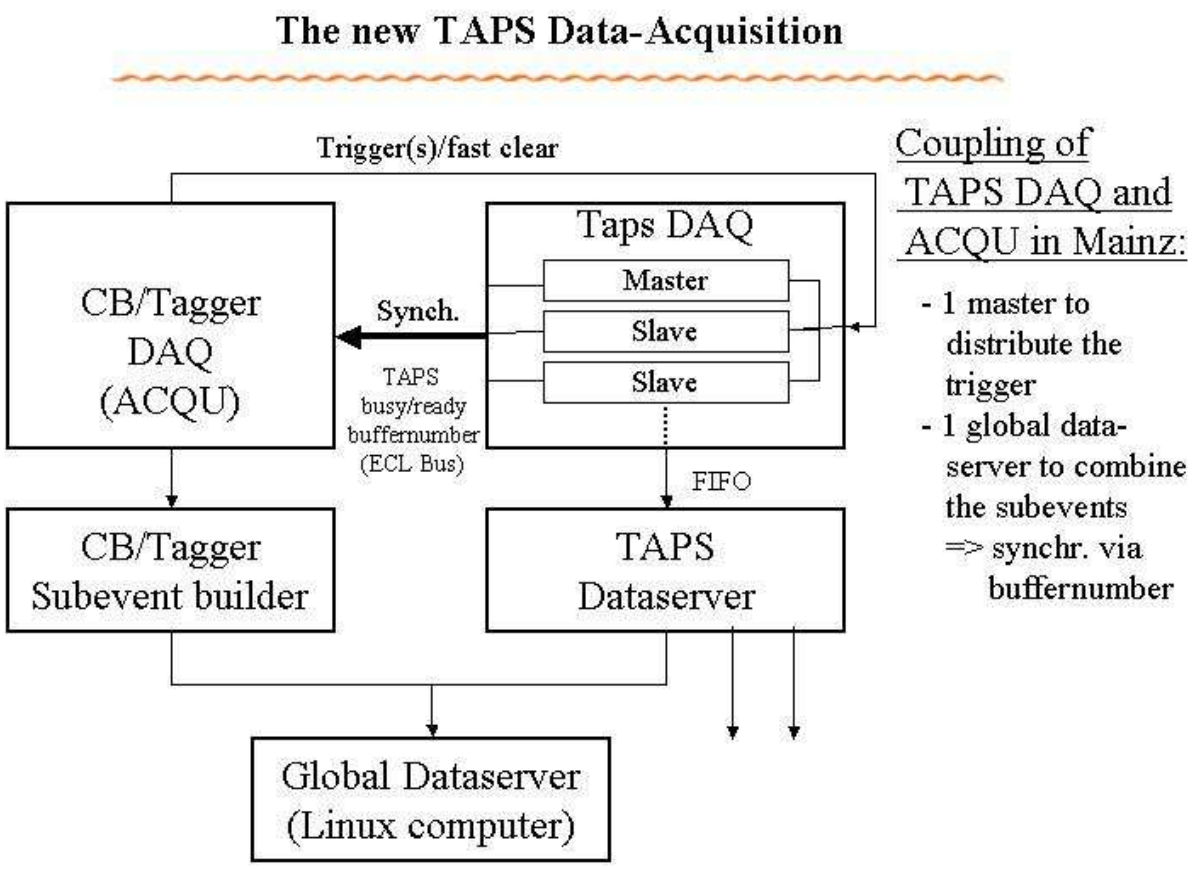

Figure 4.24: Schematic diagram illustrating the integration of the CB and TAPS DAQ systems. This is fully described in [52].

including these in the cluster multiplicity section of the CB DAQ. This is illustrated in figure 4.7.2. Synchronisation between the CB and TAPS was achieved by checking the event indexes were consistent in both detectors and also by ensuring timing coincidence between the two. If the timing coincidence strays from the cross-referencing window shown in Fig. 4.25 then the data file is closed and the DAQ reset.

4.8 Triggering

Several triggering options are provided to make the detectors as flexible as possible during both testing and production running. There are two levels of trigger; 'Level One' (L1) and 'Level Two' (L2). Generally triggers are left pretty 'open'; energy thresholds are set low and multi-cluster events are

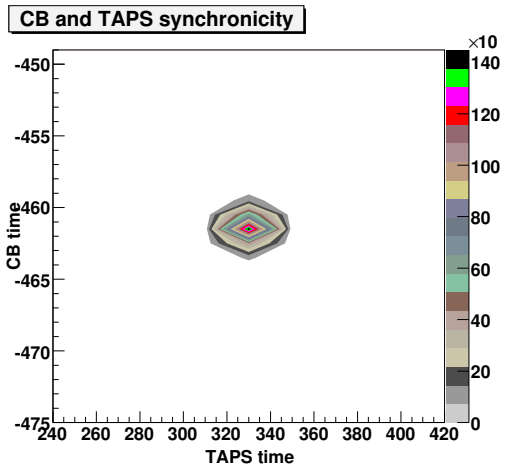

Figure 4.25: Plot showing typical synchronicity of the CB and TAPS.

permitted to allow several reaction channels to be studied at once. This tends to lead to a large quantity of data being accumulated and requires careful separation in the analysis software to produce the 'signal' required for the final state of interest. The full trigger logic can be seen in figure 4.27.

4.8.1 The Level One trigger

The main input to the L1 trigger is from the CB Energy Sum, the total energy deposit in the CB which can be set at an experiment-dependent level. As the conducted experiment ran in parallel with others which required the detection of the Energy Sum trigger was set to approximately 40 MeV. The Level One trigger also features inputs from TAPS and the PID. The latter is used for providing an input dependent on there being at least one charged particle - of any type - present in the CB, whereas the TAPS input is an AND of the four sectors from their own DAQ system, discussed in section 4.7.1, above.

4.8.2 Level Two triggers

If the L1 trigger is satisfied during experimental running the L2 triggers are initialised. These triggers are constructed corresponding to different clustering multiplicities that may be required for different experiments and are dependent on the number of final state particles. These multiplicities usually two (M2) or three (M3) and are selected by adjusting the discriminator thresholds (~30 and 50 MeV

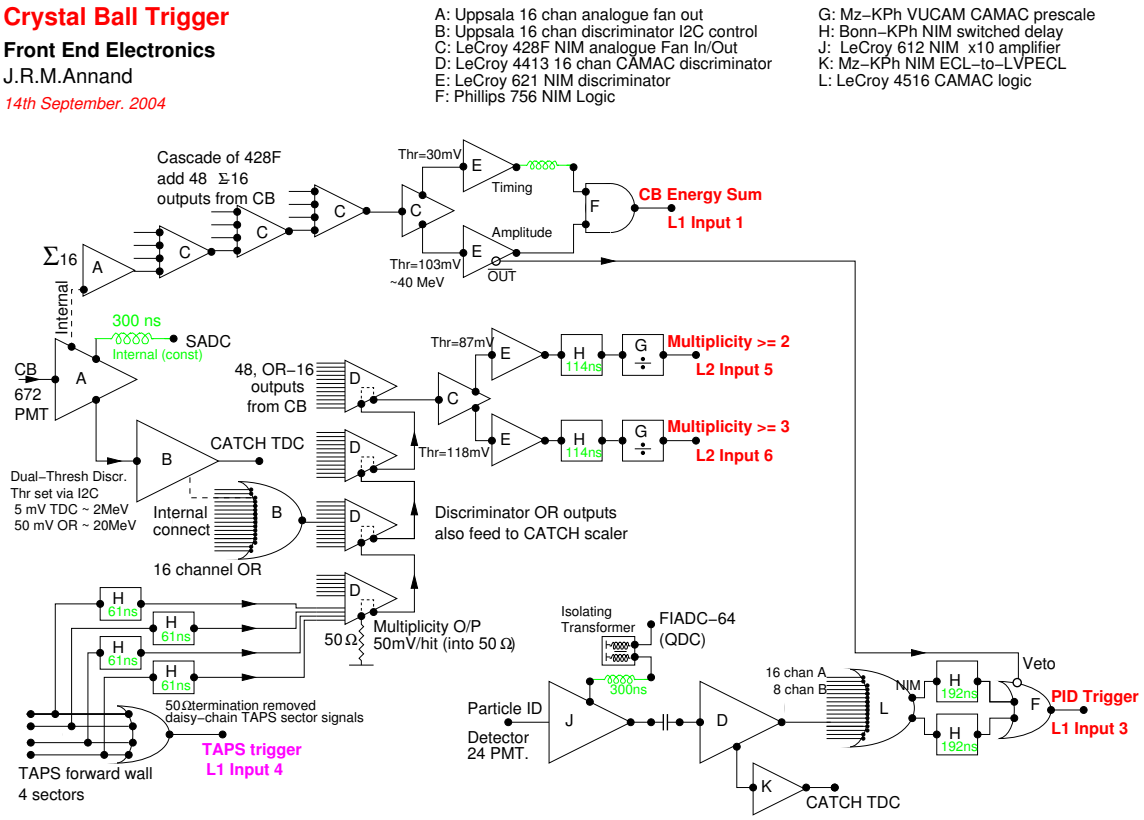

Figure 4.26: CB electronics used for trigger generation incorporating TAPS and PID trigger contributions.

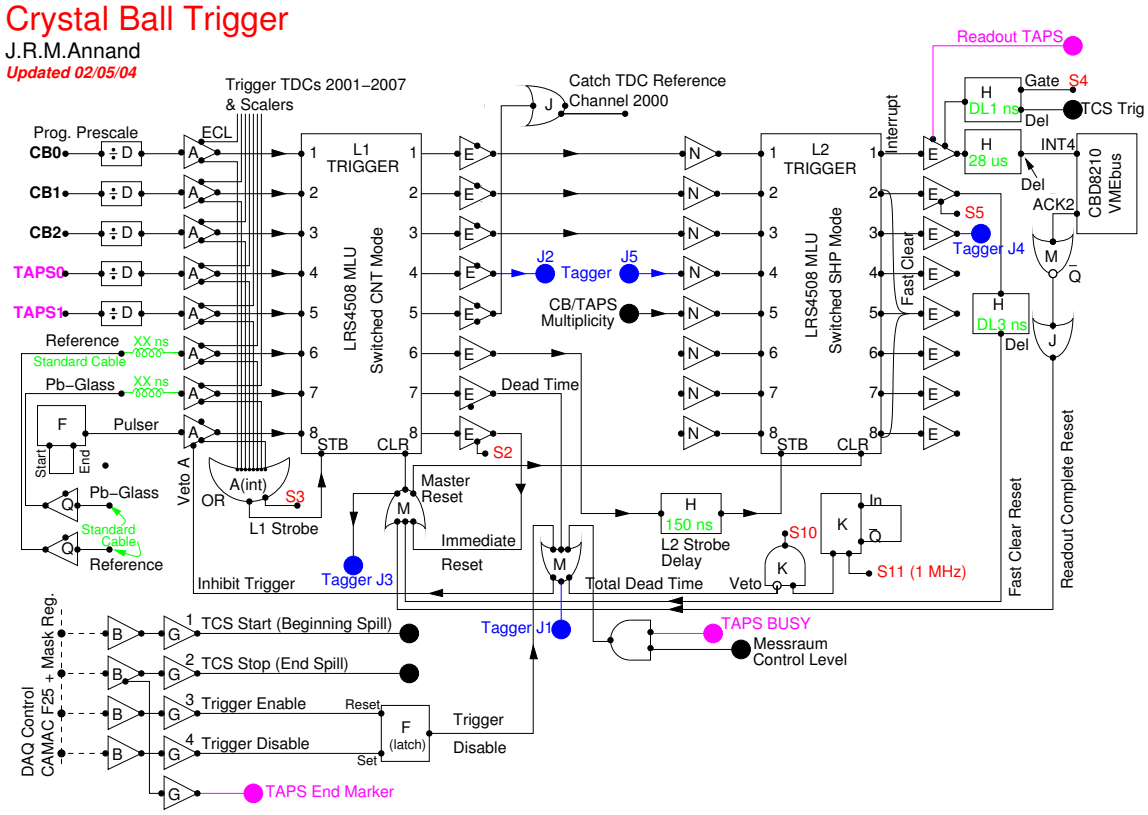

Figure 4.27: The trigger logic setup. This circuit allows different trigger conditions to be set, for example cluster multiplicities and energy thresholds. It also allows different detector system components to be included in or excluded from the trigger as desired.

respectively for the M2 and M3 L2 triggers). The trigger condition used to obtain the $\pi^+ n$ final state used for the experimental analysis presented here was M2 which required two energetic clusters (groups of detector crystals exhibiting energy deposits) to be seen in the CB and/or TAPS. These energy deposits would relate to two particles being produced as a result of the $\overrightarrow{\gamma} p$ interaction. As the experiment was being run in parallel with those designed to measure the radiative cross-section of $\overrightarrow{\gamma} p \rightarrow \pi N \gamma'$, the M2 trigger was pre-scaled by a factor of 1/10 to prevent two-cluster events swamping the DAQ systems which would prevent these M3 events from being read out.

Chapter 5

Analysis

The analysis of the experiment consisted of several basic stages: calibration; particle ID and reaction reconstruction; event characterisation in terms of angular distribution and polarisation; asymmetry construction and extraction. An overview of the analysis software used is presented first, then the experiment-specific analysis procedure discussed in greater detail.

5.1 The AcquRoot Analysis Package

The Physics analysis described herein was performed using AcquRoot [49], the ROOT-based analysis software package also used for the CB DAQ (Section 4.6.3). AcquRoot's design makes it very flexible, thus allowing individual users to customise and adapt it for their own specific analysis needs. This framework incorporates all of the display features, tools and facilities provided by 'ROOT', the CERN-developed, C++ based, object-oriented data analysis framework [51].

5.1.1 Analysis Structure

AcquRoot, also written in C++ follows the hierarchical structure of the ROOT classes, including the 'TClass' naming convention with the corollary - for the most part - that the prefix becomes 'TA2'

implying its use within the A2 collaboration. The AcquRoot hierarchy divides an analysis setup into three main layers: Physics, Apparatus, Detector. The 'Detector' classes are concerned with the individual detector components, for example the individual plastic scintillators that comprise the PID. The 'Apparatus' classes - for example the CB - include the detectors that comprise them; the PID, MWPCs and NaI in the case of the CB. The 'Physics' level deals with reconstructing the variables required for the analysis in question. As can be seen in Figure 5.1.1, examples of each type of class would be: TA2Physics (Physics), TA2CrystalBall (apparatus), and TA2PlasticPID (detector). Each class in the analysis setup has an associated configuration file, generally identifiable by the '.dat' filename suffix. In these files, input parameters are entered; for example, the TA2Tagger class has both the MAMI beam energy and the Tagger's magnetic spectrometer NMR reading entered as input parameters in the Tagger.dat setup file. This is useful for quantities that change during data taking over an extended period of time, for example having multiple instances of a detector calibration files, one each for any particular set of experimental running conditions. This enables changes to be made to the analysis setup quickly, without having to recompile AcquRoot.

5.2 Calibrations

After data collection was completed, calibrations were performed for each detector component in order to convert the digital signals collected by the various ADCs and TDCs into energy and time information. These calibrations were generally undertaken by collaboration members at the institutes to which a particular detector is closely affiliated. For example, the Tagger and PID calibrations were performed in Glasgow by the author; CB calibrations were done by UCLA and Mainz students, and TAPS by Basel and Giessen students. Those calibrations that were the responsibility of the author will be discussed in greater detail than those performed by others, for which a general overview is given.

5.2.1 Tagger Calibrations

The Glasgow Tagger has to be calibrated in both energy and time to be successfully used in an AcquRoot analysis. The electron energy calibration was performed by C. McGeorge [53] and Section 5.2.1.1. This information was then incorporated into AcquRoot using a set of ROOT macros written

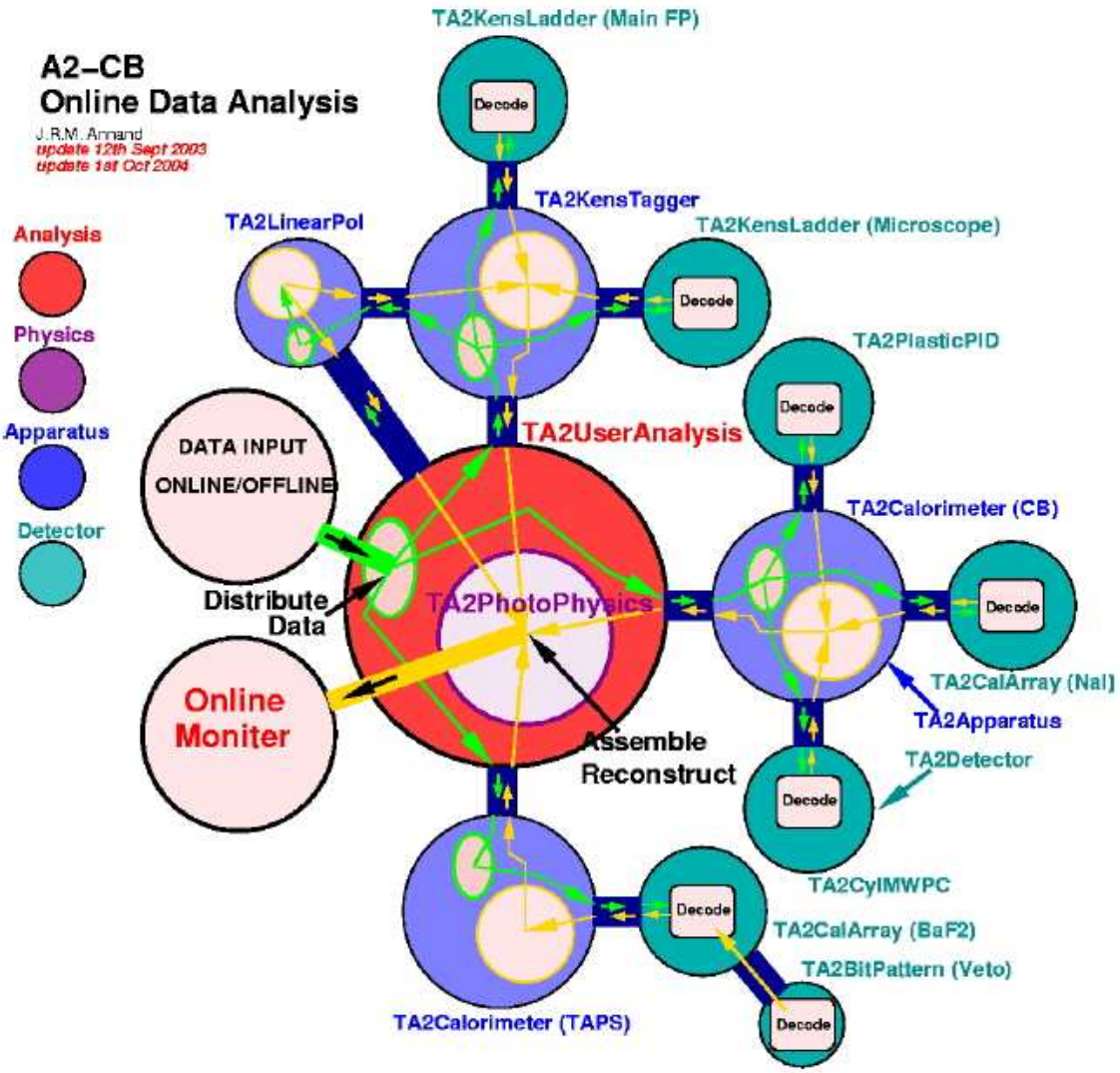

Figure 5.1: A schematic overview of the AcquRoot analyser.
The hierarchical structure described in Section 5.1.1 can be seen, as can the flow of data; raw data being fed in (green) and results being returned (yellow).

by K. Livingston (see directly below, and reference [54]) which were used to produce calibration files for each experimental beam-time, the actual process being performed and monitored by the author. In AcquRoot the Tagger setup comes in two parts: the files 'Tagger.dat' and 'Ladder.dat', the former being the Tagger Apparatus class setup file where the average NMR value and MAMI beam energy are entered. Ladder.dat is the Detector setup file called by Tagger.dat, and contains the values for each parameter related to each individual FPD element. Tagger calibrations were performed using Tagging Efficiency runs for each experimental beam-time and were repeated whenever run conditions changed.

5.2.1.1 Energy

The Tagger energy calibration consists of calculating the electron energy that corresponds to the centre of each FPD channel. The tagger energy calibration comes not from the analysis of deposited energy in the focal plane scintillators - the focal plane detector has no ADCs for this purpose - but from the hit position on the focal-plane detector in conjunction with the known MAMI electron-beam energy and the magnetic field of the spectrometer, measured by an NMR probe. The calibration is performed for several MAMI beam energies ($180 < E_{e^-} < 840$ MeV) by the program "tagcal" [55] which taggcal interpolates the energy corresponding to a given FPD hit position, from fits made to specific calibration runs where an electron beam of known energy is bent directly into the FPD rather than the beam dump as is usual for the full-energy MAMI beam.

This procedure requires some user inputs; the strength of the magnetic field in the spectrometer and MAMI beam energy. The magnetic field strength is taken from the NMR probe multiplied by a factor derived from measured field maps at 1.0 and 1.4 Tesla. The energy calibration procedure is more fully discussed in reference [56] which focuses on the 'Tagger Microscope', a detector used for providing a much better energy resolution (between a factor of two and six) over a small, movable region ($\sim$60 MeV) of the main photon tagger's energy range.

In AcquRoot, the procedure for acquiring the correlation of Tagger channel with incident photon energy has two components. First, a time alignment is performed to make extraction of prompt and random coincidence events more straightforward. Secondly, an energy calibration to relate hit tagger channel to electron energy is produced. At each stage, a previously created file is read in and the information it contains added to. For example, when running the energy calibration, an already time-aligned

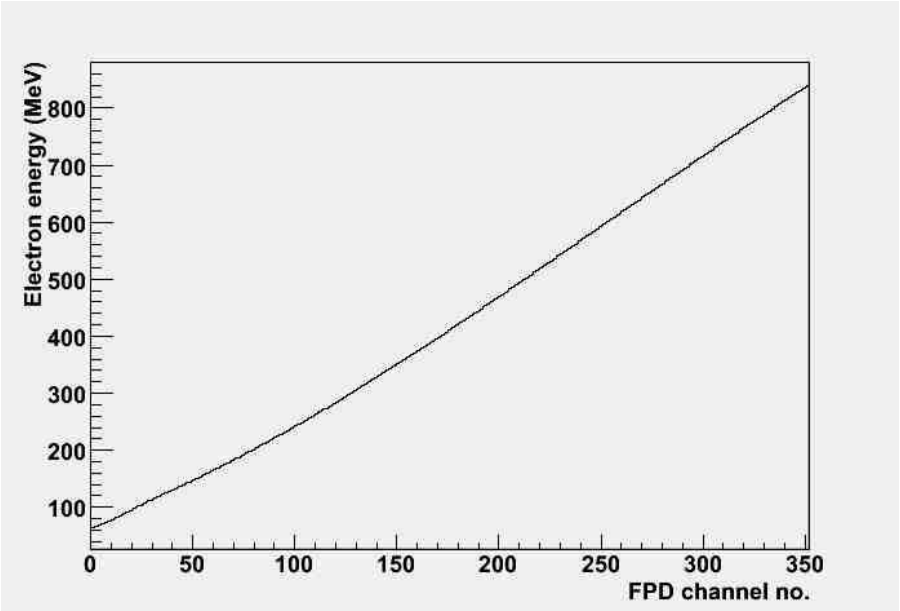

Figure 5.2: An example Tagger 'Energy Map'. This relates the energy of an electron striking the Tagger's Focal Plane Detector to the FPD channel number.

file - as created by following the procedures outlined in section 5.2.1.2 - is read in, then the energy calibration macro is run with the NMR value and E_{e^-} being entered as input parameters. This yields a final Tagger calibration file containing both energy and timing information. In addition, the energy calibration creates a Tagger 'Energy Map' which relates the incident electron energy to Tagger channel number which in turn relates, by position, to the energy of the associated Bremsstrahlung photon. A typical example of an Energy Map can be seen in Fig. 5.2. The relationship between electron energy and FDP channel number is non-linear because the widths of the scintillators changes to accommodate approximately the variation in dispersion along the length of the focal plane. This dispersion arises as the FPD scintillators are aligned to sit perpendicular to the paths of the electrons leaving the field of the Tagger's magnet.

5.2.1.2 Timing

The timing alignments for the tagger involve converting the signal from the TDC of a firing FPD element into a time (measured in ns) using the known channel-width-to-time conversion factor (117ps) and then applying an offset so that the peak of the coincidence distribution comes at the same time for each tagger channel. First, a null calibration file is created, with all timing values set to zero.

Then a tagging efficiency file is analysed offline using AcquRoot and a ROOT macro run which fits a Gaussian distribution to the peaks of the time spectra for each FPD channel. The mean of each of these Gaussian distributions is noted, and its offset from the aligned time is calculated. For the purposes of the experiment discussed here, the peaks were aligned to sit at a value of 50ns. It is the offset from this 50ns that is written to a new ladder setup file as the timing calibration factor. Plots of this process can be seen below, in Fig. 5.3.

5.2.2 Tagging Efficiency

The other Tagger-related quantity one has to know when performing real photon experiments is the so-called 'tagging efficiency' [57]. This quantity is necessary to relate the measured number of electrons incident on the FP detector to the number of photons incident on the experiment target. When calculating photon asymmetries the effects of tagging efficiency cancel by the nature of taking ratios of the polarised cross-sections, and so the tagging efficiency does not have to be explicitly calculated for this type of analysis. Tagging efficiency is defined as

$$\varepsilon_{tagg} = \frac{N_\gamma}{N_{e^-}} \tag{5.1}$$

and is not unity as the bremsstrahlung is collimated before the target. The value of ε_{tagg} depends on collimator diameter, electron beam energy, focal-plane hit position and radiator thickness, typically being of the order 0.3-0.5 for the present experiment.. The tagging efficiency is measured, typically once per day during experimental running, by inserting a Pb-Glass Cherenkov detector, which has a detection efficiency of 100% for energetic photons, directly in a very low intensity photon beam. The tagging efficiency is given by

$$\varepsilon_{tagg}[i] = \frac{N_\gamma[i]}{N_{e^-}[i]} \tag{5.2}$$

N_γ is the number of counts in the coincidence peak of the ladder-channel TDC and N_γ is the number of counts in the scaler attached to the FPD channel. i is the FPD detector channel in question.

Eqn. (5.2) however, does not allow for background counting rate in the FPD scalers. This was estimated by measuring the FPD counting rates with beam turned off, before and after the tagging-

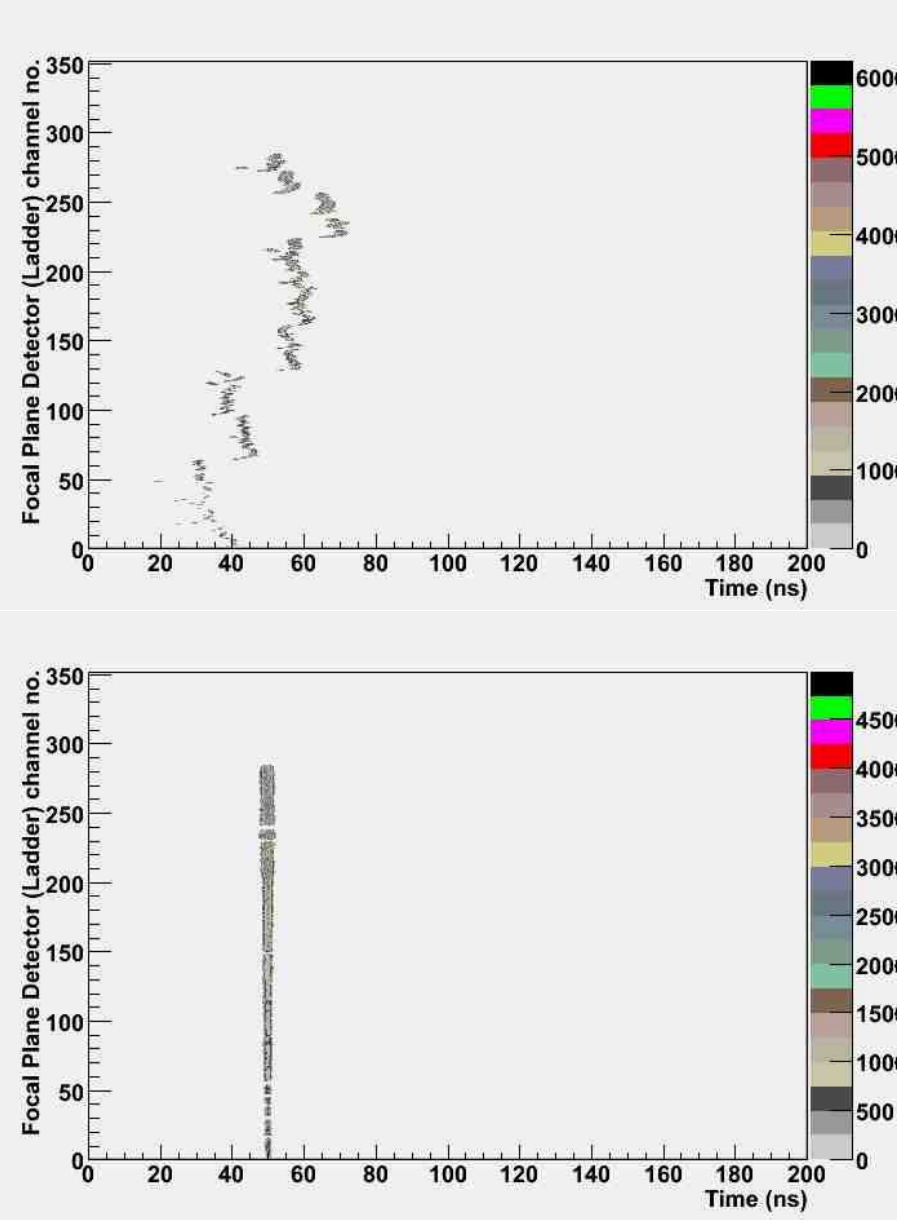

Figure 5.3: Unaligned (top) and aligned (bottom) Tagger time spectra.

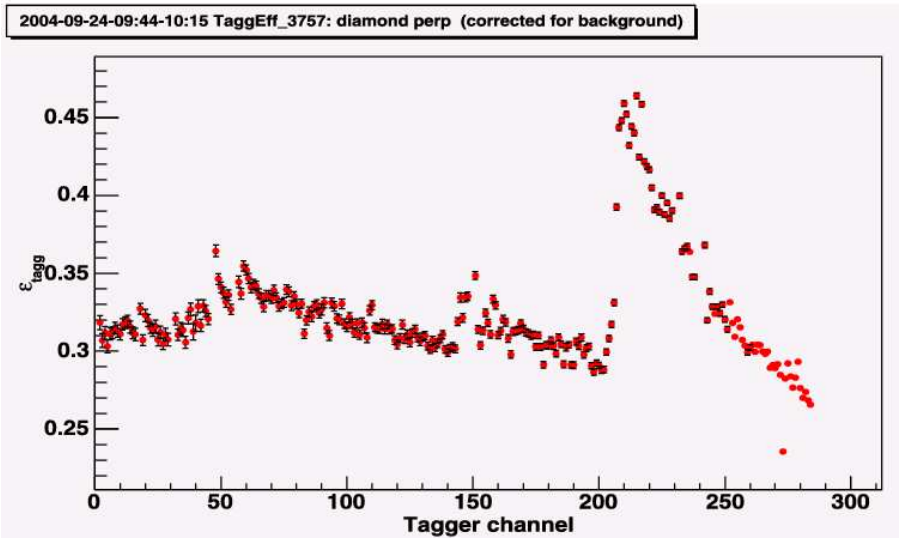

Figure 5.4: Tagging efficiency $\varepsilon_{tagg} \pm \delta_{\varepsilon_{tagg} stat.}$ *vs.* FPD channel number for a typical polarised photon data file with a 3 mm diameter photon beam collimator with the polarisation peak set at 400 MeV.

efficiency runs. This was subtracted from the FPD's beam-on counting rate:

$$\varepsilon_{tagg}[i] = \frac{N_{\gamma}[i]}{N_{e^-}[i] - N_{bkgnd}[i]} \tag{5.3}$$

where $N_{bkgnd}[i] = \frac{t_{beam-on}}{t_{beam-off}} N_{off}$, t being the time that the beam was switched on or off, respectively and N_{off} being the number of counts observed when the beam was switched off. By accumulating and correcting data in this way, calibration files can be produced for each experimental beam-time, with the tagging efficiency and uncertainty for each of the 352 FPD channels. A plot of this can be seen in Fig. 5.4.

5.2.3 PID Calibrations

The Particle Identification Detector was calibrated in energy, time and position using a set of ROOT macros prototyped by E. Downie [58]. The calibration procedure was performed and monitored by the author.

PID calibrations were performed using several data files - around eight - from the start of each experimental beam-time and then checked with a similar number of files from the end of the same beam-time. As with the other detectors used, calibrations were performed every time the run conditions changed,

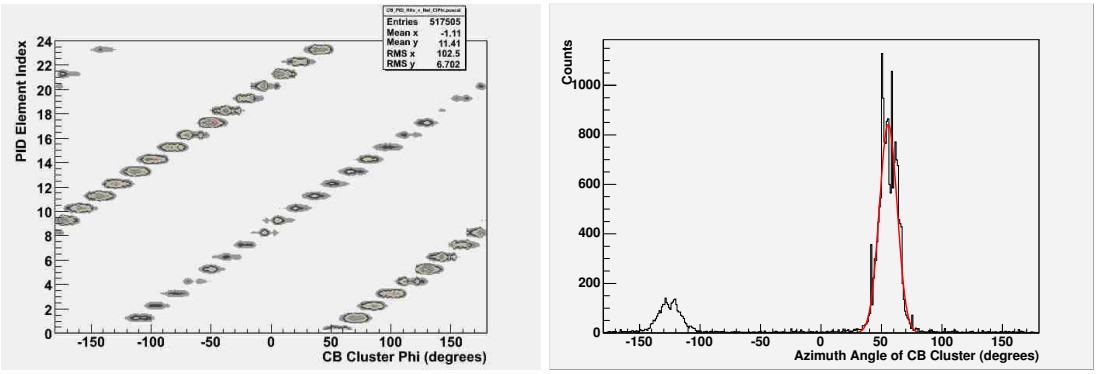

Figure 5.5: PID Hits *vs.* CB ϕ (left) and Gaussian-fitted projection for element 1 (right). The smaller 'back-to-back' signal is due to a charged-uncharged particle pair being produced but not being detected by standard means. In this case, the uncharged reaction product is detected in the CB while the charged particle is not, possibly due to its energy - it stops between the PID and the CB thus only leaving an energy deposit in the CB.

e.g. a new beam-time, a different target being used, different MAMI beam energy, trigger condition and so on. The PID calibrations are relative; a new file is produced based on the values contained in the input file, which was generally the one used for the previous beam-time or set of run conditions.

5.2.3.1 Position

A position alignment should be performed whenever it is suspected that the PID may have moved with respect to the CB, when the target is changed, for example. In reality, the positional alignment was checked for each beam-time and was found to change very little.

The procedure consisted of ensuring that the centres of the PID elements were in fact 15 degrees apart in ϕ as should be expected from the geometry of the detector; the PID elements were designed to have exactly this azimuthal angular coverage. A plot of PID hits vs. CB azimuthal angle ϕ is projected onto the ϕ axis for each element and a Gaussian distribution fitted to the resulting peak (Fig. 5.2.3.1). The positions of the means of these peaks are plotted and fitted with a straight line to ensure that they are 15 degrees apart as expected. Once this has been done, these means are written to a new PID AcquRoot setup file as the new ϕ positions of the PID element centres. This process is depicted in Fig. 5.2.3.1.

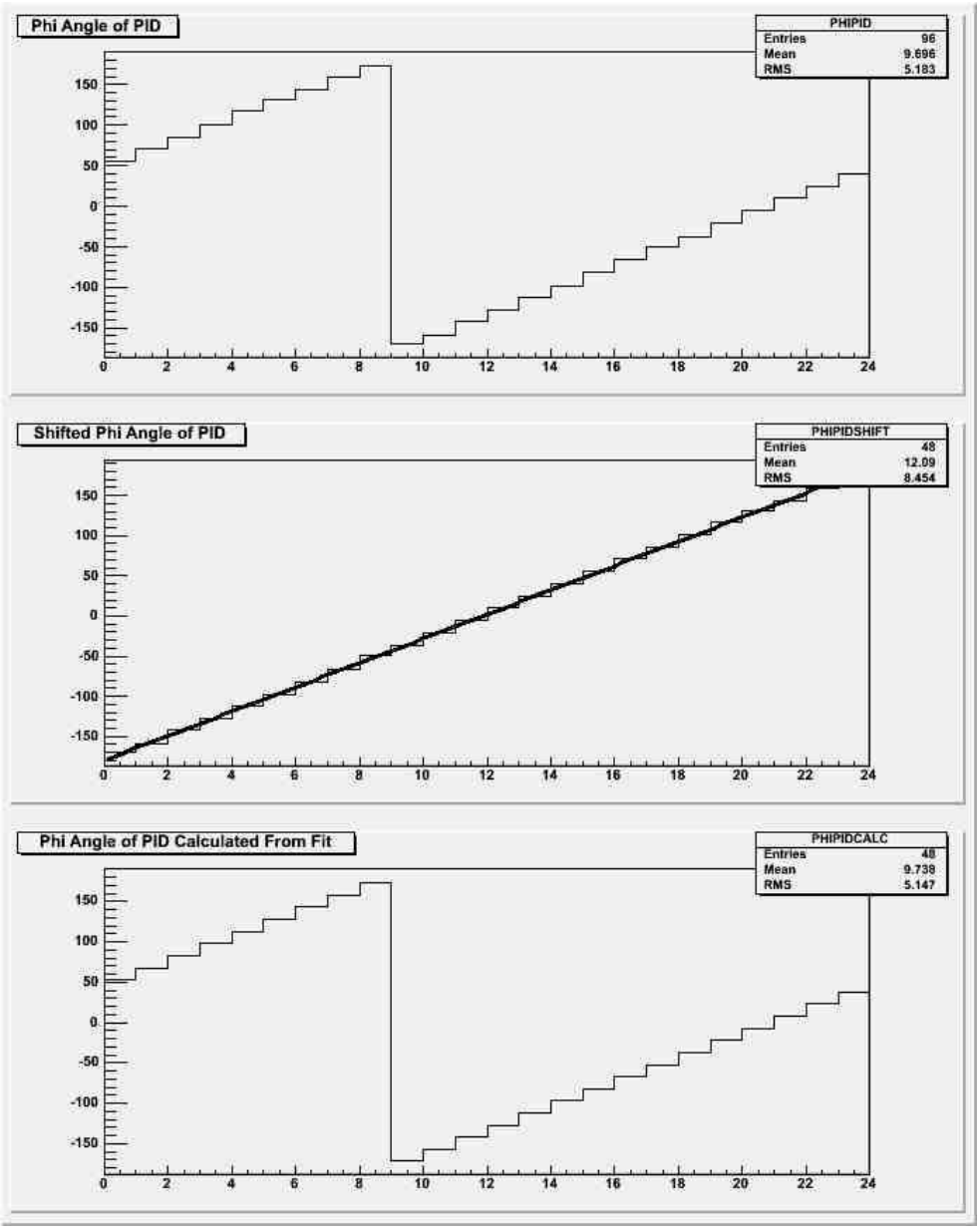

Figure 5.6: Plots showing the PID asimuthal position calibration.

Top: PID element ϕ angles acquired from CB angular information - see Fig. 5.2.3.1.

Middle: PID elements arranged in order of increasing ϕ and fitted with $m = 15$ straight line.

Bottom: Calculated angular offsets rearranged in original order.

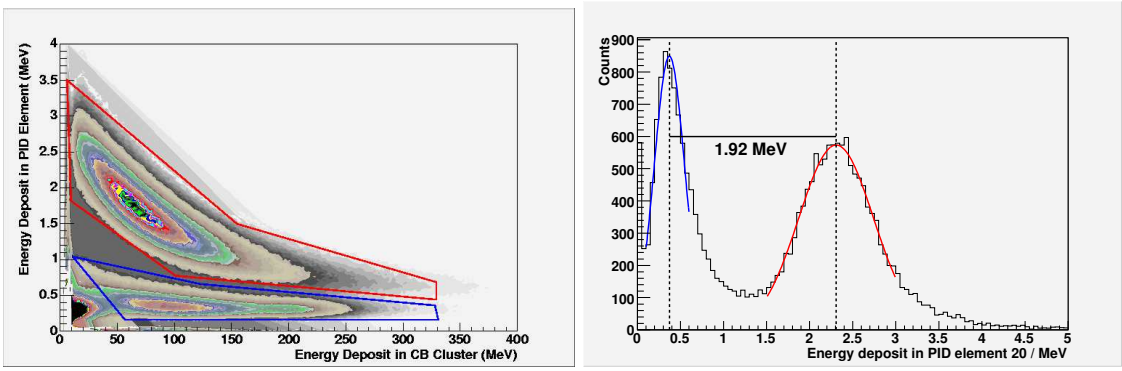

Figure 5.7: Typical E *vs.* E plot (left) and its projection (right), showing the fitted Gaussian distributions and their separation.

5.2.3.2 Energy

To calibrate the energy, the PID's output was compared to that of the GEANT3 Monte-Carlo simulation (see section 5.6 for a full description of this) in order to calculate the MeV per channel conversion gain.

The energy calibration for each PID element is based on its δE vs. E plot. Projections are made onto the PID energy axis for CB energy deposits of between 32 - 48 MeV. Projections are made onto the PID energy axis and Gaussian fits are then made to the two peaks, one each for the pions and protons. The fit ranges are checked to ensure they adequately cover the projected peaks - see Fig. 5.7. The separation of the means of the two Gaussian peaks is then checked for each element - 1.92 MeV according to the simulation - and thus an energy calibration factor (MeV / channel) is calculated using the relation:

$$G = g \times \frac{\bar{p}_{sim.} - \bar{\pi}_{sim.}}{\bar{p}_{expt} - \bar{\pi}_{expt}} \tag{5.4}$$

This new calibration factor, G, is written to a second new calibration file, having read in the file already containing the positional information as calculated in section 5.2.3.1 and the old energy calibration factor, g, upon which G is based.

5.2.3.3 Timing

Pre-processing of the timing signals for each PID element consisted of simply aligning all the times to zero, the offsets needed to achieve this being written to a third and final PID calibration file which

includes position, energy and timing information.

Gaussian distributions are fitted to all 24 of the individual PID element time spectra and the means of these aligned to zero. The ns/channel gain shift required to do this for each element is saved to a final AcquRoot setup file, again having first read in the most recently created PID configuration file containing position and energy calibration factors. Having done this, the final 'PID.dat' file now boasts position, energy and time information as mentioned above, and is ready for use in offline AcquRoot Physics analysis.

5.2.4 CB Calibrations

The Crystal Ball detector was calibrated in terms of energy and time. This work was done by J. Brudvik (UCLA), Appendix A of [59], and M. Unverzagt (Mainz) [60].

5.2.4.1 Pulse Height

As a precursor to performing a calibration with beam, based on pi0 production on the proton, an $Am^{241}Be^{9}$ source was used to roughly equalise the gain of each PMT. The procedure involved placing the $Am^{241}Be^{9}$ source in the centre of the Crystal Ball (in a borated polyethylene container) and observing the emitted 4.438 MeV photon produced when the alpha particle emitted by an Am^{241} decay combines with the Be^{9} to form a neutron plus an excited state of C^{12} which then relaxes. The Am decay also produces a spectrum of neutrons with ~few keV $< E_n <$ ~10MeV, which would appear as noise in the detector outputs, were it not for the container attenuating them. Crystals were looked at in groups of 16, with a Total Energy discriminator threshold of 6mV (roughly 10 MeV, but it should be remembered that this work was done before the CB was properly calibrated in energy). The triggering was done on the basis that if the sum of the 16 crystals had a signal above threshold, all were read out. The background was fitted and subtracted using ROOT and the position of the photon peak was compared to that of the signal's pedestal location. The average of this distance over all crystals was calculated and those showing large deviations from this value had the voltage dividers on their PMTs adjusted manually.

5.2.4.2 Energy

Energy-calibrating the CB was done by analysing the reaction $\gamma p \rightarrow p\pi^0$ [59], the procedure used is outlined in section D.3. The PID and wire chambers were used to identify the proton and the Crystal Ball to reconstruct the neutral pion. The procedure was to compare the ratio of the measured and expected photon energies from the decay $\pi^0 \rightarrow \gamma\gamma$ to reconstruct the π^0 total energy in the lab. frame of the pion, then apply a Gaussian fit to these distributions. The new calibration factor, G (MeV/channel for each crystal) was produced using the mean value of this fit:

$$G = g \times \overline{Gaus.} \tag{5.5}$$

The procedure was performed in an iterative manner starting with a value averaged over all of the CB crystals, g. This was to eradicate any effects caused by the fact that any particular photon's energy can be spread among several NaI crystals in the CB, thus affecting the gain of the crystal in the centre of the cluster. After repeating the process an average of four times, the gain value was not observed to change significantly.

5.2.4.3 Timing

Precise timing in CB elements is required in order to make accurate correlations between incoming tagged photons and products of $\overrightarrow{\gamma}p$ reactions. As signals in NaI have a rise-time of ~100ns, the leading edge discriminators give a timing uncertainty of this order. Because larger signals will cross the discriminator threshold sooner than smaller signals, a range of start times is observed (Fig. 5.2.4.3). This spread in timing, $\delta t = t_2 - t_1$, is called 'walk' and has to be more accurately corrected for to allow the signals in the CB crystals to be accurately correlated in time with the other items of apparatus.

To determine the walk corrections - which will vary slightly for each crystal - a parameterised polynomial fit is applied to plots of Time vs. Energy for each of the 672 NaI CB elements. The parameters in this instance were chosen to be the discriminator energy threshold E_t, the rise-time t_r, and the degree of the polynomial n. This yields the required timing correction t_c:

$$t_c = t - t_r \left(1 + \frac{E_t}{E^n}\right) \tag{5.6}$$

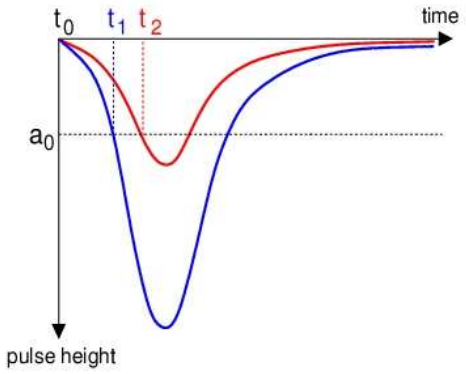

Figure 5.8: Plot showing the spread in timing for different pulse heights.

The various points to note are:

a_0: Leading Edge Discriminator (LED) threshold.

t_0: Signal start time.

t_1: Time at which a large signal crosses a_0.

t_2: Time at which a small signal crosses a_0.

Detector	START signal	STOP signal
TAGGER	FPD element	Trigger
CB	Trigger	NaI element
TAPS	BaF_2 element	Trigger

Table 5.1: Summary of timing signals used for read-out.

and the results for a typical CB element can be seen in Fig. 5.9, in this case for eqn. (5.6) with $n = \frac{1}{2}$. Slight improvements can be seen for other values of n but $\frac{1}{2}$ was generally found to be good enough for our purposes. As the walk correction as implemented in AcquRoot requires the rise-time for each NaI crystal to be entered, these values are extracted and included in the AcquRoot CB apparatus's NaI detector configuration file.

Once the walk has been dealt with, the question of aligning the times of the NaI crystals can be addressed. Some consideration is required of how the different detectors work in terms of timing, which is taken with respect to the triggers, each of which has a 'START' and 'STOP' component. For the Tagger and the CB, the START signals come from the FPD and the experimental trigger (provided by the Tagger) respectively. The STOP signals are provided by the trigger and a signal in the CB, meaning that the time difference between the CB's NaI elements and the Tagger's FPD with respect

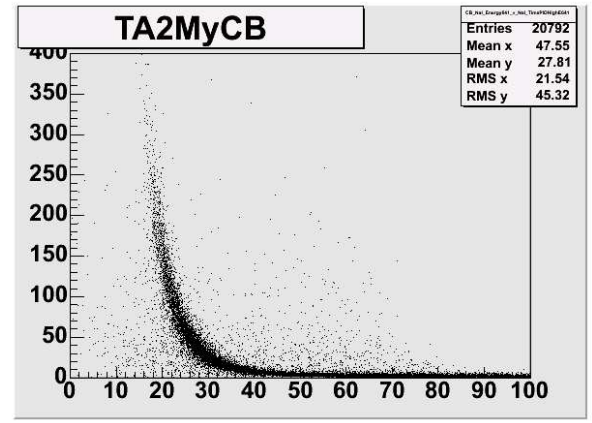

(a)

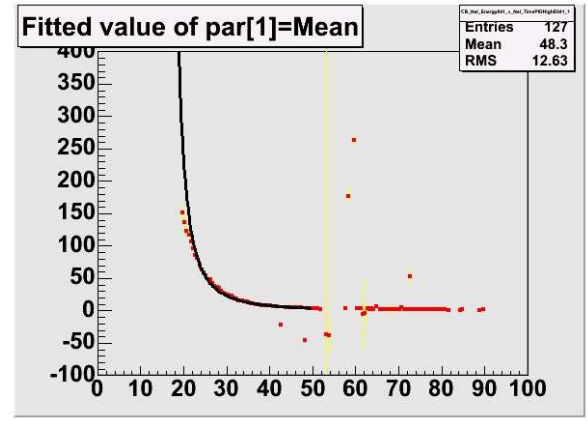

(b)

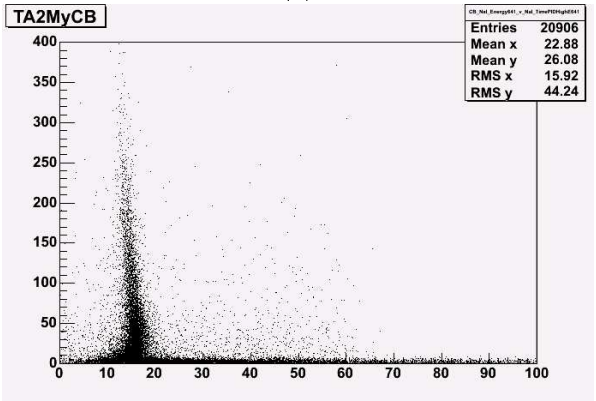

(c)

Figure 5.9: CB walk corrections: raw Energy *vs.* Time spectrum (a), fitted data (b), walk corrected E *vs.* t spectrum (c). The fit in (b) shows the effect of setting $n = \frac{1}{2}$. The final walk correction algorithm left n as a free parameter leading to a better agreement between the fit and the data than is shown here.

to - and eliminating - the experimental trigger, eqn. (5.7) is given by:

$$t_{CB-TAGGER} = (t_{TRIGGER} - t_{CB}) + (t_{TAGGER} - t_{TRIGGER}) = t_{TAGGER} - t_{CB} \quad (5.7)$$

This also improves the timing resolution as the trigger timing pulse width is eliminated. The difference between each of the 672 CB elements and the aligned Tagger is taken and this value used to correct the signals from the NaI crystals. A projection of these aligned times is in turn compared to each of the Tagger's FDP time signals in order to obtain, in an iterative manner, the best possible timing resolution. Usually, around two iterations were made before no further improvement was seen.

5.2.5 TAPS Calibrations

Like the other experimental detectors, TAPS was calibrated both in energy and time so that particle ID and momentum could be extracted. The Pulse-Shape Analysis (PSA) method of identifying different particle species for the forward wall, as well as the energy calibrations for TAPS were performed by Ralf Gregor [61] and Stefan Lugert [62], both from the Justus Leibig University in Giessen, Germany. A procedural overview, together with some choice plots, is presented below.

The TAPS energy calibrations were performed by Benedict Boillat of Basel [63] using cosmic-ray measurements which were taken at the beginning and at the end of each experimental beam-time in order to check that there were no large drifts in output over the course of running. The Energy calibration was based on determining the positions of both an applied pedestal pulser and observing the position of the peak in the cosmic ray spectrum.

Timing alignment was performed by Fabien Zehr, also of Basel [64], and for this a similar method to the alignment of the CB was utilised; the signals from the TAPS BaF_2 crystals were aligned with each other and then with respect to other experimental detectors.

5.2.5.1 Pulse-shape

BaF_2 has two scintillating components, a fast component and a slow component. Using this ratio, one is able to distinguish photons from Hadrons. The relative strength of these components, and thus their

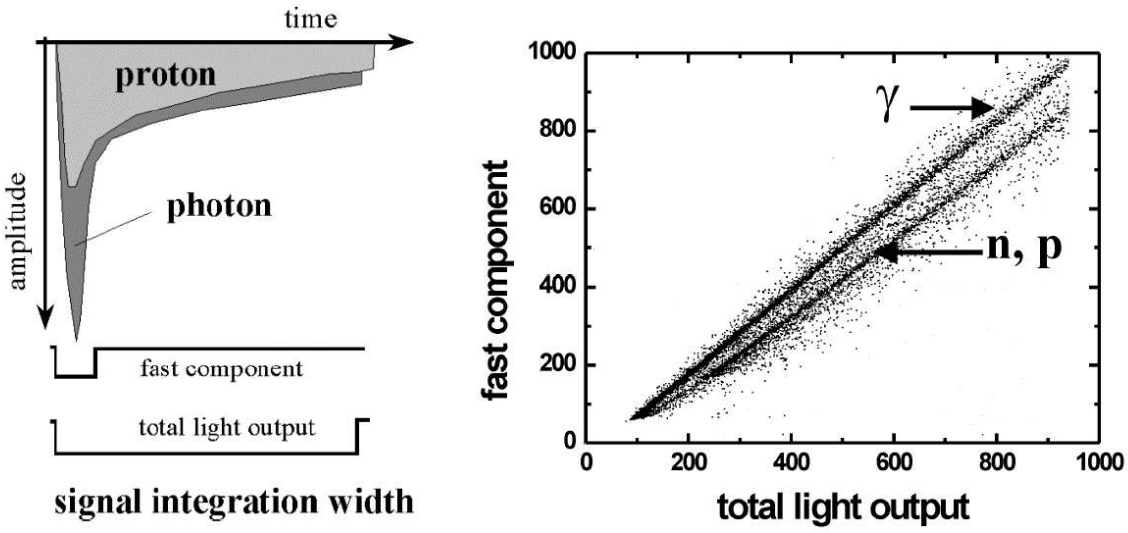

Figure 5.10: Linear plot of E_S *vs.* E_L.

contribution to the total light output, depends on the velocity of the interacting particle. Relatively slow particles e.g. protons have proportionally less fast component than fast pions or relativistic electrons. The fast and total (fast+slow) scintillation components are recorded by integrating the PM signal in QDCs with input gate widths of 30ns and 2μs. Plotting the energy deposition of the short component E_S against the long component E_L, one is able to separate different types of particles as they have different loci in this 2D space - see Fig 5.10. Alternatively one may to plot the pulse shapes in polar coordinates. Here the distance (radius) R between any point and the origin is plotted against the angle (ϕ) subtended with respect to the x-axis, as calculated by eqns. (5.8) and (5.9).

$$R = \sqrt{E_S^2 + E_L^2} \tag{5.8}$$

$$\phi = arctan(E_S^2 E_L^2) \cdot 180^\circ \cdot 2\pi \tag{5.9}$$

In an ideal calibration the photons should be located at $\phi = 45^\circ$. Due to slight uncertainty in the determination of the short component energy due to its effective integration length of 30 ns, a slight divergence from the ideal signal pulse form is observed.

The pulse shape analysis was done by taking slices of the polar representation of the $E_S$vs. E_L plot (figure 5.11) at values of radius 0, 10, 20, 30, 40, 60, 90, 130, 200, 280, 360, 420 and 535 MeV (see the magenta lines shown on the y axis of Fig. 5.11) and projected onto the x axis. The resulting plots

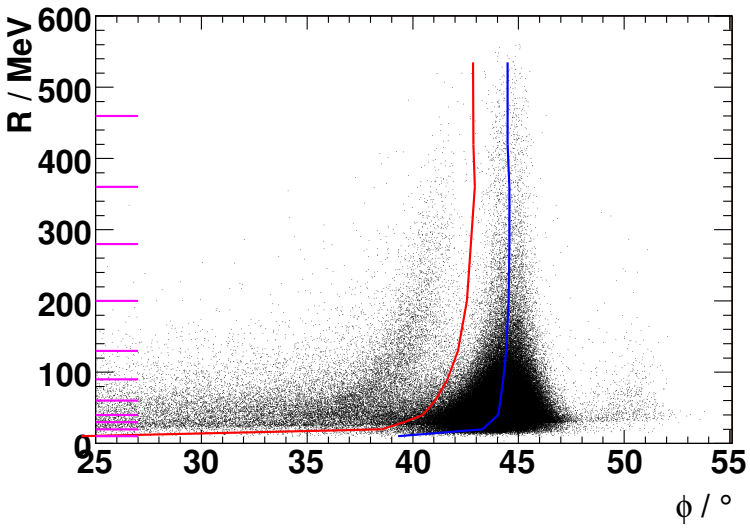

Figure 5.11: Polar representation of E_S *vs.* E_L.

(see figure 5.12 for a typical example) were interpreted the following way: the projection is fitted by two Gaussian distributions superimposed on a linear background. A particle is selected by placing a 3σ cut about the PSD peak. These fits are shown on figure 5.12, the red and blue lines respectively. Particles lying to the left of the blue line are Hadrons, those on the right hand side (depending on the VETO information) are photons or electrons. With this information, one is able to determine an individual cut line for each detector. Using this cut, one is able to select photons or Hadrons for further analysis. Usually the 3σ interval below the peak position (blue line) is recognized to be photons, and, in principle, every angle above this peak position can be neglected if one is looking for protons. For further analysis, only the photons were identified using the 3σ cut. It should be noted that distinguishing mesons is currently impossible in TAPS. Therefore, for the present $\pi^+ + n$ analysis, TAPS only contributed information to the data set when the neutron was seen in TAPS, coincident with a π^+ detected in the CB.

5.2.5.2 Energy

The combination of BaF_2 crystal, PMT and electronics delivers a linear relationship between energy and pulse height, and therefore one needs just two known energy points to determine the two calibration factors: gain and offset. The gain is given in units of MeV/Channel, the same as for the other detectors,

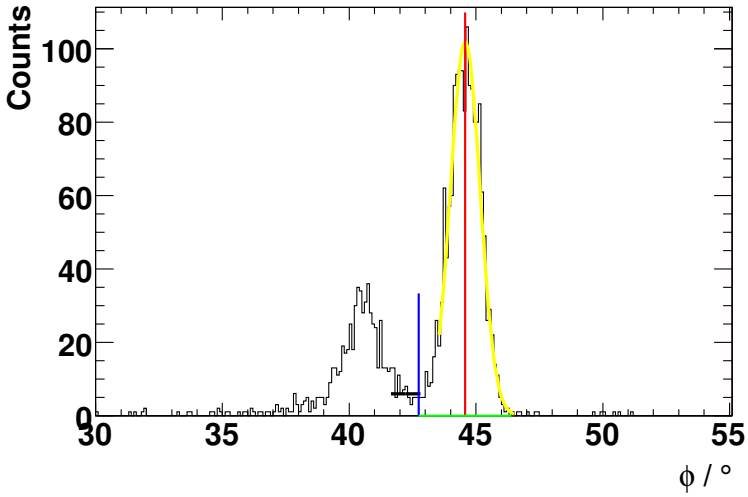

Figure 5.12: A typical projection of E_S *vs.* E_L onto the polar (ϕ) axis.

and the offset corresponds to the pedestal signal (the large spike appearing at around channel 100 on a typical TAPS ADC spectrum - Fig. 5.13. In order to have precise control of the pedestal position, an electronic pulse-trigger uncorrelated with the PMT signals is used and with this the position of the channel corresponding to 0 MeV is determined. This is the first of the two required energy points. The other energy point is given by the cosmic-ray induced peak corresponding to the energy deposition of minimum-ionizing muons. This value was, for the BaF_2 crystals, determined to be 37.7 MeV. The determination of the pedestal offset was made by taking by the index of the ADC channel containing the highest value in the initial spiked peak. The determination of the cosmic peak position is reached by fitting a Gaussian distribution superimposed on a decaying exponential as shown in figure 5.14.

5.2.5.3 Timing

The TAPS time calibrations were performed in a similar way to the Glasgow-Mainz photon tagger: an alignment of all of the time signals to one specific value by way of calculating the offset from this value. The time value chosen was that of the Tagger and thus the offsets calculated are equal to $t_{TAPS} - t_{TAGGER}$. In a similar manner to the alignment performed for the CB, it can be seen from table 5.1 that the START signal comes from individual detector elements (the FASTBUS TDCs for the Tagger and the CFD for the BaF_2) and the trigger provides a common STOP. For determining the time between TAPS and the Tagger with respect to - and eliminating - the experimental trigger,

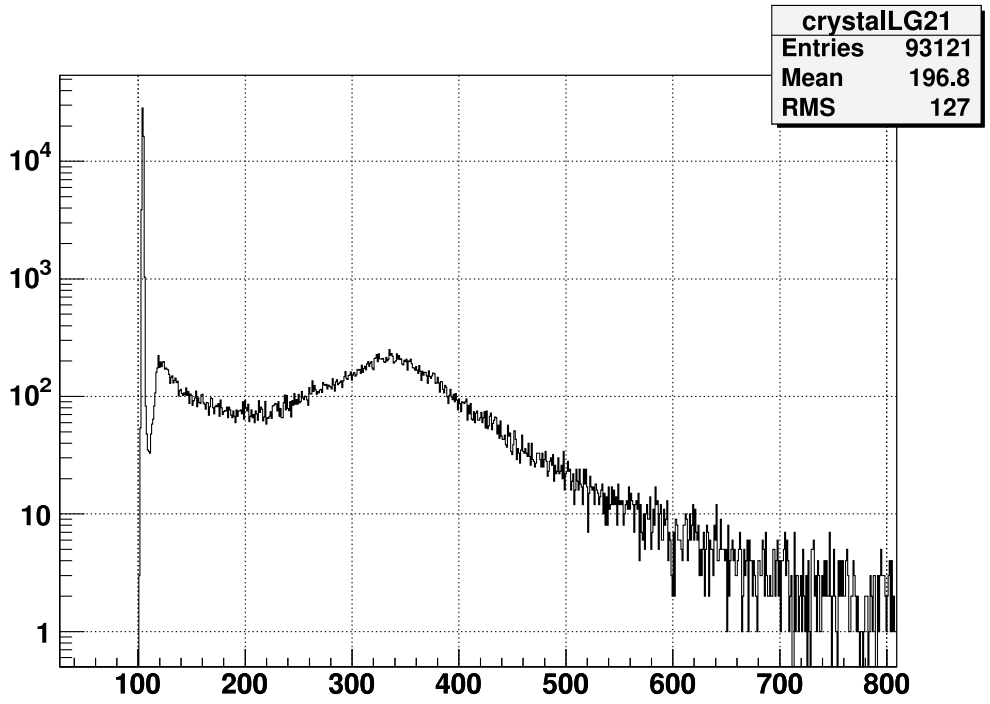

Figure 5.13: Example of a typical cosmic-ray induced signal in a TAPS ADC.

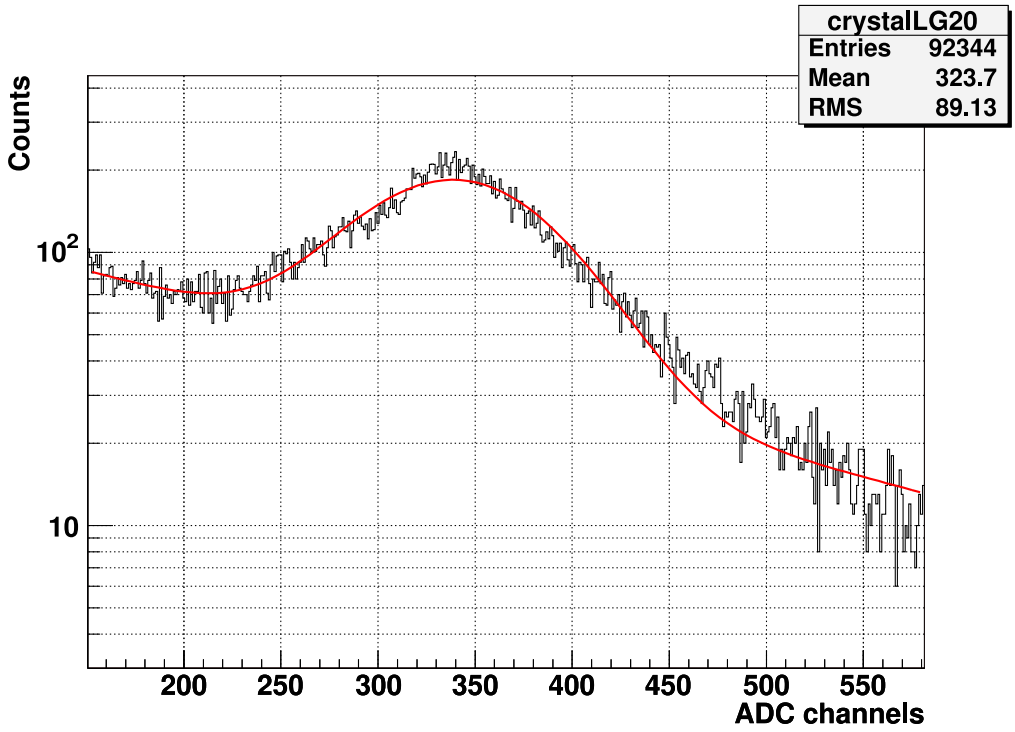

Figure 5.14: Fitted TAPS cosmic ADC spectrum.

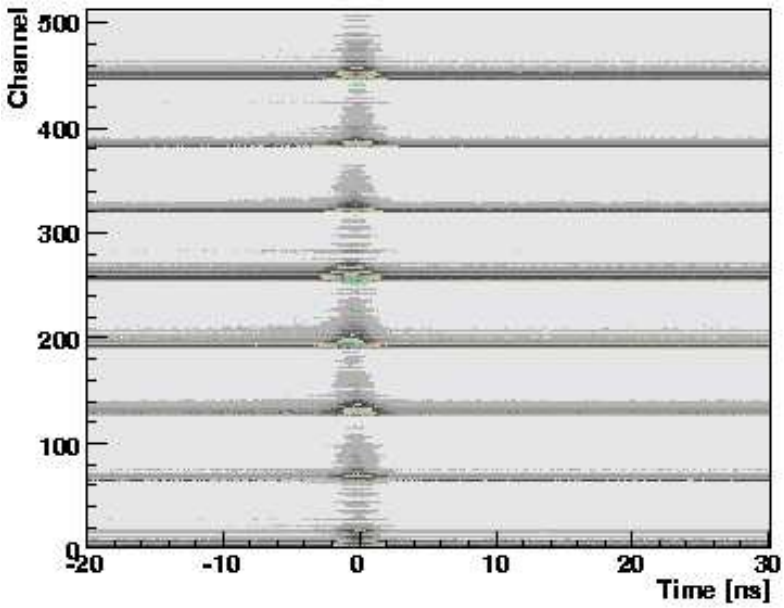

Figure 5.15: The TAPS timing alignment for all BaF_2 crystals.

eqn. (5.10) is used:

$$t_{TAPS-TAGGER} = (t_{TRIGGER} - t_{TAPS}) - (t_{TRIGGER} - t_{TAGGER}) = t_{TAGGER} - t_{TAPS} \quad (5.10)$$

Taking the difference between the tagger and each of the detectors provides a calibration factor that is written into the BaF_2AcquRoot setup file, using the same iterative procedure as used for the CB (section 5.2.4.3). The aligned TAPS crystal's time spectra can be seen in Fig 5.15.

Once all the various calibrations have been performed, the real business of analysing the data to produce Physics results from the $\overrightarrow{\gamma}p \rightarrow \pi^+ n$ reaction can begin. The first stage of this is to acquire the signal; the final state particles required to reproduce the expected reaction. Producing the signal was done by first identifying the π^+, then obtaining the missing energy associated with it, which should be equal to the mass of the neutron. This procedure is fully discussed in section 5.4. Before this, however we need to be certain that any interaction registering as a real event was in fact initiated by the real photon with the correct energy and timing coincidence rather than another random 'hit' on the Tagger focal plane detector.

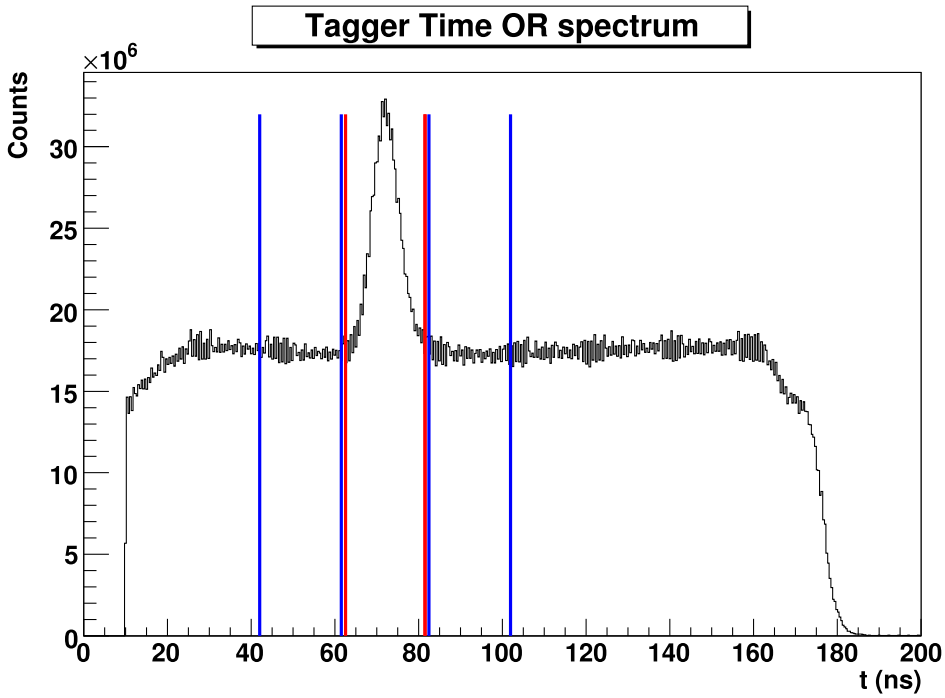

Figure 5.16: Typical Tagger time spectrum showing prompt (red lines) and random regions (blue lines) as selected in the data analysis.

5.3 Tagger Prompt and Random regions

In any particular event that passes the various hardware and software trigger conditions, energy thresholds and data cuts, there can be several tagger channels that are triggered and thus potentially relate to a photon that induced the event. We want to accept only the photons responsible for producing the final state particles - the so-called 'prompt' photon - and reject the other, random coincidences produced by electrons whose corresponding Bremsstrahlung photons are not coincident in time with the required reaction products. The prompt peak can be clearly seen, centred around 72ns - see figure 5.16 - sitting on top of an approximately flat background. It is photons in the peak from which we want to identify the reaction products and so a simple correction is applied to subtract the random background.

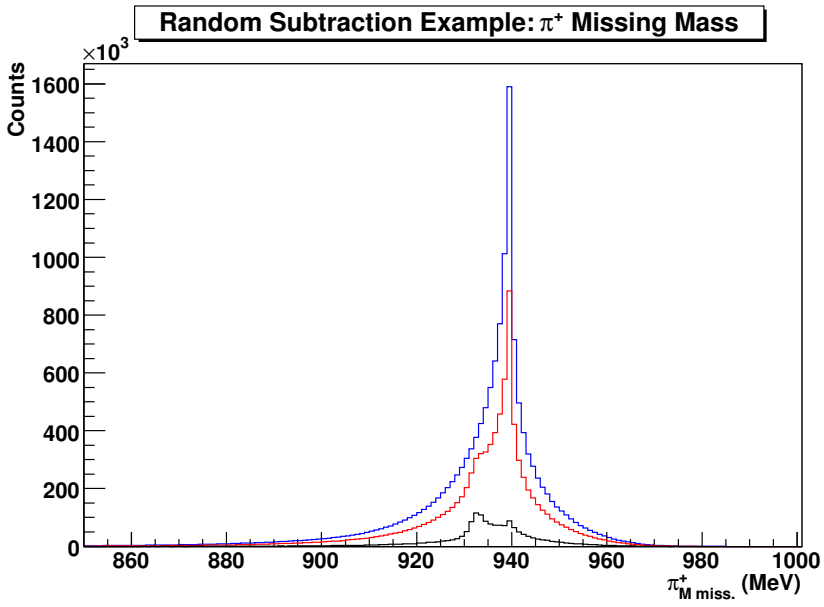

Figure 5.17: Example plot showing prompt (red), random (blue) and random-subtracted (black) experimental data, the quantity in question being $\pi^+_{Mmiss.}$ as used to identify the neutron.

5.3.1 Random Subtraction

Random subtraction is done by setting regions - so-called 'windows' - on the Tagger timing spectrum; a sample of random coincidence photons is obtained which are then subtracted from the peak region, which initially contains prompt and random photons, leaving only the prompt photon peak events for further analysis. These windows are shown in figure 5.16. The random window is set wide, typically twice as large as the prompt so as to have have twice the channel space. They are set close to the prompt to attempt to minimise systematic uncertainty in the subtraction. Before the subtraction is performed in an AcquRoot offline analysis session, it is scaled to be equal to the width of the prompt window. The selection of the peak in the Tagger time spectrum is possible due to the fact that the time spectra for each of the 352 FPD channels were aligned during the calibration phase (section 5.2.1.2). In the results file produced by the AcquRoot offline analysis, two sets of histograms are produced for each variable, with suffixes 'P' and 'R' depending on which window the events fall into. To get the final signal the random (R) events are subtracted fro the prompt (P). This is illustrated in Fig. 5.17 below, the quantity being illustrated is the incident photon signal.

5.4 Particle Identification and Event Selection

TAPS covers polar angles of between 2 and 22 degrees in the laboratory frame, the CB covering between 22 and 157 degrees. Particle identification for TAPS comes from the Pulse-Shape Analysis discussed above, in section 5.2.5.1, while species discrimination in the Crystal Ball is achieved from correlations of energy deposits with respect to the PID located in its centre. In order to select the products, a π^+ and a neutron expected from the $\overrightarrow{\gamma}p$ reaction, it was chosen to 'tag' the reaction using the π^+. The reason for this was that, despite the fact that the CB and TAPS were originally designed with photon detection in mind, the PID allows the π^+ to be effectively selected in the CB. The reaction is reconstructed from the π^+ missing mass, if this is equal to the mass of the neutron. At the time of writing, it was impossible to distinguish charged pions in TAPS ($\theta_{\pi^+}^{Lab.} < 22^\circ$) and so ultimately less complete angular coverage than was originally hoped for was achieved. It is hoped that by the time MAMI-C data comes to the analysis stage, charged mesons will be distinguishable at forward lab. θ angles.

For reference, for the alternate reaction channel $\overrightarrow{\gamma}p \rightarrow \pi^0 p$, final state identification is achieved by selecting the two pion decay photons then reconstructing the proton missing mass. This approach effectively utilising the excellent photon detection capabilities of the detector crystal materials to confirm the location of the proton without having to rely in it interacting hadronically - with much lower detection efficiency - with the crystals. If the proton is also detected (confirmed by the PID and MWPCs in conjunction with the CB) then the reaction kinematics are said to be 'overdetermined'.

5.4.1 π^+ Detection

The π^+ was identified by first looking at the δE vs. E plots (PID energy vs. CB energy) with charged pions appearing in the region bordered by the blue line in figure 5.18. It should be noted that it is impossible to tell a π^+ from a π^- with the experimental detectors alone; the distinction between them comes from consideration of the allowed reactions or other detected particles. The observation of a π^+ is confirmed by seeing a cluster of the expected size and shape caused by a nuclear interaction between the π^+ and the NaI detector material in the CB (E) directly behind a PID element (δE). This will give a data point on a plot of δE vs. E (figure 5.18). From preliminary analysis, the best resolution is achievable by limiting the cluster size to 4 CB crystals to eliminate the effects of subsequent muon

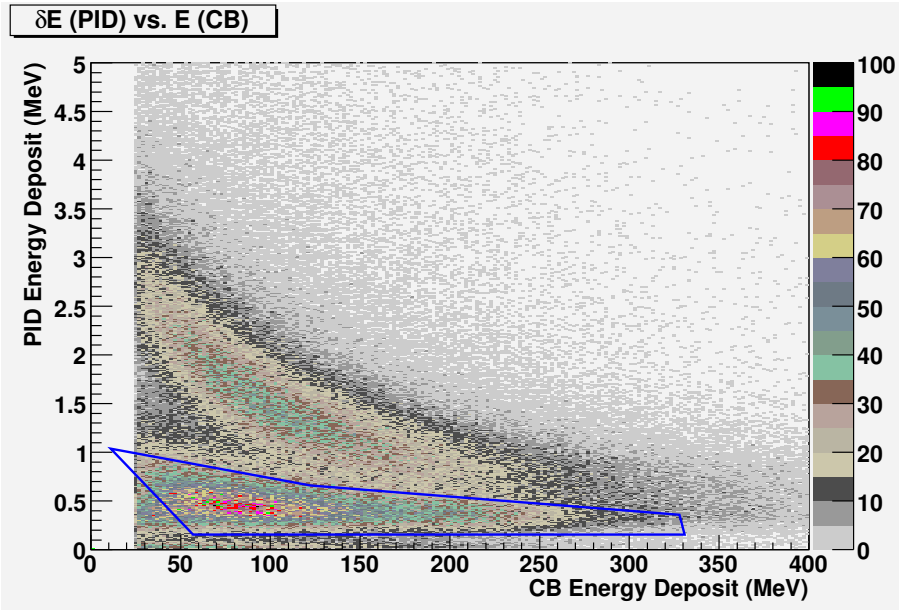

Figure 5.18: δE *vs.* E plot showing the polygon which determines the limits of the pion locus.

decay ($\pi^+ \rightarrow \mu^+\nu_\mu$) [65]. As mentioned above, for this experiment it was impossible to distinguish a π^+in TAPS and so all results will be for final states where the pion was detected in the CB and the neutron seen in the CB or TAPS.

5.4.2 Neutron Detection

Neutrons are detectable both in the CB and TAPS detectors. The CB detects neutrons by way of Hadronic interactions with the NaI detector material, which it does with an efficiency of around 20% at E_K= 50MeV rising to ~40% at E_K= 250MeV [66]. TAPS detects hadrons in the same way as the CB, by relying on a hadronic interaction between the incident neutron and the detector material, in this case BaF_2. The distinction between the two is made by Pulse-Shape Analysis (see 5.2.5.1) and the fact that a neutron will not have an associated veto detector hit, thus identifying it as an uncharged hadron.

Once the π^+ has been successfully identified, we need to look for the neutron which completes the required two-body final state. This is done by looking at the pion's missing mass spectrum. This missing mass, in this case, was taken to be any neutral cluster identified in coincidence with a charged pion. This missing mass was then compared with the measured momentum of the candidate neutron.

The M2 trigger condition ensured that events with this characteristic - two final state particles - were recorded. Once the neutral clusters have been identified, it is necessary to decide which one corresponds to the neutron that is required for full event reconstruction. To do this we look to check that we can see a neutral cluster directly opposite the π^+ in the CM frame. This assumes two-body kinematics, as described in Appendix D.

Given the incident photon energy and the angle of the emitted pion, the two-body calculation returns the expected π^+ momentum $\mathbf{p}_{\pi^+}$. Its total energy is then calculated as being:

$$E_{\pi^+} = \sqrt{\mathbf{p}^2_{\pi^+} + E^2_{0_{\pi^+}}} \tag{5.11}$$

with $\mathbf{p}_{\pi^+}$, E_{π^+} and $E_{0_{\pi^+}}$ being the momentum, total and rest mass energies of the positively charged pion respectively. The energy component of the detected π^+ momentum four-vector is then set to be equal to the value of E_{π^+} calculated by the two-body kinematic From this, the π^+ missing momentum is determined by subtracting the momentum of the π^+ from the sum of momenta of the incident photon and the target:

$$\mathbf{p}_{miss.} = \mathbf{p}_\gamma + \mathbf{p}_t - \mathbf{p}_{\pi^+} \tag{5.12}$$

The missing mass is then extracted from eqn. 5.12 and should be comparable to the rest mass of a neutron. Fig. 5.19 shows the missing mass of the π^+ obtained in this way. Next, the polar and azimuthal angles, θ and ϕ, of any neutral clusters are compared to those of the missing four-momentum. The difference between the angle observed and 180 degrees - the ideal 'back-to-back emission' scenario in the CM reference frame - is calculated and the opening angle is noted. The neutral clusters that are the coincident neutrons will have an opening angle which is small. A plot of missing energy vs. opening angle is shown in figure 5.20, the obvious enhancement being the neutron in coincidence with the already identified π^+. To select the neutron peak and thus our reaction signal some conditions are applied to this plot: $910 < \pi^+_{Mmiss.} < 960$ MeV and $0^\circ < A_{open} < 25^\circ$. A_{open} is the angle between a neutral cluster as detected and that predicted by a two-body calculation. Now that we have our 'signal' we can go about producing the asymmetry which we seek.

The stages for this are:

i) Split the $\pi^+ n$ events into their photon beam polarisation states.

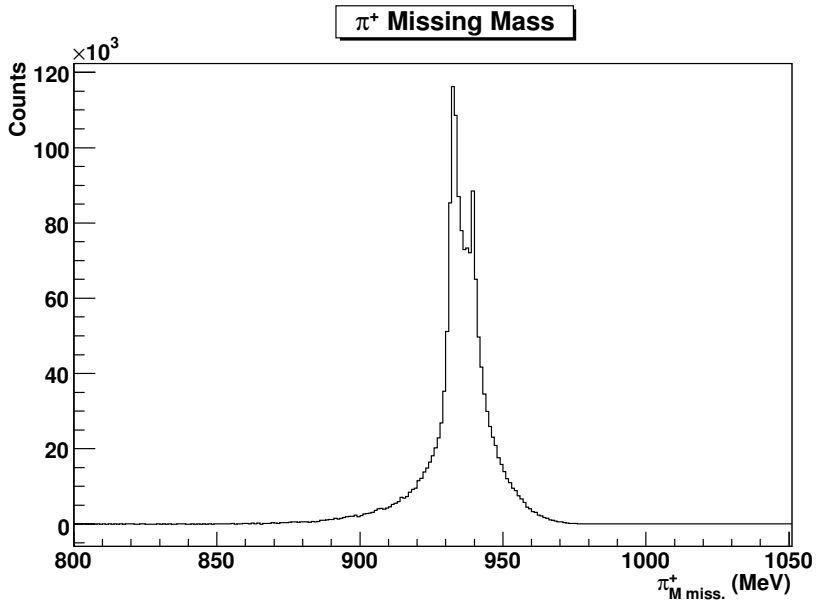

Figure 5.19: A typical $\pi^+_{Mmiss.}$ plot after random subtraction. The observed peak is centred around m_n as required. We take this to be the confirmation that we have indeed successfully identified our $\pi^+ n$ final state.

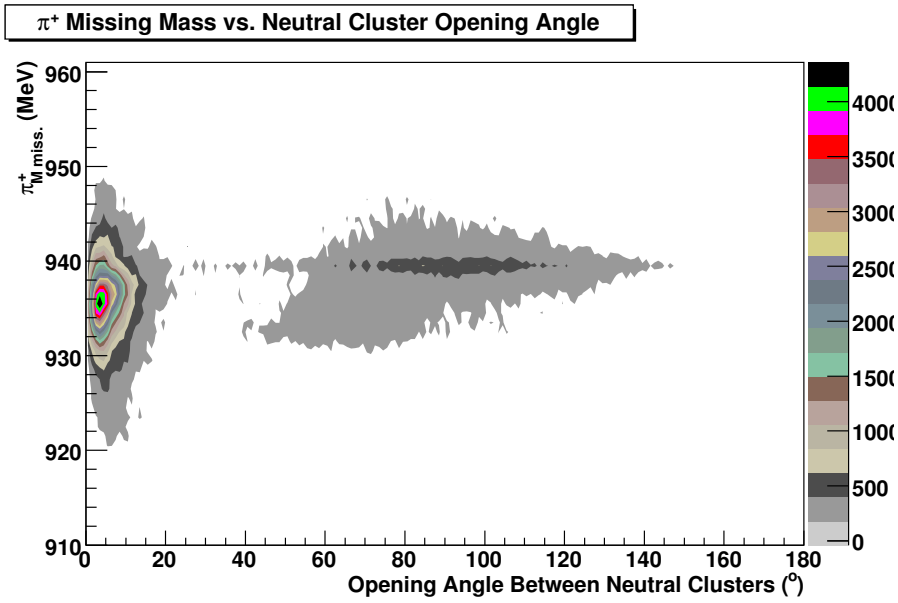

Figure 5.20: A typical $\pi^+_{Mmiss.}$ *vs.* A_{open} plot from which the n peak was selected. Ultimately, selection was perfomed by requiring that $910 < \pi^+_{Mmiss.} < 960$ MeV and $0° < A_{open} < 25°$.

ii) Produce ϕ distributions for the different $\theta_{\pi^+}^{CM}$ bins.

iii) Subdivide these binned-in-$\theta_{\pi^+}^{CM}$ ϕ distributions into incident E_γ bins, thus producing ϕ distributions and thus asymmetries in terms of E_γ and $\theta_{\pi^+}^{CM}$.

iv) Scale the $\cos 2\phi$ distributions by the degree of linear polarisation and photon flux in order to produce normalised $\cos 2\phi$ distributions.

5.4.3 Beam Polarisation Dependence

To produce photon asymmetries, events must be split into two groups, one corresponding to each of the polarisation states: parallel and perpendicular (abbreviated to '*para*' and '*perp*' respectively). The two polarisation orientations are orthogonal to each other and are taken with respect to the electron beam, to which the diamond radiator was aligned in the goniometer during experimental running. This positional reference is defined by the plane of the Tagger's FP detector which is parallel to the floor by design.

As mentioned above, each of the polarisation data sets was split into five angular bins in terms of $\theta_{\pi^+}^{CM}$, over the energy range corresponding to the highest observed polarisations of the incident photon energy spectrum. Bin sizes were chosen to allow a significant quantity of statistics to populate each. For $\theta_{\pi^+}^{CM}$ the bin size (width in terms of $\theta_{\pi^+}^{CM}$) was chosen based on observing the $\theta_{\pi^+}^{CM}$ angles at which reasonable of statistics had accumulated. The $\theta_{\pi^+}^{CM}$ range to be analysed was chosen to be between 30 and 160 degrees and this was divided into five bins of unequal width in order to ensure that reasonable quantities of statistics populated each one. The binnings chosen were 30° to 60°, 60° to 80°, 80° to 100°, 100° to 120° and 120° to 170° and are shown in Fig. 5.21.

Within each of these $\theta_{\pi^+}^{CM}$ bins 20MeV wide projections were taken from the E_γ ranges appropriate to the data set being analysed. From these ϕ_{π^+} distributions dependent on $\theta_{\pi^+}^{CM}$ and E_γ were produced. The E_γ ranges were chosen to be 300 to 400 MeV for those data files which had the enhancement peak set at 400MeV, and 340 to 440 MeV for the runs with the 440MeV polariastion peak. The E_γ region above the peak was not analysed as the polarisation varies rapidly (it drops off sharply above the peak) with respect to small changes in beam position. Asymmetries were then produced for each of these binning combinations, thus giving 25 measurements of Σ binned in $\theta_{\pi^+}^{CM}$ and E_γ for each of

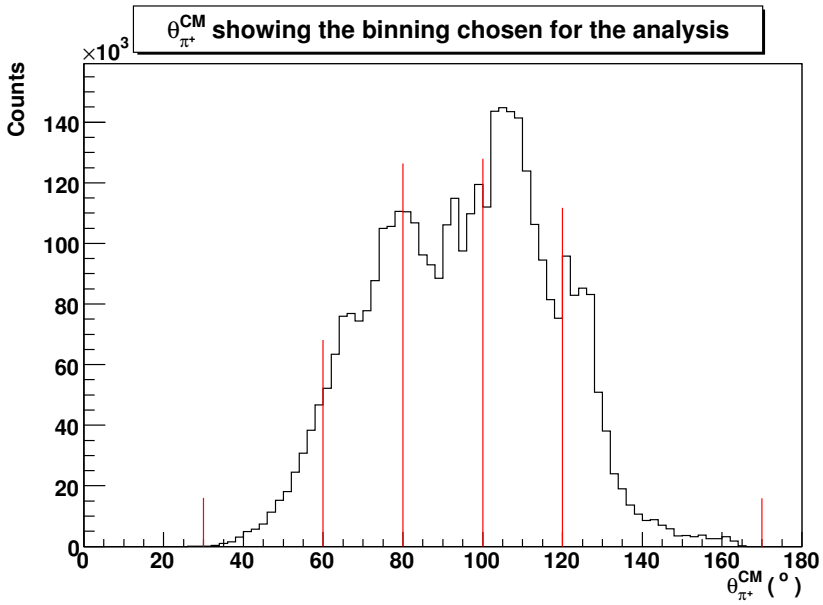

Figure 5.21: A plot showing the region in $\theta_{\pi^+}^{CM}$ populated by $\gamma p \rightarrow \pi^+ n$ events. The $\theta_{\pi^+}^{CM}$ bins used in the analysis are shown bounded by the red lines.

the two coherent peak energies investigated, E_γ= 400MeV and E_γ= 440MeV. These will subsequently be referred to as the 400 MeV data set and the 440 MeV data set.

5.4.4 Normalisation Considerations

Re-writing eqn. (1.1) with respect to the linearly polarised cross-sections as functions of ϕ: $\sigma_{\parallel}(\phi)$ and $\sigma_{\perp}(\phi)$; yields eqn. (5.13):

$$\frac{\sigma_{\perp}(\phi) - \sigma_{\parallel}(\phi)}{\sigma_{\perp}(\phi) + \sigma_{\parallel}(\phi)} = A\cos(2\phi - \phi_0) \tag{5.13}$$

Scaling the amplitude, A, to the degree of polarisation $P_{deg.}$ (eqn. (5.14)) gives the absolute value of Σ.

$$\Sigma = AP_{deg.} \tag{5.14}$$

5.4.4.1 Determining the Degree of Linear Polarisation

The absolute degree of the linear polarisation of the incoming photons is determined on the basis of an Analytic Bremsstrahlung Calculation (ANB), an example of which was illustrated in Fig. 4.4.1. This

produces reference tables of absolute polarisation with respect to incident photon which can then be used to scale each event, and thus the amplitude of the $\cos(2\phi)$ distribution, to produce an accurate determination of Σ.

For each polarisation setting, a so-called 'enhancement spectrum' is produced, showing the peak due to the alignment of the electron beam with the relevant plane of the diamond crystal mounted in the goniometer. An example of an enhancement spectrum is displayed in Figure 5.4.4.1, which is then used to normalise the $\cos(2\phi)$ distributions produced by the processing of the polarised experimental data.

In order to do the normalisation, we first set a 'baseline' on the Y-axis of the enhancement spectrum having first subtracted the incoherent Bremsstrahlung background. This allows us to remove by direct subtraction what could be referred to as the DC offset from the spectrum. This baseline is set at a value determined by inspection of the plot; 100 on the example shown (the upper plot in Fig. 5.4.4.1). Once this baseline value had been subtracted from the enhancement spectrum, what remains is scaled to the maximum value of the ANB fit to the coherent edge. This ensures that the degree of linear polarisation is included as a scaling factor rather than an absolute value.

We then take a look at edges from the ANB calculation and find one that fits the edge in the data best. To accommodate smearing in the polarisation edges, a superposition of two such ANB edges may be required; the bottom plot of shows an example of this scenario. From this fit to the data the polarisation for any particular incident photon can be accessed by cross referenceing a plot such as that shown in Fig. 5.4.4.1 (bottom).

5.4.5 Scaling the $\cos 2\phi$ Distributions

In order that a meaningful asymmetry can be constructed, both of the polarisation data sets are scaled to the magnitude of the other before calculating the asymmetry. This is done by multiplying the cross-section for one orientation by the number of events and degree of linear polarisation associated with the other polarisation orientation $N_{\perp}P_{\perp}\sigma_{\parallel}$ and $N_{\parallel}P_{\parallel}\sigma_{\perp}$. Appendix E contains a full discussion of this process. The asymmetry is constructed , thus producing plots from which Σ can be directly extracted from the relation outlined in eqn. 5.14. These are the plots and results tables presented in 6.

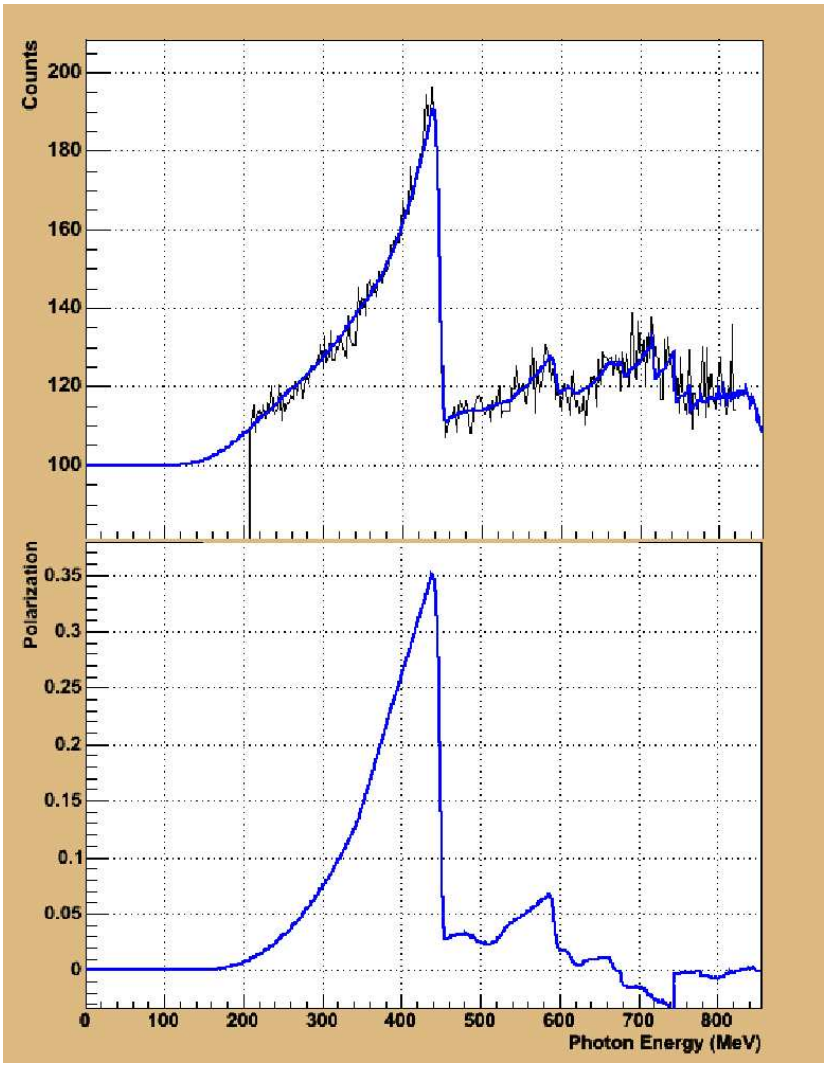

Figure 5.22: Determining the degree of polarisation of the linearly polarised photon beam. This is shown for the 440 MeV data, the 400 MeV data received exactly the same treatment. The spectra show:

Top: Enhancement spectrum from the Tagger TDCs fitted with a coherent edge calculated using ANB methods. The exponential incoherent Bremsstrahlung background has been subtracted.

Bottom: Baseline-subtracted spectrum of P *vs.* E_γ scaled by an edge as calculated by the ANB calculation (blue).

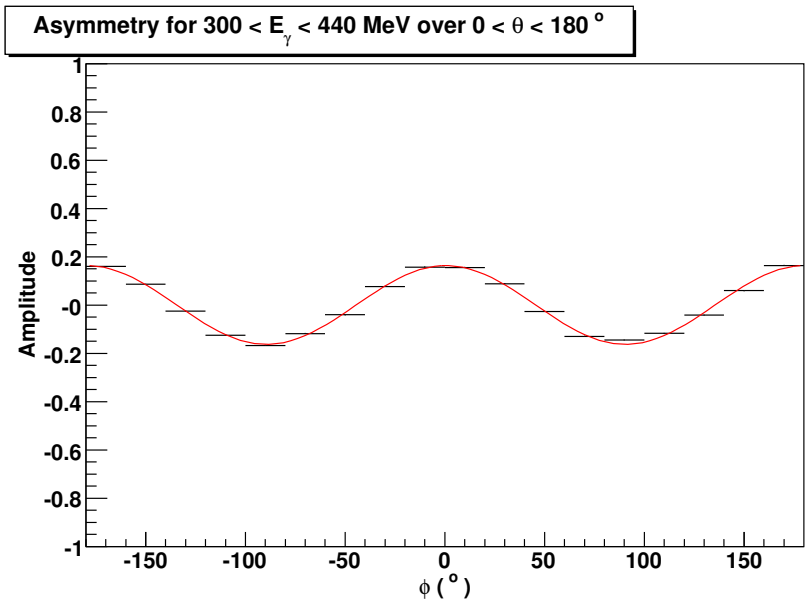

Figure 5.23: A plot showing a typical $\cos 2\phi$ fit (red) to an experimental asymmetry distribution (black). The case shown is for the 440 MeV data set. The y-axis range of -1 to 1 shows the limits of such a distribution.

5.5 Determining Σ

Once the asymmetries have been constructed from the angular distributions associated with the two orthogonal polarisation data subsets, the asymmetries are fitted in order to extract Σ, the quantity we desire to experimentally determine.

5.5.1 Fitting the asymmetries

The constructed asymmetry can be fitted with a function of the form

$$O + A\cos(2\phi - \phi_0) \tag{5.15}$$

where O is the offset observed, A is the amplitude of the $\cos(2\phi)$ distribution and ϕ_0 is the initial phase. O should be 0, implying that the detector acceptance is equal for both polarisation orientations. A is related to Σ, the experimental quantity of interest and it's extraction is discussed presently. An example of a $\cos(2\phi)$-fitted asymmetry distribution is shown in Fig. 5.23.

5.5.2 Determining ϕ_0

The value of ϕ_0, the initial phase of the distribution, must be established. This was done using data from the alternative reaction channel, $\overrightarrow{\gamma}p \rightarrow p\pi^0$ due to the higher statistics available, the data for this being accumulated at the same time as the $\overrightarrow{\gamma}p \rightarrow n\pi^+$. The photon asymmetry for the $p\pi^0$ channel was constructed and the initial phase of the fit extracted as a parameter, from eight incident photon energies. This was done for each of the two possible electron polarisations - the experiment was run with both circularly polarised photons as well as linear, the former being produced by polarised electrons incident of a crystalline radiator - producing 16 values from which ϕ_0 was determined. The value of ϕ_0 was calculated by combining the values for phase given in [67], table 5.2, weighted by their errors as in eqn. (5.16), below:

$$\phi_0 = \frac{\sum(\phi_{0measured} \times w)}{\sum(w)} \tag{5.16}$$

with $w = \left(\frac{1}{\delta\phi_{0measured}}\right)$. This yields a value of $\phi_0 = -0.564176$ which was subsequently used in the fit given in eqn. (5.15).

5.5.3 Extracting Σ

The Photon Asymmetry, Σ, is related to the amplitude of the $\cos(2\phi)$ distribution, A, by the relation

$$\Sigma = \frac{A}{\left(\frac{2P_\perp P_\parallel}{P_\perp + P_\parallel}\right)} \tag{5.17}$$

The factor $\left(\frac{2P_\perp P_\parallel}{P_\perp + P_\parallel}\right)$ in eqn. (5.17) comes from the way that the cross-section for linearly polarised photons relates to the unpolarised cross-section. This is discussed in Appendix E. Values of Σ obtained in this way for the various angular and incident E_γ ranges can be found in section (6.1). If $P_\perp = P_\parallel$, as was the case in the performed experiment, eqn. (5.17) reduces to

$$\Sigma = \frac{A}{P} \tag{5.18}$$

5.5.3.1 Uncertainties in Σ

The uncertainty in Σ, $\delta\Sigma$, is determined from the uncertainties in A and P (hereon referred to as δA and δP respectively). For these purposes, the uncertainties in the degrees of linear polarisation for each of the orientations are deemed to be equal and thus treated as one entity. δA is obtained from the $\cos(2\phi)$ fit whilst δP is estimated to be around 5% (Section 7.2 of [68] and Appendix D of [67]).

Including the uncertainties in the dependent quantities, eqn. 5.17 becomes

$$\Sigma \pm \delta\Sigma = \frac{A \pm \delta A}{P \pm \delta P} \tag{5.19}$$

$\delta\Sigma$ is evaluated using the partial derivatives method, in this case

$$(\delta\Sigma)^2 = \left(\frac{\partial\Sigma}{\partial A}\right)^2 (\delta A)^2 + \left(\frac{\partial\Sigma}{\partial P}\right)^2 (\delta P)^2 \tag{5.20}$$

and thus

$$(\delta\Sigma)^2 = \left(\frac{1}{P}\right)^2 (\delta A)^2 + \left(\frac{-A}{P^2}\right)^2 (\delta P)^2 \tag{5.21}$$

Using this method, the uncertainties in Σ for the full ranges of analysed data were found to be $\delta\Sigma \sim 5.66\%$ for the 400 MeV data and $\delta\Sigma \sim 5.08\%$ for the 440 MeV data. Of these uncertainties, the statistical contribution arising from the fit is 2.64% and 0.94% for the two data sets respectively. The uncertainty in calculating the degree of linear polarisation using the ANB calculation accounts for the remaining discrepancy.

The binned data is also subjected to this treatment. The results are presented graphically with only the statistical errors taken from the uncertainty in the fit shown. This is to be consistent with the results from previous experiments which have only this uncertainty shown. The uncertainties in Σ due to the uncertainty in calculating the degree of linear polarisation are given in the results tables of Appendix F.

5.5.4 Systematic Effects

From the standard expression for calculating an asymmetry (eqn. (1.1)) it can be seen that by the nature of evaluation that the systematic effects will cancel. Systematic effects are generally absolute

quantities such as angular acceptance, yield and tagging efficiency. As these quantities are more commonly associated with the determinations of total cross-sections and have no effect on asymmetry calculations they are not discussed here.

5.6 Monte-Carlo Simulation

The results obtained (Chapter 6) from following the above analysis procedure were compared with some simulated data for consistency. The conclusions drawn from doing this are also presented in 6.

5.6.1 GEANT-4

The simulated A2 detector setup was written in GEANT-4 [69] which, like AcquRoot, is a C++ based piece of software. This has the obvious advantage over the Fortran-based GEANT-3 of having somewhat better compatibility with all of the various functions available in the myriad ROOT classes.

In short, the primary function of GEANT is to "simulate the passage of particles through matter". In doing this it also tracks particles and their interactions with said matter through user-defined detector geometries.

5.6.2 AcquMC

AcquMC - see section 8 of [49] - is the simulation arm of the AcquRoot Software. It produces AcquRoot- and thus ROOT- compatible sample data files by way of its kinematics generator. There are specific input files for each of the various reactions possible with the set-up at MAMI and one simply uses the one they wish to study. The AcquMC class 'TMCGenerator' does the spade-work, utilising the ROOT class 'TFoam' to perform the multi-dimensional random sampling required for populating all of phase space with reaction products, using distributions produced by physics models. This can include polarisation information if desired and this makes the comparison with experimental results possible as AcquMC can also be used to compare SAID partial-wave analyses with experimental data.

SAID (Section 1.3.2) is used to model the photo-pion differential cross sections and Sigma asymmetries. These are tabulated on a grid of energy and angular points. These data are used to generate, using AcquMC, a random sample of events (which conform to the SAID distributions). Each "event" records the four-momenta of the incident photon, the final-state pion and the recoil nucleon. Events are then run through the GEANT-4 based computer model of the A2 detector apparatus setup. This simulates the response of the Crystal Ball and TAPS detectors to the sample of events created by the SAID generator incorporated in AcquMC. The output from the A2 detector geometry is recorded, then analysed using AcquRoot in an almost identical way to that employed for real data. The sigma values extracted from the AcquRoot analysis of the simulation can then be compared with the experimental data thus providing useful checks of the accuracy of the simulation.

Chapter 6

Results and Discussions

6.1 Experimental Results

The experimental results are presented here. When discussing them, it should be noted that the phrase 'full energy range' is often used. This is the range of incident photon energies, E_γ, analysed for that data set, each of which used an E_γ range of 100 MeV. These ranges were 300$\leq E_\gamma \leq$400 MeV for the 400MeV data set and 340$\leq E_\gamma \leq$440 MeV for the 440 MeV data set. In the titles of the relevant graphs, these are expressed as 350$\pm$50 MeV and 390$\pm$50 MeV respectively. The phrase 'energy bin' refers to a 20 MeV subset of these 'full energy ranges'. The similar phrase 'full θ range' refers to 30$\leq \theta_{\pi^+}^{CM} \leq$160 degrees in the CM frame. A 'θ bin' is equal to a subset of this full θ range, these being 30 to 60 degrees, 60 to 80 degrees, 80 to 100 degrees, 100 to 120 degrees and 120 to 170 degrees.

6.1.1 The 400 MeV data

Figures 6.1 through to 6.7 show the results from the 400MeV data set. Figure 6.1 shows the data split into the five described theta bins over the full energy range for this data set. Figures 6.2 to 6.6 show the fits to the asymmetry distributions for the data split into θ and E_γ bins while 6.7 shows the values for Σ extracted from the $\cos(2\phi)$ fits. The asymmetries and $\cos(2\phi)$ fits are all presented on the y-axis range of -1 $\leq y \leq$ 1 to enable the evolution with respect to $\theta_{\pi^+}^{CM}$ and E_γ to be easily observed.

These values of Σ are presented on plots of Σ *vs.* $\theta_{\pi^+}^{CM}$ enabling the variance of Σ with respect to $\theta_{\pi^+}^{CM}$ to be easily observed. The value of Σ was extracted from the amplitude of the $\cos(2\phi)$ fits made to each asymmetry distribution as described in Section 5.5.3.

The fits displayed on the plots of Σ *vs.* $\theta_{\pi^+}^{CM}$ are the predictions of the current versions of MAID (red line) and SAID (blue line). The agreement (or otherwise) of the experimental data with these fits is discussed below, in Section 6.1.3.

6.1.2 The 440 MeV Data

Figures 6.8 through to 6.14 show the results from the 440MeV data set. The plots presented are equivalent to the ones described above for the 400 MeV data and are arranged in the same way.

6.1.3 Comparisons with MAID and SAID

Predicted values of Σ from MAID and SAID are compared with those from the data for the two coherent peak energies as can be seen by the red and blue fit lines on the graphs shown in Figs 6.7 and 6.14. These seem to disagree somewhat with the experimental results, especially when considering the data after its subdivision by E_γ. A reason for this can be found when perusing the $\cos(2\phi)$ fits to the asymmetry distributions (Figs. 6.2 to 6.6 and 6.9 to 6.13). From these plots, it can be seen that the fits sometimes seem to not fit the data very well thus leading to an ambiguous value for the amplitude A. This is less of a problem in the more populated regions where the effects of the uncertainty in knowing the degree of linear polarisation dominate, but is significant at the extremes of the ranges of investigation; $30^\circ < \theta_{\pi^+}^{CM} < 56^\circ$ and especially $134^\circ < \theta_{\pi^+}^{CM} < 160^\circ$. Extracting the precise degree of linear polarisation P was also problematic, not least because there were some Tagger channels in the data ranges of interest exhibiting a reduced count rate than expected due to age-related radiation damage. The ANB fit used to return values of P therefore over-compensated at these photon energies, which in turn has knock-on effects when scaling A by this value of P in order to return a result for Σ as in eqn. (5.18).

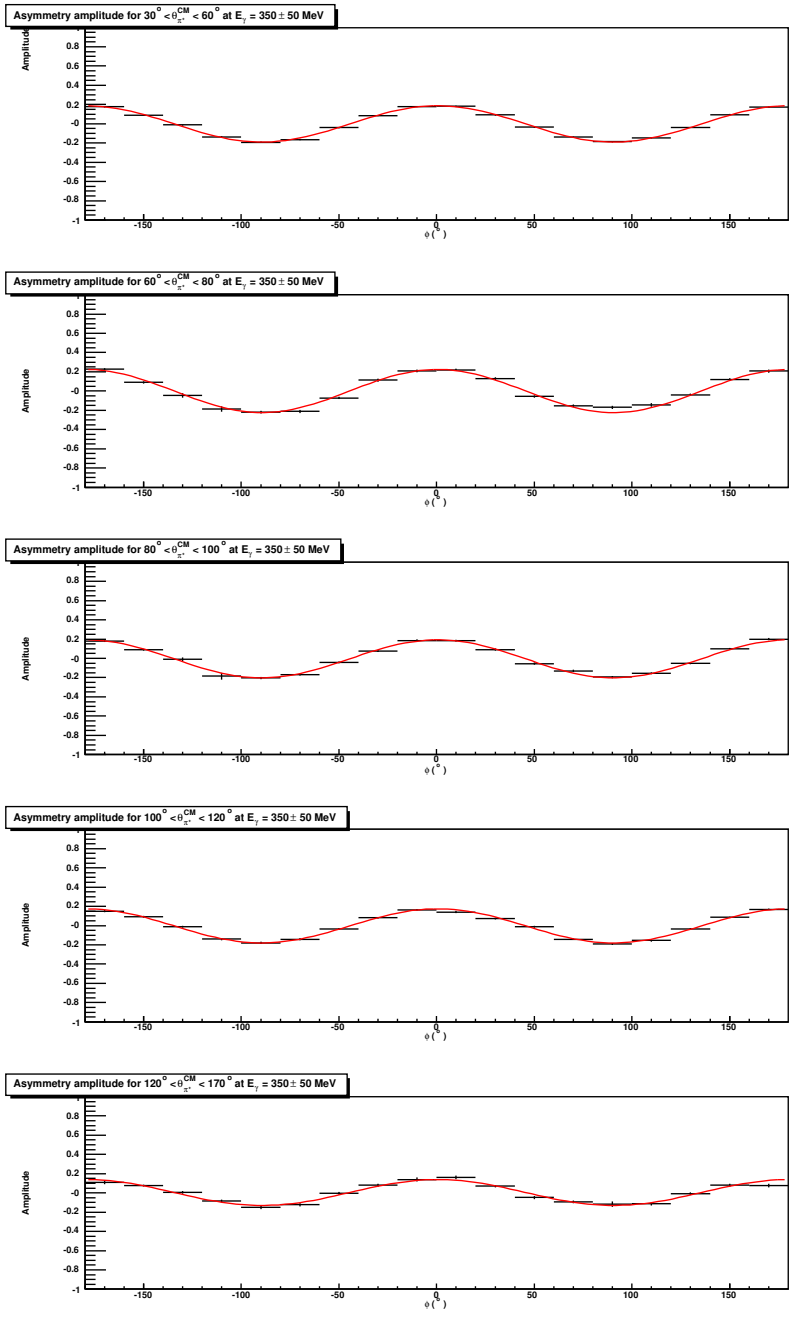

Figure 6.1: Asymmetry distributions over the full E_γ range from the 400MeV data. The data has been split into five $\theta^{CM}_{\pi^+}$ bins as described in the main body of text.

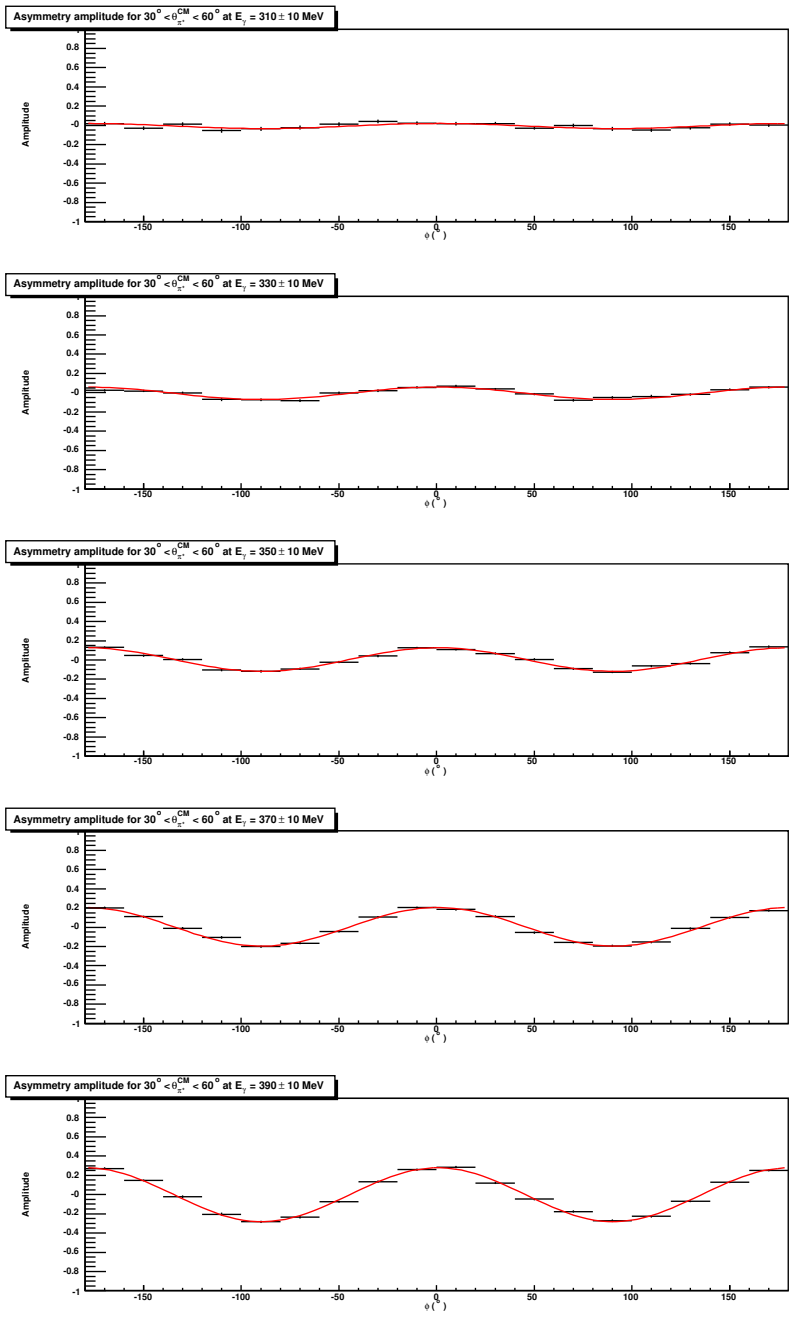

Figure 6.2: Asymmetry distributions over the $30° < \theta_{\pi^+}^{CM} < 60°$ angular range from the 400MeV data set. The data has been split into five E_γ bins as described in the main body of text and is displayed vertically in terms of increasing E_γ, from top to bottom.

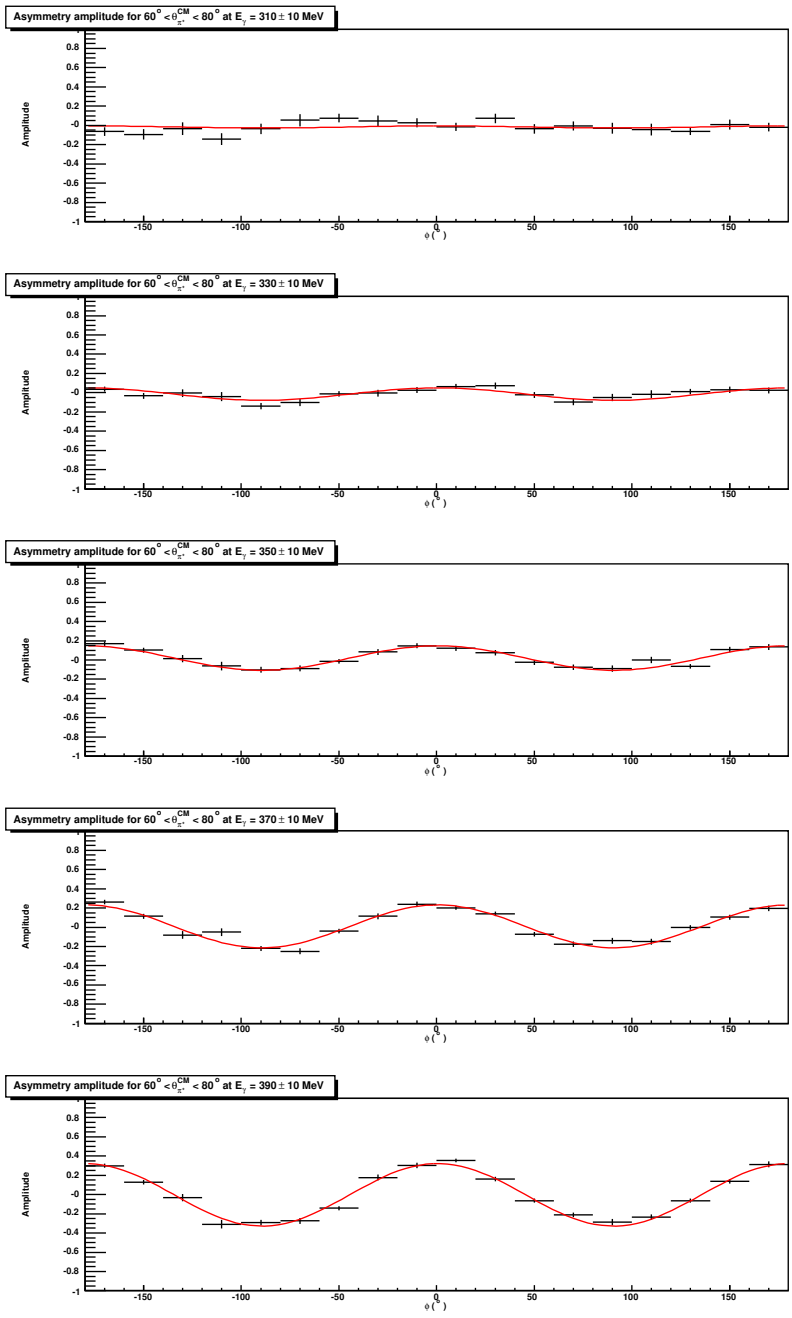

Figure 6.3: Asymmetry distributions over the $60° < \theta_{\pi^+}^{CM} < 80°$ angular range from the 400MeV data set. The data has been split into five E_γ bins as described in the main body of text and is displayed vertically in terms of increasing E_γ, from top to bottom.

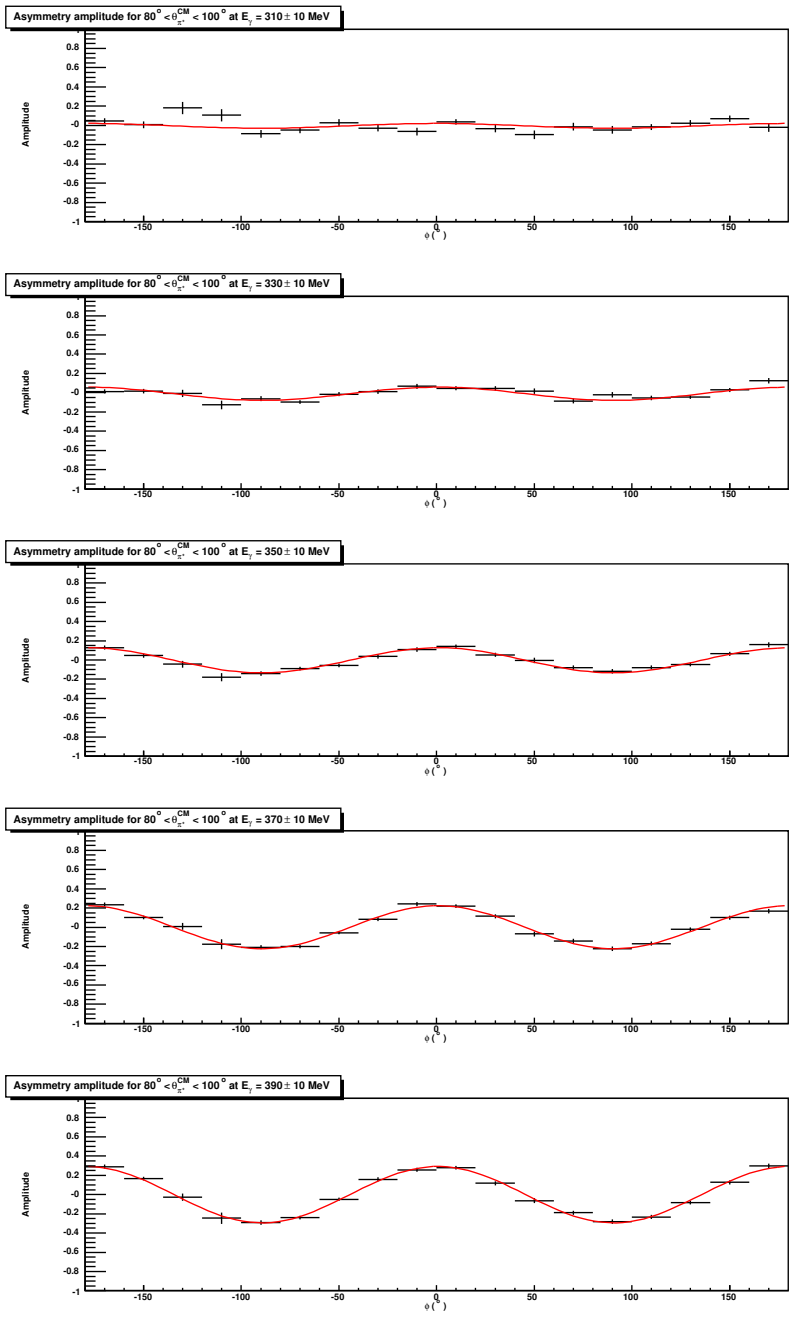

Figure 6.4: Asymmetry distributions over the $80° < \theta_{\pi^+}^{CM} < 100°$ angular range from the 400MeV data set. The data has been split into five E_γ bins as described in the main body of text and is displayed vertically in terms of increasing E_γ, from top to bottom.

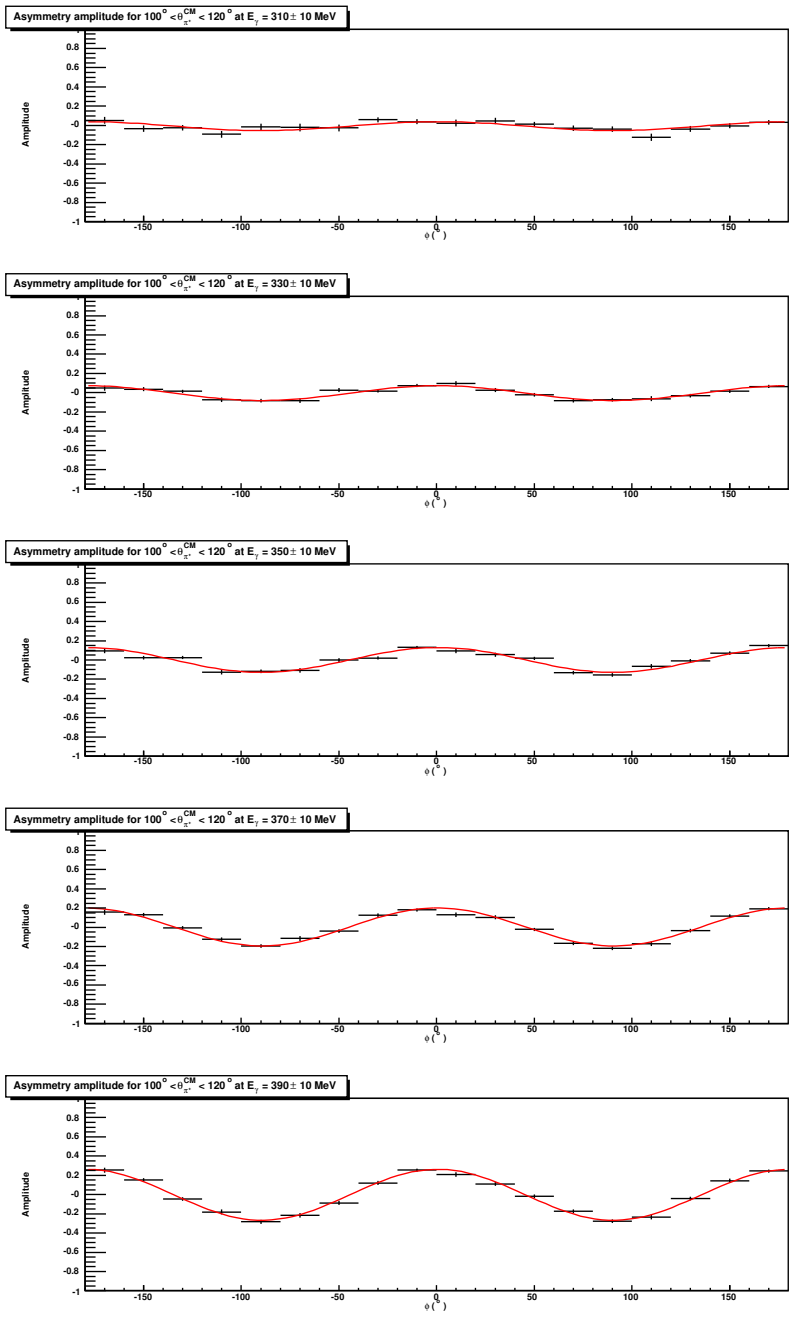

Figure 6.5: Asymmetry distributions over the $100° < \theta_{\pi^+}^{CM} < 120°$ angular range from the 400MeV data set. The data has been split into five E_γ bins as described in the main body of text and is displayed vertically in terms of increasing E_γ, from top to bottom.

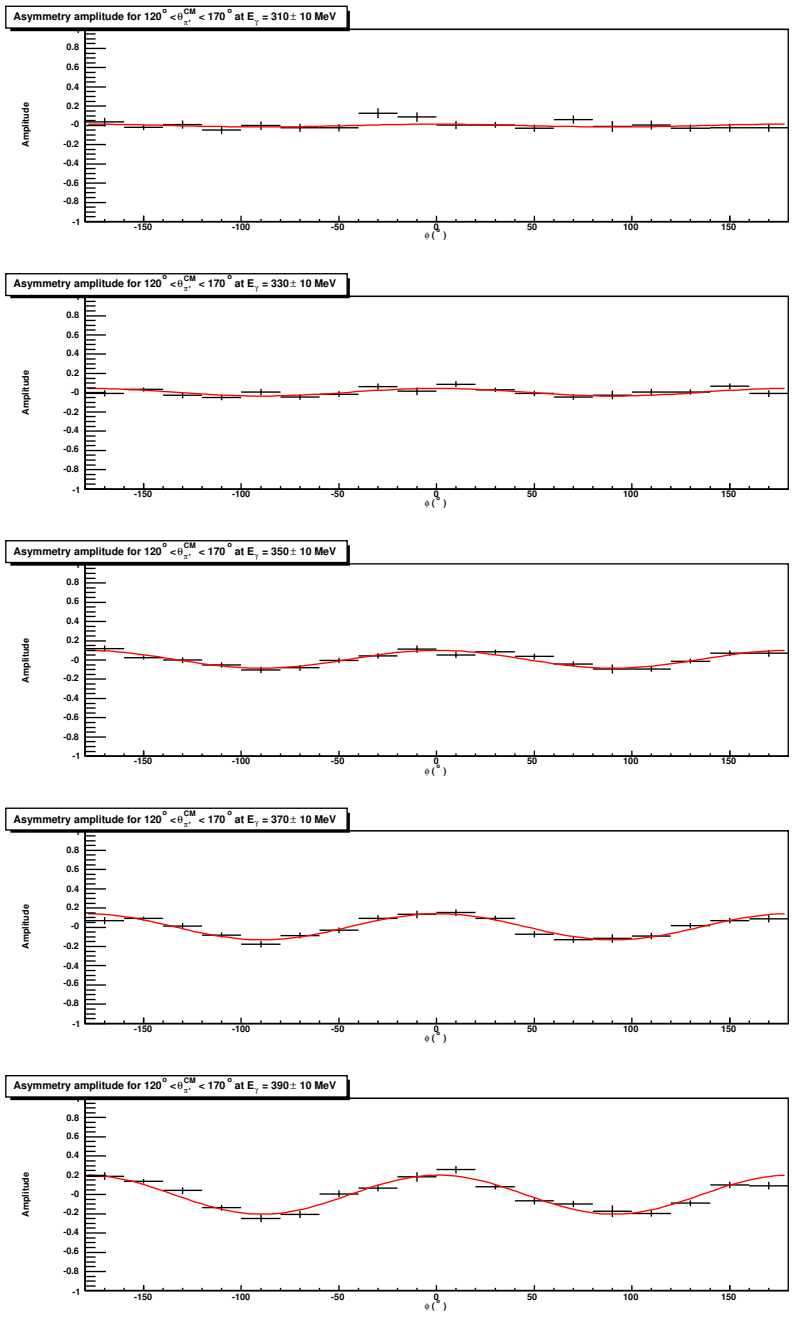

Figure 6.6: Asymmetry distributions over the $120° < \theta_{\pi^+}^{CM} < 170°$ angular range from the 400MeV data set. The data has been split into five E_γ bins as described in the main body of text and is displayed vertically in terms of increasing E_γ, from top to bottom.

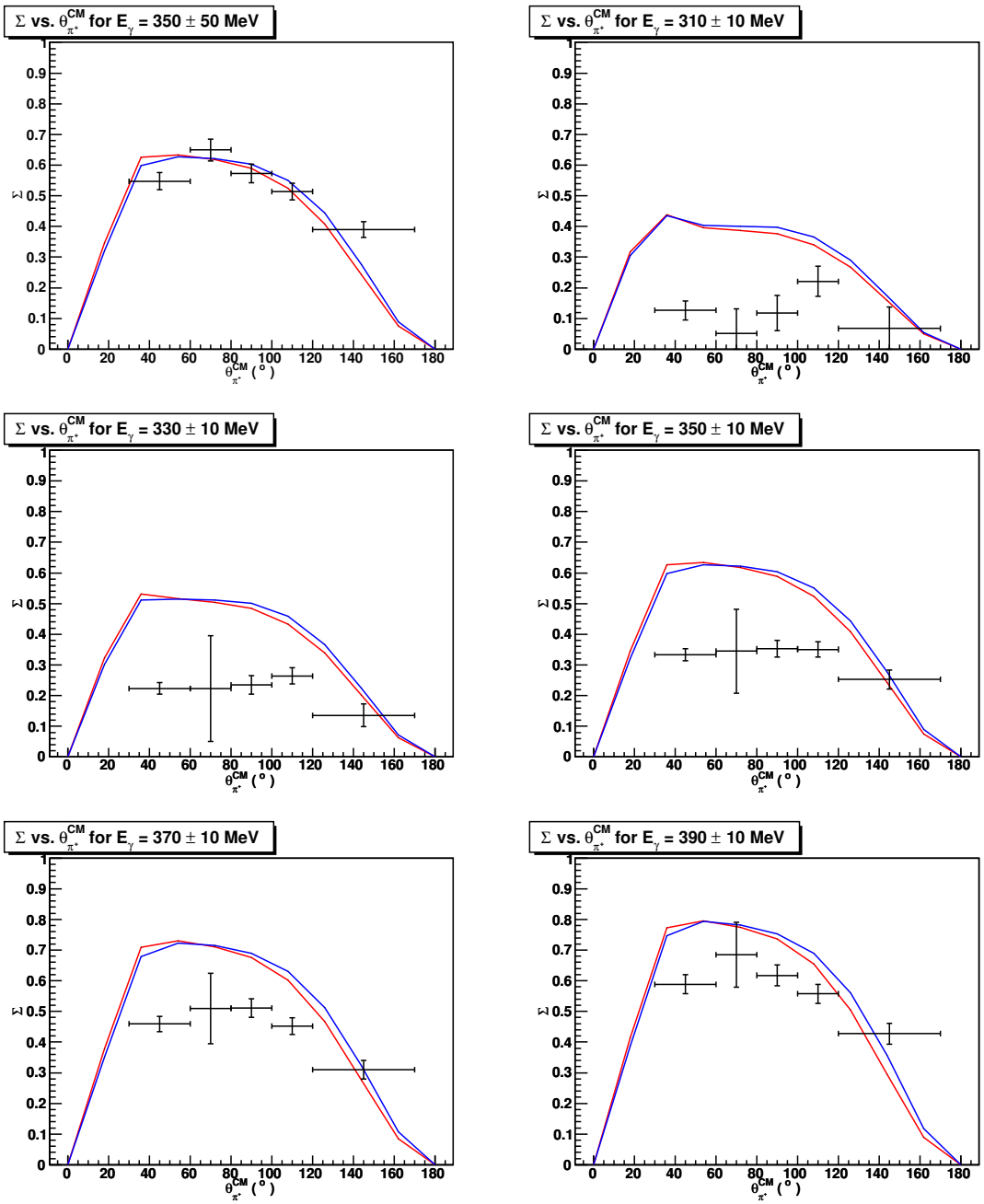

Figure 6.7: Photon asymmetries for the 400 MeV data set, displayed as a function of $\theta_{\pi^+}^{CM}$ for the full E_γ range (top left) as well as the 20 MeV E_γ bins (others). E_γ ranges are given in the titles of the plot in question. The displayed uncertainties in *Sigma* include the contributions from both A and P.

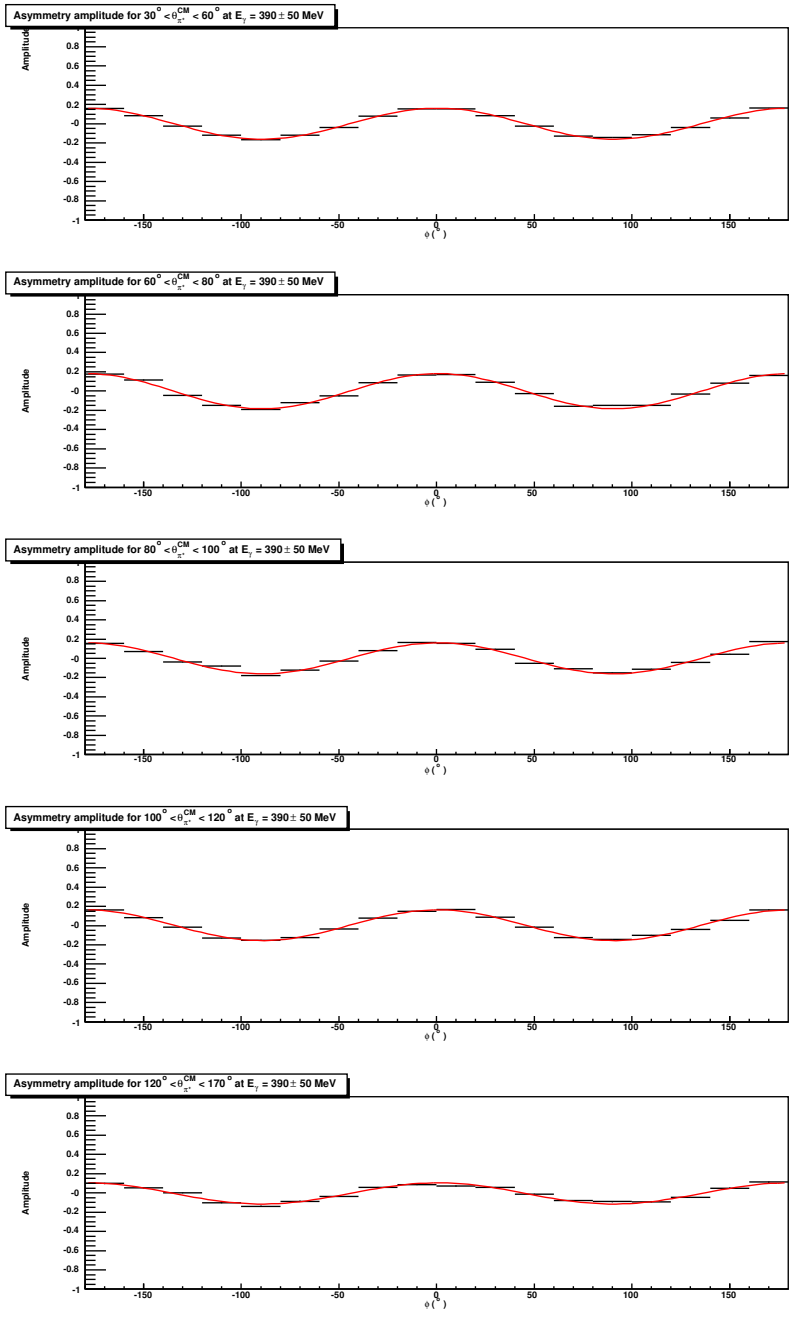

Figure 6.8: Asymmetry distributions over the full E_γ range from the 440MeV data. The data has been split into five $\theta^{CM}_{\pi^+}$ bins as described in the main body of text.

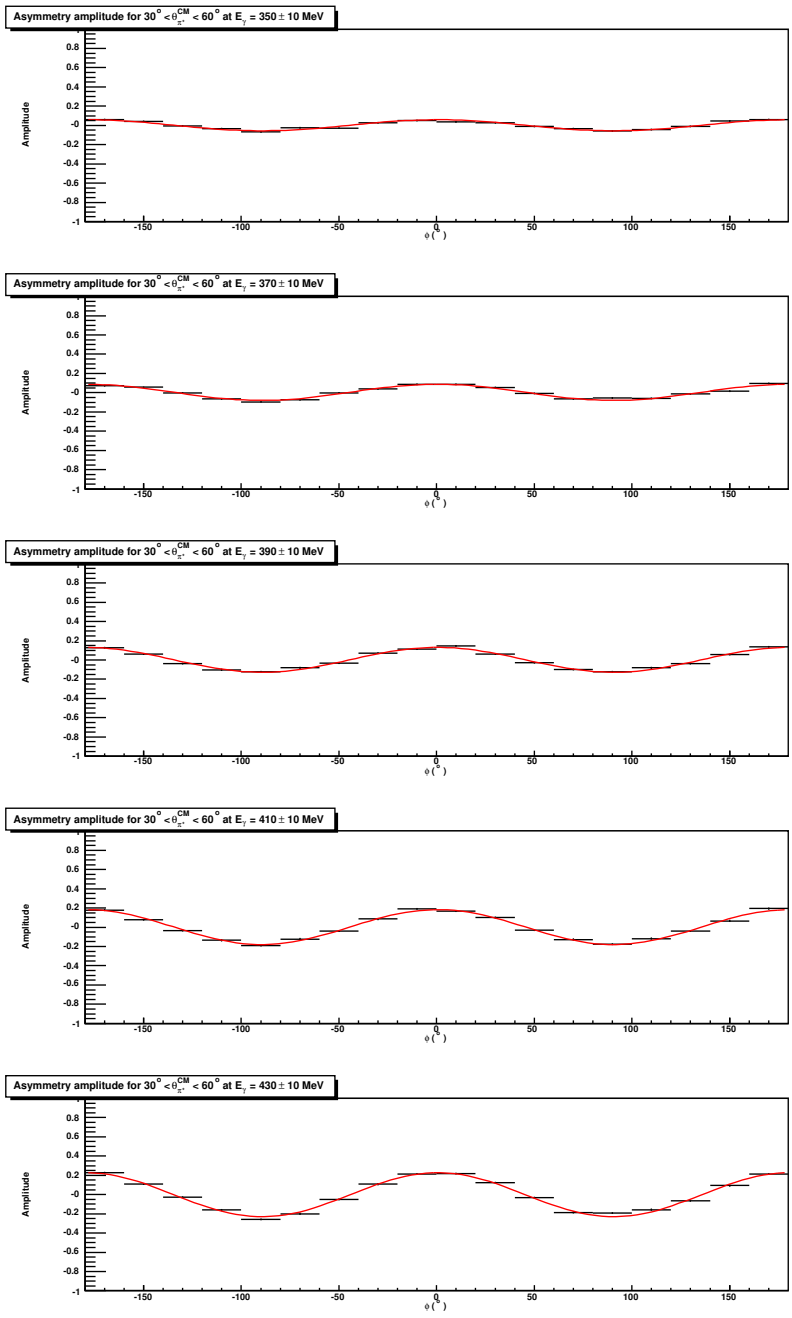

Figure 6.9: Asymmetry distributions over the $30° < \theta_{\pi^+}^{CM} < 60°$ angular range from the 440MeV data set. The data has been split into five E_γ bins as described in the main body of text and is displayed vertically in terms of increasing E_γ, from top to bottom.

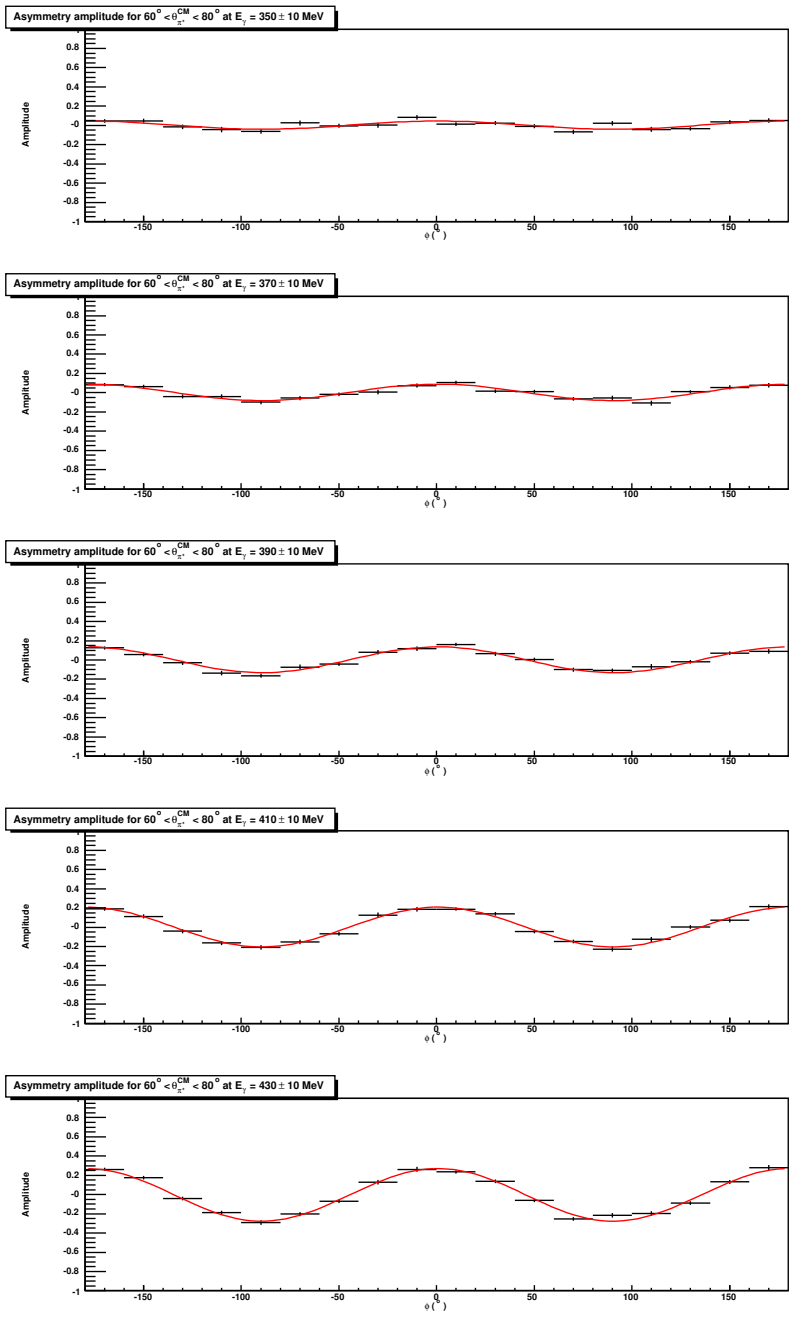

Figure 6.10: Asymmetry distributions over the $60° < \theta_{\pi^+}^{CM} < 80°$ angular range from the 440MeV data set. The data has been split into five E_γ bins as described in the main body of text and is displayed vertically in terms of increasing E_γ, from top to bottom.

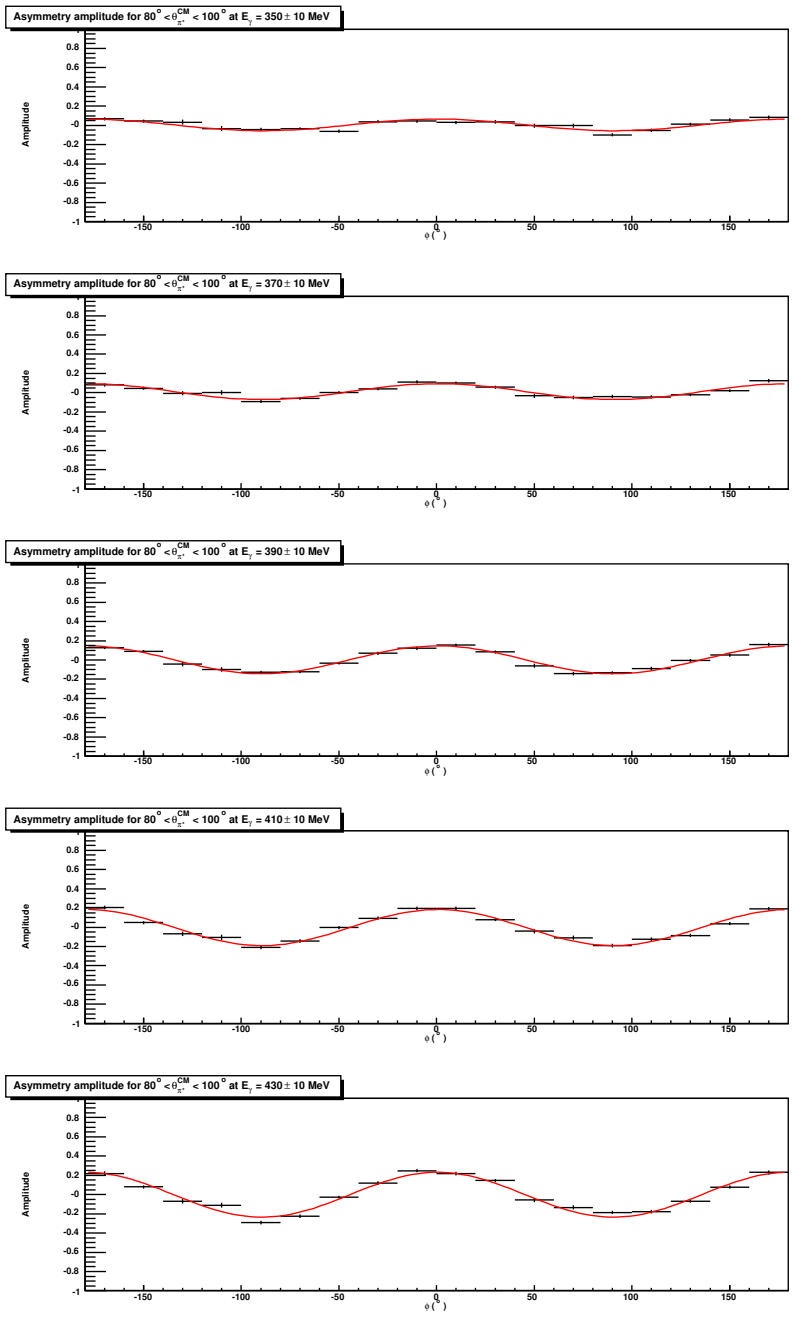

Figure 6.11: Asymmetry distributions over the $80° < \theta_{\pi^+}^{CM} < 100°$ angular range from the 440MeV data set. The data has been split into five E_γ bins as described in the main body of text and is displayed vertically in terms of increasing E_γ, from top to bottom.

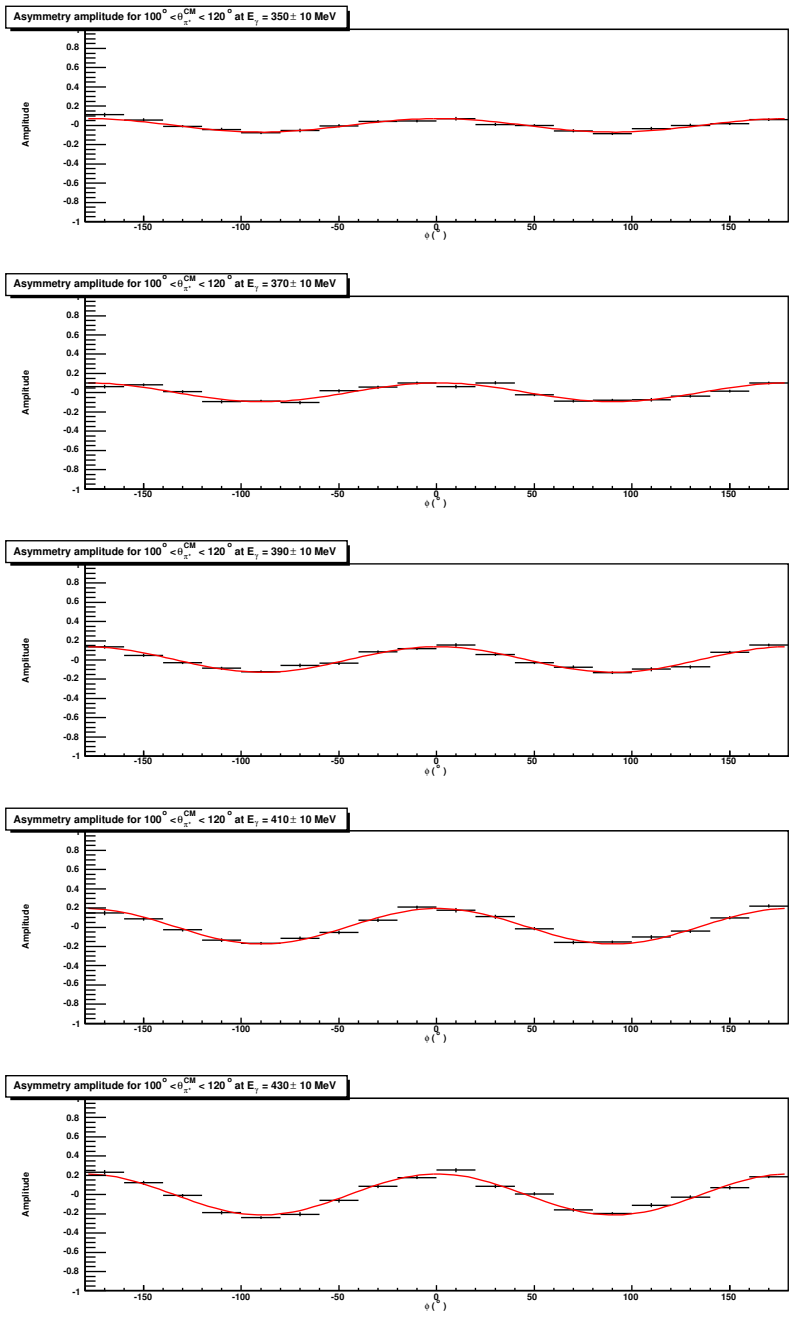

Figure 6.12: Asymmetry distributions over the $100° < \theta_{\pi^+}^{CM} < 120°$ angular range from the 440MeV data set. The data has been split into five E_γ bins as described in the main body of text and is displayed vertically in terms of increasing E_γ, from top to bottom.

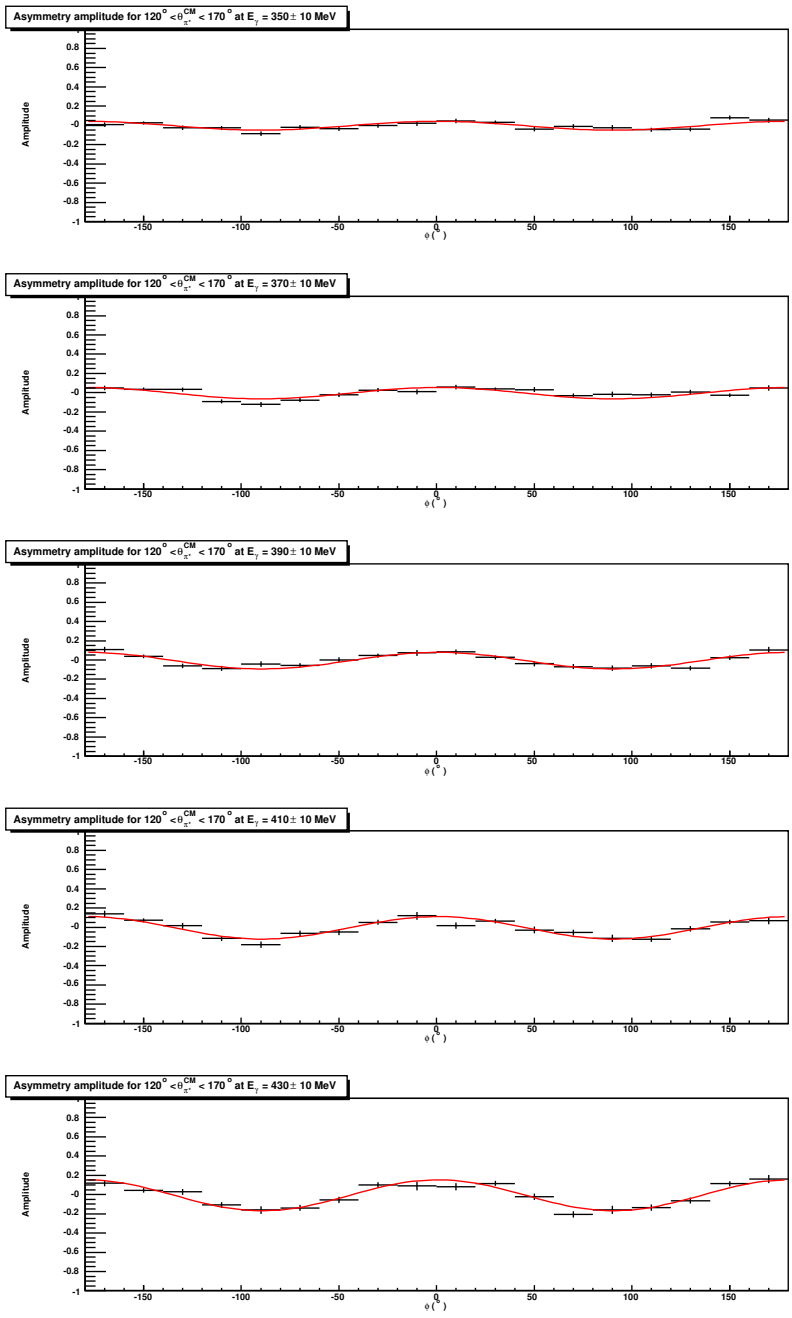

Figure 6.13: Asymmetry distributions over the $120° < \theta_{\pi^+}^{CM} < 170°$ angular range from the 440MeV data set. The data has been split into five E_γ bins as described in the main body of text and is displayed vertically in terms of increasing E_γ, from top to bottom.

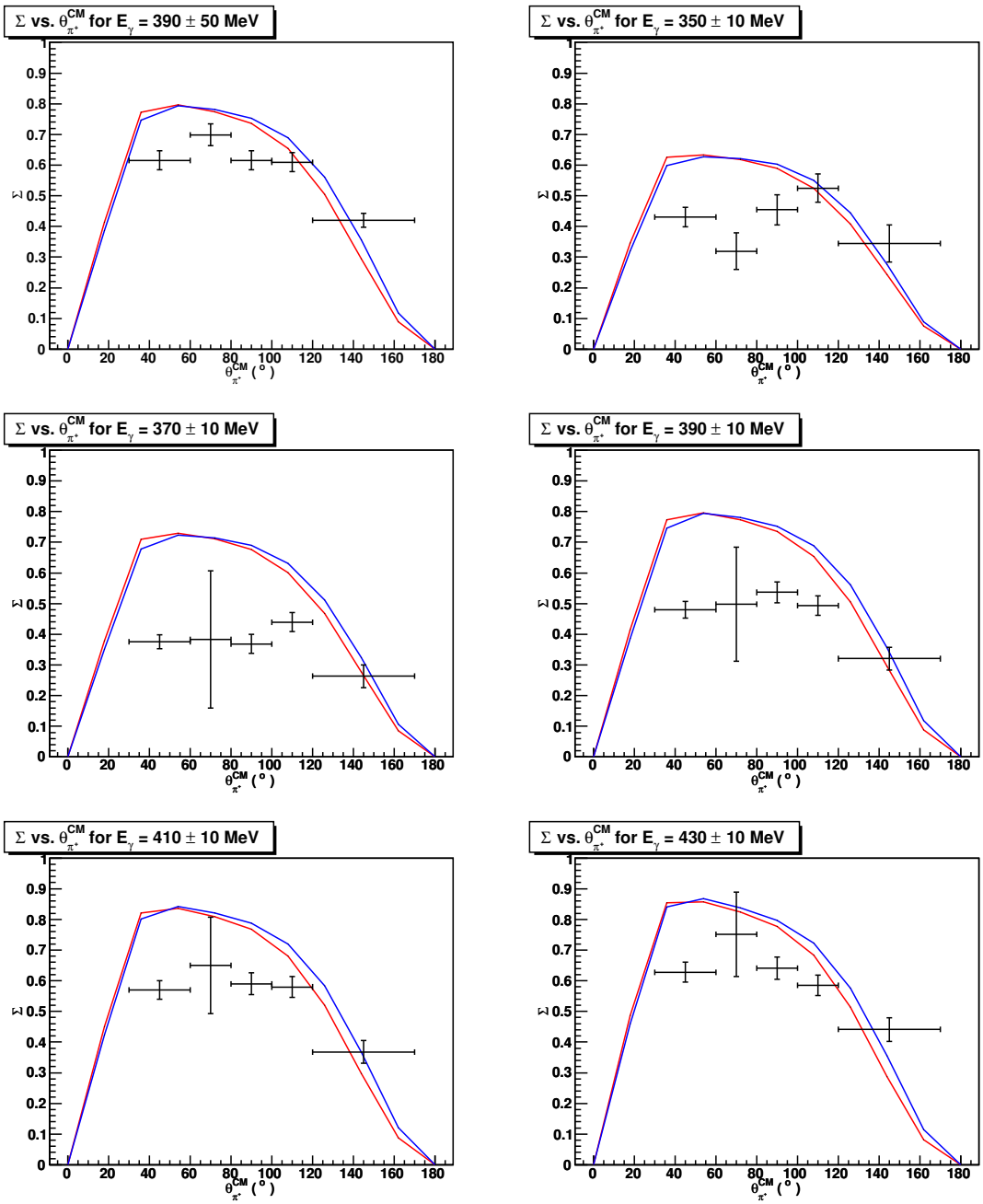

Figure 6.14: Photon asymmetries for the 440 MeV data set, displayed as a function of $\theta_{\pi^+}^{CM}$ for the full E_γ range (top left) as well as the 20 MeV E_γ bins (others). E_γ ranges are given in the titles of the plot in question. The displayed uncertainties in $Sigma$ include the contributions from both A and P.

6.2 Internal Data Consistency

As the E_γ ranges for the two data sets partially overlap, it makes sense to compare these results for consistency. The data ranges that overlap are the 350 $\pm$ 10 MeV, 370 $\pm$ 10 MeV and 390 $\pm$ 10 MeV E_γ bins, the $\theta_{\pi^+}^{CM}$ binning being kept constant at a width of 26° between 30° and 160°. The values of Σ for each data set are presented in Fig. 6.15 in order that they may be easily cross-referenced with each other. The numerical values of Σ for these plots are tabulated in Appendix F.

It can be seen from Table F that the data does, for the most part, agree between the two data sets in terms of shape of the $\theta_{\pi^+}^{CM}$ distributions and approximate magnitude of Σ. This is to be expected as despite coming from data sets with different coherent photon polarisation edges, the normalisation process for each data set is identical. A possible cause of the disagreement is contained in the determination of the degree of linear polarisation for each data set which was determined from different ANB calculations as the data was collected during experimental runs with the polarisation enhancement set at different photon energies. These degrees of linear polarisation are shown in Fig. 6.16. The difference in the degree of linear polarisation will give rise to a difference in Σ. It is this difference that is observed in Fig. 6.15.

6.3 Comparisons with Previous Data

Values of Σ for previous experiments are compared with those from the data for the two coherent peak energies - Fig. 6.3. The seem to agree reasonably with the results from previous experiments. The 400 MeV data (red circles) seems to fare less well statistically than the 440 MeV data (blue circles) when compared to the previous work. The reason for this is that there were 10 times the amount of data in the 440 MeV data set and thus the statistics scale accordingly in the results. The disagreement in the values of Σ therefore has to be explainable by the poorer $\cos(2\phi)$ fits to the asymmetry distributions as well as the ANB fit to the enhanced E_γ spectra for both data sets.

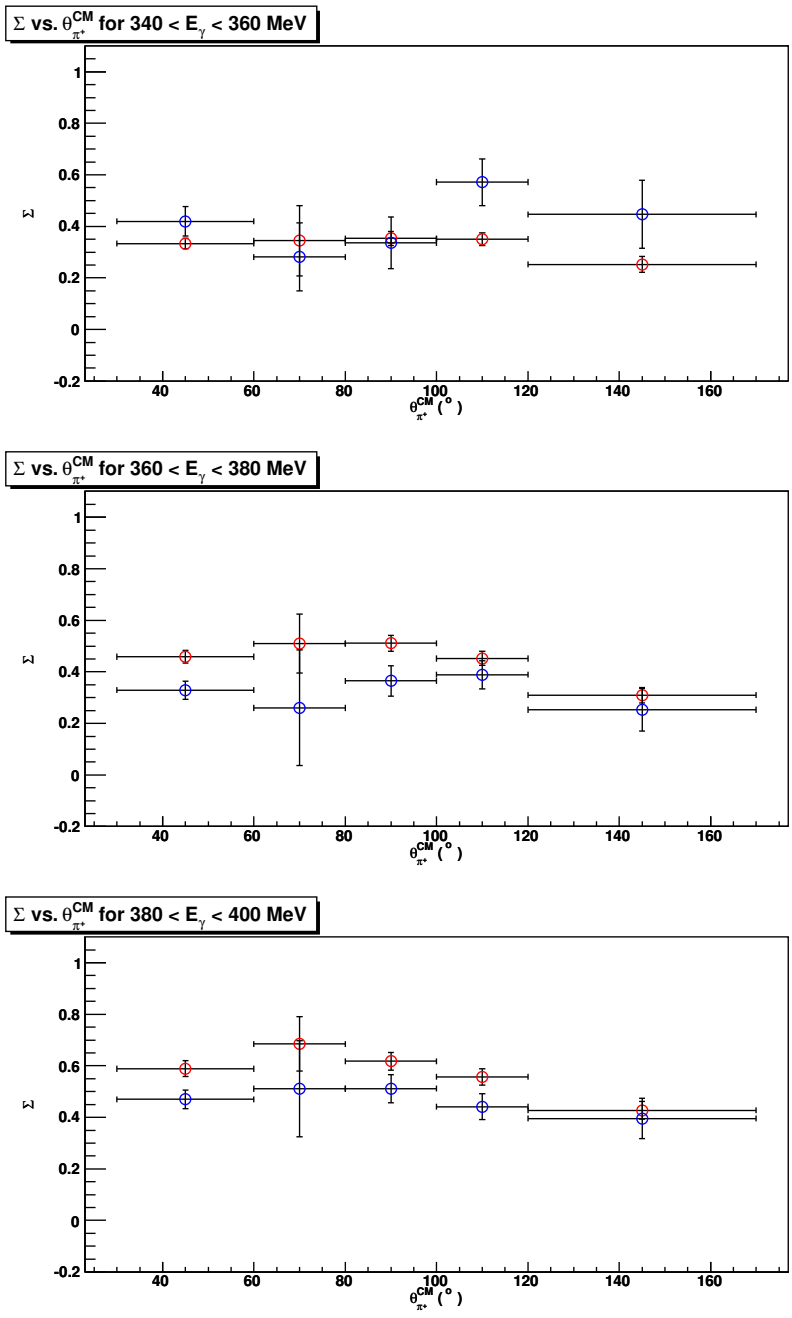

Figure 6.15: Comparisons of values of Σ obtained from the analysis of the two experimental data sets for the overlapping ranges of E_γ. The 400 MeV data is shown in red, the 440 MeV data in blue.

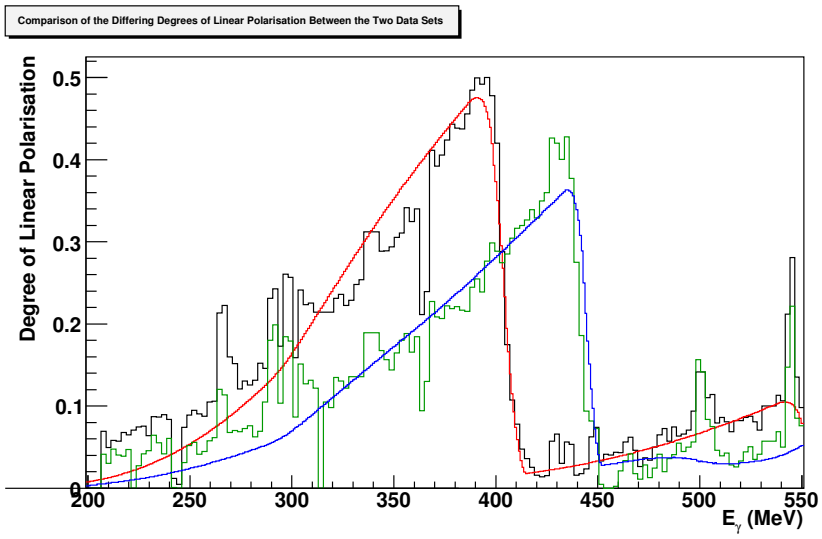

Figure 6.16: Comparisons of the differing degrees of linear polarisation between the two data sets. The 400 MeV data is shown in black with the fit in red. The 440 MeV data is shown in green with the fit in blue.

6.4 Comparisons with Simulation

As mentioned in Section 5.6.2, SAID [7] allows simulated polarisation data to be produced. This simulated data was analysed in the same way as the experimental data and the results are compared in Figs. 6.18 and 6.19. On this plot, the displayed uncertainties are from the contribution of δP only. The reason for this is that comparing the statistical uncertainties of two unequal samples is somewhat meaningless, hence its omission. The large discrepancies between the simulated data and the experimental results stemmed from the fact that only 400,000 events were simulated for each data set (200,000 for each polarisation orientation). This is especially evident for the 440 MeV data. The experimental data sets were several orders of magnitude larger than this and so the comparisons between then should be made with the idea in mind that the simulation of polarised data is very much in its infancy with respect to the A2 GEANT-4 simulation. It is included here to illustrate its potential usefulness in the future when both the SAID models and analysis techniques are more evolved.

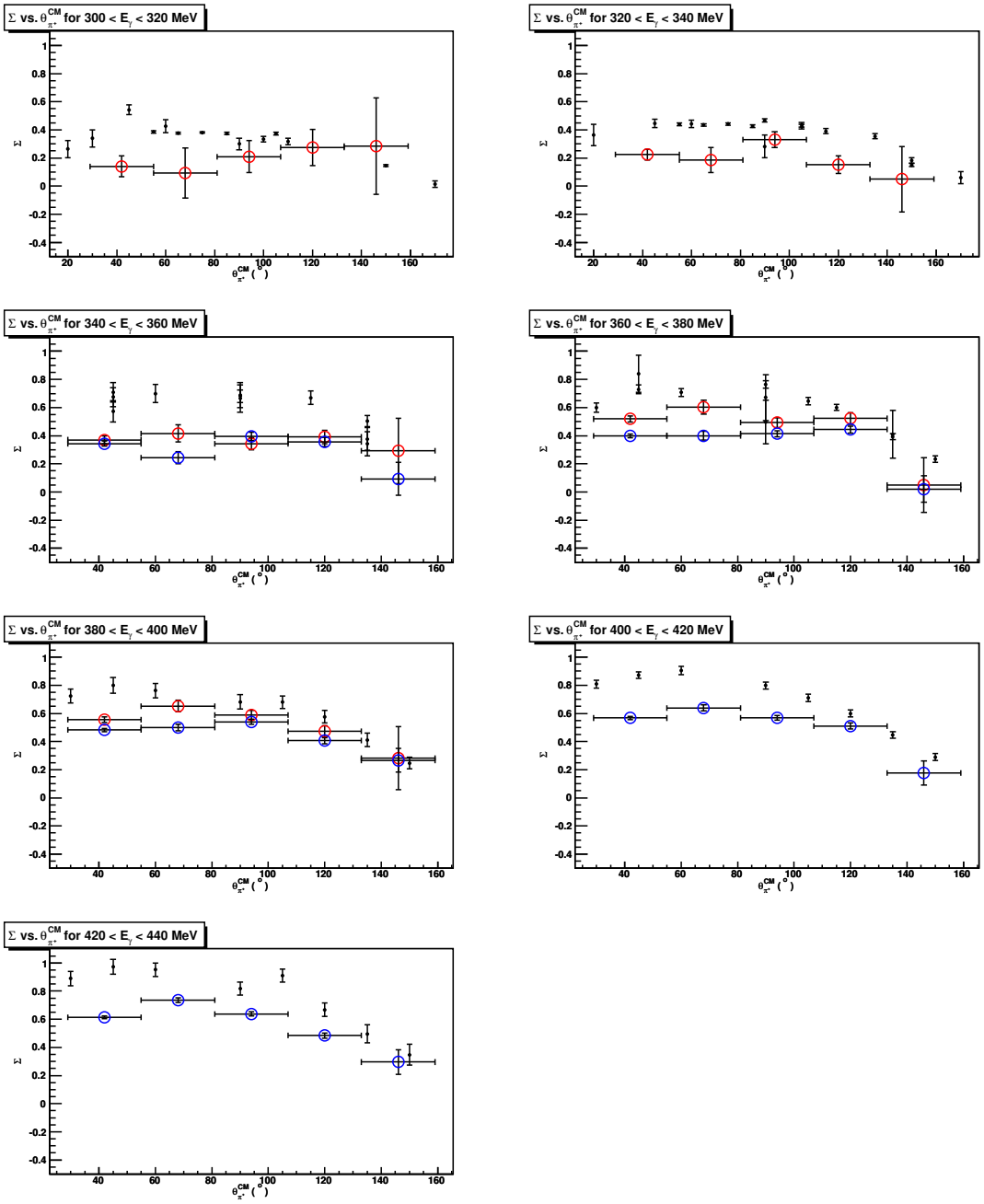

Figure 6.17: Comparisons of this work with previous existing data.
This plot is similar to Fig. (2.1) but with all previous measurements now shown solely in black. The results of this work have been added in red (for the 400MeV data) and blue (for the 440 MeV data) and statistical errors only are shown.

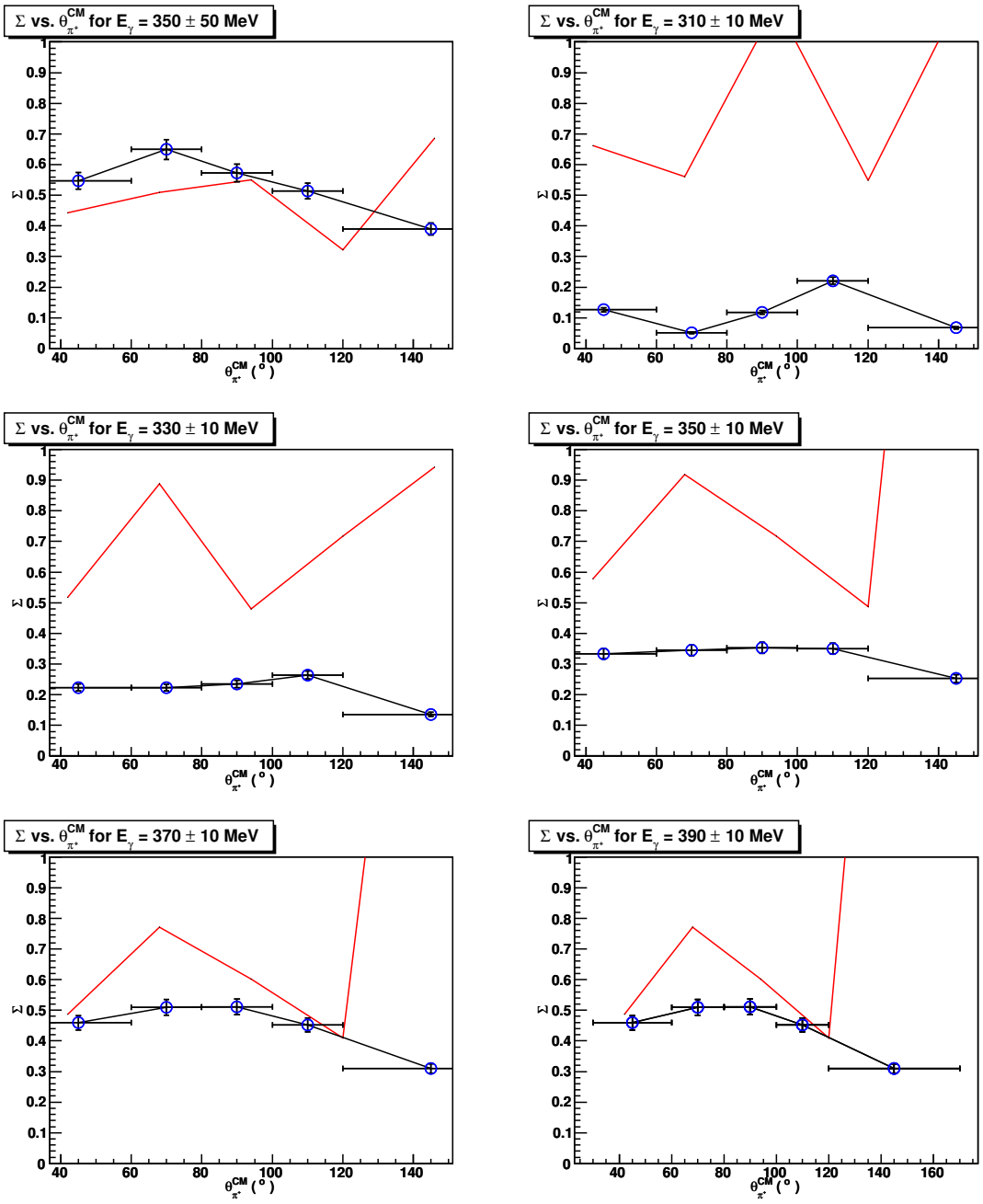

Figure 6.18: Comparisons of the 400 MeV data set (blue points) with the SAID-produced MC data (red line) run through an identical analysis setup. Omitted SAID points indicate that an asymmetry could not be deterimined due to insufficient statistics in the simulated data set.

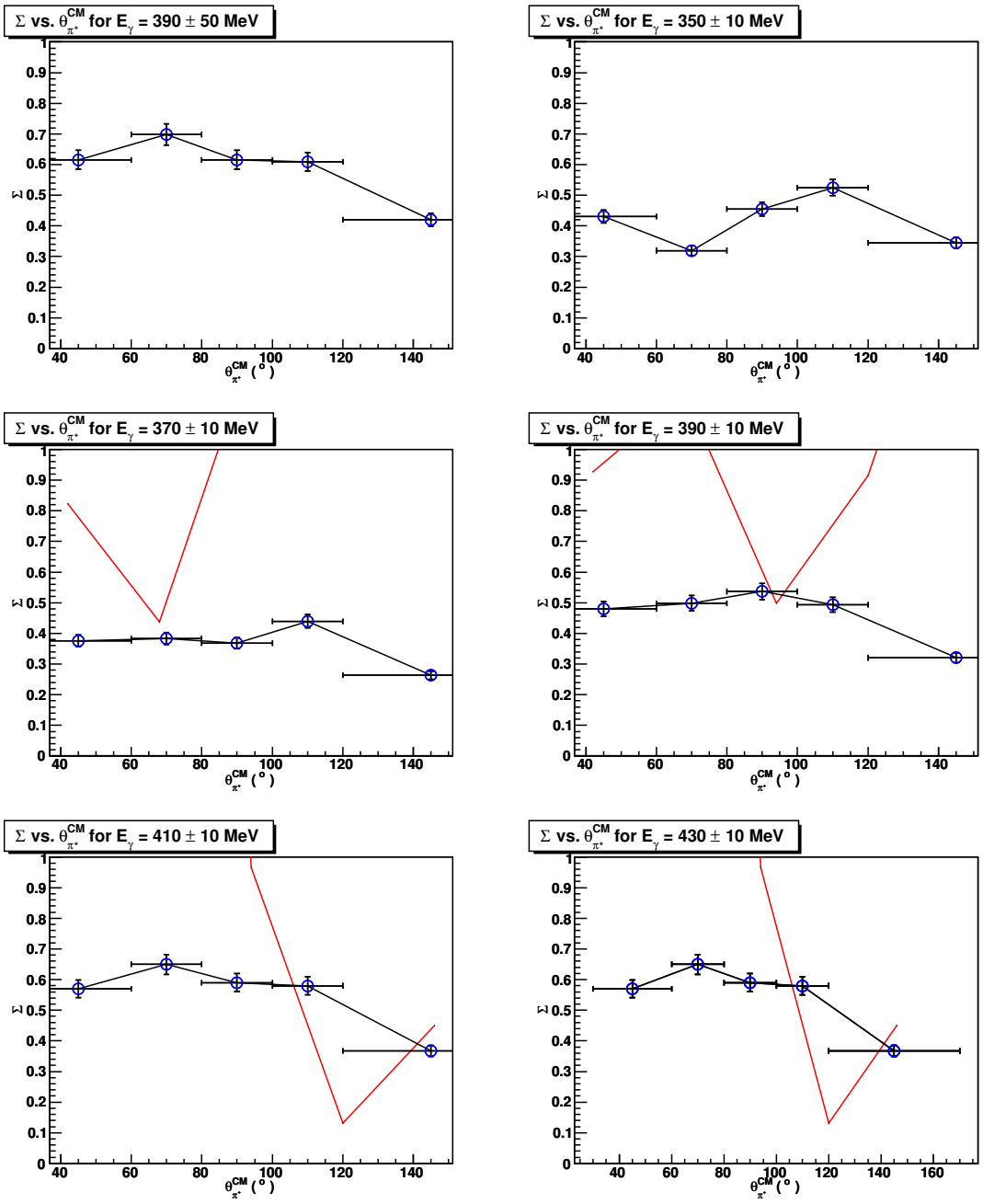

Figure 6.19: Comparisons of the 440 MeV data set (blue points) with the SAID-produced MC data (red line) run through an identical analysis setup. Omitted SAID points indicate that an asymmetry could not be deterimined due to insufficient statistics in the simulated data set.

6.5 Conclusions

In terms of being the first use of the CB for the detection of charged pions, the experiment was a resounding success as the final state required relied on being able to detect the charged pion in order to tag the coincident neutron. Other experiments requiring the detection of charged-meson final states have been, and are due to be, performed by the A2 collaboration which have potential to yield results of great scientific interest.

The results for Σ from $\overrightarrow{\gamma}p \rightarrow \pi^+ n$ are presently not in a form that can be submitted to the MAID and SAID databases. In order for the current analysis to yield such results, further analysis is required, especially when binning the data in terms of incident photon energy. The data do show great promise over larger energy binning ranges, agreeing for the most part with the MAID and SAID fits to current data.

The initial experimental brief highlighted the advantage of utilising the full solid angular acceptance. This unfortunately was not fully realised due to the distribution of experimental statistics. An increase in statistics would be required in order to extend this analysis to the extremes of $\theta_{\pi^+}^{CM}$, but in the current experimental climate, it is unlikely that extra beam-time would be allocated for such a venture. As such this aspect may have to go unaddressed in the immediate future.

It would be a distinct advantage if the degree of linear polarisation P could be better determined. A cause of the erroneous polarisation could be due to the ANB fit to the experimental data. Again, extra beam-time would be of use as the photon Tagger was upgraded during the period in which the analysis work for this experiment was performed and now does not exhibit the reduced data collection that afflicted the E_γ range of interest in the current work. As such, a better agreement of the ANB calculation with the data could be obtained and thus a more accurate value of P obtained with which to scale a high-statistics value of A by to obtain an accurate and precise value for Σ.

The internal consistency of the data is fairly good. The energy ranges of the two data sets overlapped between 340 and 400 MeV and in some places the data points are almost exactly coincident. This is as to be expected, the normalisation processes being identical for both data sets.

Comparisons of the results presented with those of previous experiments show that this work exhibits a significant statistical improvement on some of the previous measurements especially at higher incident

photon energies. Thus, when the analysis has been improved these measurements will provide more precise values of Σ over these energy ranges than have been measured before.

Appendix A

The Pion Threshold

A derivation for the pion threshold is given in general terms, the difference in threshold energy between charged and neutral pion production being highlighted.

A.1 The Pion Threshold

The general case of real-photon induced, one-nucleon knock-out pion production reaction on a nuclear target material X is described by

$$\gamma + X \rightarrow N + \pi \tag{A.1}$$

The threshold for such a reaction is given in terms of the energy required, expressed in natural units, by

$$E_{threshold} = \frac{E_{CM}^2 - m_X^2}{2m_X} \tag{A.2}$$

with

$$E_{CM}^2 = W^2 \tag{A.3}$$

This relation requires

$$W^2 = (E_{lab.} + m_X)^2 - \mathbf{p}_{lab.}^2 \tag{A.4}$$

which in turn expands to

$$W^2 = E_{lab.}^2 + 2E_{lab.}m_{target} + m_X^2 - \mathbf{p}_{lab.}^2 \tag{A.5}$$

which, due to the fact that

$$E_{lab.}^2 = m_{beam}^2 + \mathbf{p}_{lab.}^2 \tag{A.6}$$

yields, using eqn. (A.3):

$$E_{CM}^2 = 2m_X E_{lab.} + m_{beam}^2 + m_X^2 \tag{A.7}$$

For the case of threshold pion photo-production on the proton $m_{beam} = 0$, $m_X = m_p$, $E_{CM} = E_{\pi N}$ and $E_{lab.} = E_{threshold}$, thus giving (A.8):

$$E_{threshold} = \frac{E_{\pi N}^2 - m_p^2}{2m_p} \tag{A.8}$$

$E_{threshold}$ is equal to the minimum incident E_γ required to produce the πN final state. For the reaction $\gamma + X \rightarrow N + \pi$, $E_{\pi N}$ is equal to $(m_\pi + m_N)$. Thus, for positive pion photo-production on hydrogen, eqn. (3.3) becomes

$$E_{threshold} = \frac{(m_\pi + m_N)^2 - m_{target}^2}{2m_{target}} \tag{A.9}$$

As mentioned in Section ,eqn. A.9 yields values of $E_{threshold} = 151.4$ MeV for the $\gamma + p \rightarrow n + \pi^+$ reaction and $E_{threshold} = 144.7$ MeV for $\gamma + p \rightarrow p + \pi^0$.

Appendix B

DAQ Glossary

The main electronics and data acquisition (DAQ) components are presented here and their prominent features discussed in order that those unfamiliar with the experimental setup are not left confused when abbreviations are referred to, and also so that repetition is kept to a minimum.

CAMAC 'Computer Automated Measurement And Control' [70] was used for large sections of the data control and transfer systems for the CB apparatus components.

CATCH An acronym for 'Compass Accumulation, Transfer and Control Hardware', CATCH [71] was chosen as the standard for the Time-to-Digital Converters (TDCs) because of their timing characteristics and compatibility. They each contain a free-running internal clock (a 10GHz oscillator) which gives a timing resolution of 75ps (high resolution) or 150ps (low res.). The CATCH TDCs are controlled by a CERN-standard Trigger Control System which forces their readout when an experimental trigger is received by a reference TDC also connected to the CATCH system. TDCs of this type were used for the PID, CB and MWPC wires.

FASTBUS The control system used for the Focal Plane Detector TDCs [72]. These are the Time-to-Digital Converters (TDCs) used to transfer the signals from the individual Tagger Focal Plane Detector elements into the digital signals required in the DAQ systems. They are fast, multi-hit devices capable of coping with count rates of up to 1MHz. The overall function of FASTBUS is similar to CAMAC.

FIADC64 64-bit Fast Integrating Analogue-to-Digital Converters [73] as used for the PID and MWPC's strip readouts.

SADCs These are the 40 MHz Sampling ADCs used for the CB and MWPC readouts [74] . They were chosen as they have the capability to perform dynamic pedestal subtraction to extract just the pure signal. This is done using three sampling regions, the pedestal, the main signal and the tail. Attainable energy resolution is improved by subtracting the pedestal (remnant light in the detector crystals) and the tail (residual charge in the ADC) from the main signal.

VME Standing for 'Versa-Module Eurocard', VME [75] is a high speed data transfer bus system. In the Crystal Ball @ MAMI experiments, it was used for the CB and TAPS ADC readouts and the Tagger TDC readout.

Appendix C

Theory of Coherent Bremsstrahlung

Coherent Bremstrahlung is produced by the transfer of momentum from a charge-carrying entity to the lattice of a crystalline structure. In the case of real photon experiments these are the accelerator's electron beam and the crystalline radiator it is incident upon. The following discussion highlights the important kinematic relations underlying the process.

C.1 Coherent Bremsstrahlung Kinematics

The interaction of an electron with a material can be described thus:

$$e + X \rightarrow e' + X + \gamma \tag{C.1}$$

where e and e' are the incident and energy-degraded electrons, X represents the scattering nucleus of the material and γ is the Bremsstrahlung photon. The kinematics of the reaction are described by

$$E_0 = E + k \tag{C.2}$$

where E_0 and E are the initial and final electron energies and k is the Bremsstrahlung photon energy, and

$$\mathbf{p_0} = \mathbf{p} + \mathbf{q} + \mathbf{k} \tag{C.3}$$

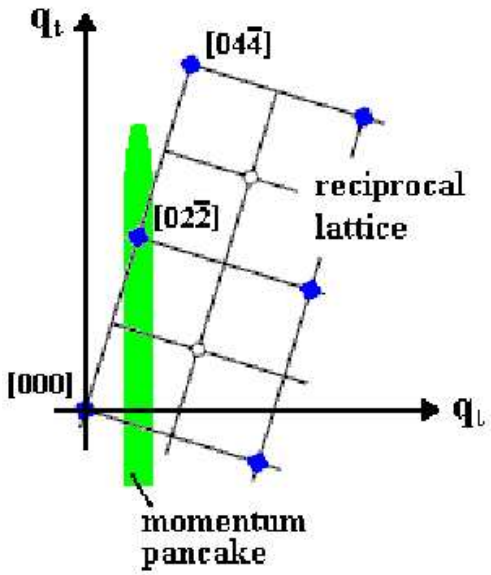

Figure C.1: The momentum 'pancake' showing the reciprocal lattice. Reciprocal lattice vectors that lie within the pancake will appear as pronounced enhancements on the Bremsstrahlung spectrum.

where $\mathbf{p_0}$ and $\mathbf{p}$ are the initial and final electron momenta, $\mathbf{q}$ is the momentum transferred to the lattice of a crystalline radiating material, and $\mathbf{k}$ is the momentum of the emitted Bremsstrahlung photon.

Due to the nature of crystals, $\mathbf{q}$ is limited [76] to a small region of momentum-space defined by the limits

$$\delta \leq q_l \leq 2\delta \tag{C.4}$$

and

$$0 \leq q_t \leq 2x \tag{C.5}$$

where q_l and q_t are the longitudinal and transverse components of $\mathbf{q}$. δ in eqn. C.4 the is minimum longitudinal momentum, $\delta \sim \left(\frac{2\pi}{a}\right)$ with a being the crystal lattice constant. x in eqn. C.5 is the quantum energy equal to $\frac{k}{E_0}$. This region is known as the 'momentum pancake' and is shown in Fig. C.1 which also illustrates the momentum pancake in relation to the reciprocal lattice of a crystal. As the momentum pancake moves through momentum space (by having the photon energy, E_0, increase), different crystal planes and lattice vectors contribute to the spectra leading to the discrete enhancements on a plot of *Intensity vs.* E_γ plot such as that shown in Fig. 4.4.1.

Appendix D

Two-body Kinematics

Two-body kinematics are primarily used for determining the energy of a π^+ at a given value of $\theta_{\pi^+}^{CM}$ in order to select the neutral cluster corresponding to the π^+'s coincident neutron in the analysis of the $\overrightarrow{\gamma}p \rightarrow \pi^+ n$ experiment (see Section 5.4.2). They were also utilised in the energy calibration of the CB, . The general principles as they apply to both uses of two-body kinematics in this work - the energy calibration of the CB and identifying the final state of interest - are covered here for reference.

D.1 Two-body Kinematics Overview

A general two-body photo-reaction is illustrated in figure D.1. From this, we can define several general kinematic relations:

$$\epsilon = E_\gamma + M_T \tag{D.1}$$

$$p_\gamma = E_\gamma \tag{D.2}$$

$$A = \epsilon^2 - p_\gamma^2 \tag{D.3}$$

- ϵ, from (D.1), is effectively the input energy to the system, equal to the incident photon energy, plus m_T, the target rest-mass energy. It limits which reactions are possible in any given experiment.

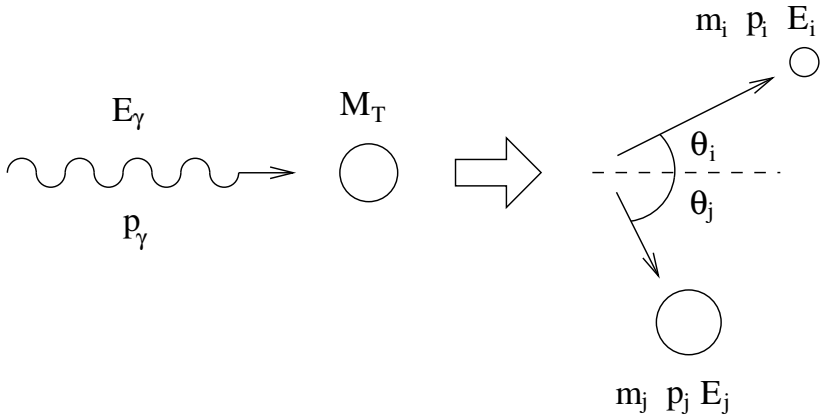

Figure D.1: Schematic diagram of a two-body reaction induced by a real photon incident on a stationery target.

- Eqn. (D.2) is true if the incident particle is a photon.
- (D.3) yields A, equivalent to E_{CM}^2, measured in natural units. It is a useful quantity to know as it can be used to check that all expected reaction products have been detected.

The following set of equations have equivalent expressions for each of the two outgoing particles, denoted i and j. For clarity, only one set will be presented here.

$$\epsilon_i = m_i + \sqrt{p_\gamma^2 + m_j^2} \tag{D.4}$$

$$d_i = m_i^2 - m_j^2 + A \tag{D.5}$$

$$c_i = m_i^2 \epsilon^2 - \frac{1}{4} d_i^2 \tag{D.6}$$

$$B_i = d_i p_\gamma \tag{D.7}$$

$$b_i = B_i \cos\theta_i \tag{D.8}$$

$$a_i = \epsilon^2 - p_\gamma^2 \cos^2\theta_i \tag{D.9}$$

The momentum is given by:

$$p_i = \frac{b_i + \sqrt{b_i^2 - 4a_i c_i}}{2a_i} \tag{D.10}$$

and from this the energy can be calculated:

$$E_i^2 = p_i^2 + m_i^2 \tag{D.11}$$

It should be noted that due to the energy ranges used during the conduction of the experiment and investigated in the subsequent analysis, threshold region phenomena are not observed. Just above the charged pion threshold of 151.4 MeV, up to incident photon energies of 162.2 MeV, the limiting of emission angles to a small cone in the forward direction is observed. The loci described by the momentum vectors is responsible for this responsible for this [77]. above this energy, the pion can populate all values of θ, thus reaction products appear to populate the whole solid angle.

D.2 E_{π^+} Determination for $\pi^+ n$ Final-state Discrimination

When used for identifying the neutron, i and j as appearing in eqns. (D.4) to (D.11) were chosen to be the pion and the neutron respectively. Entering values for the target mass (proton), residual mass (neutron), M_{π^+}, E_γ and θ_{π^+}(lab.), the above equations were used to return values for the energy of the pion. In this way, the pion energy loss can be eliminated as, even if the particle does lose energy during its passage towards the detectors, the angle of its trajectory is unaffected as the spectrometers are not magnetic. From the information available, the energy and angle of the neutron can also be easily returned.

D.3 CB Calibration: $\gamma p \rightarrow \pi^0 p$

The same two-body kinematic relations were used for calibrating the Crystal Ball, this time using the $\gamma p \rightarrow p\pi^0$ reaction, a diagram of which can be seen in figure D.2. For the purposes of the CB calibration, performed by J. Brudvik of UCLA [59], the relation

$$E_{\pi^0} = \frac{2p_\gamma p_{\pi^0} \cos\theta_{\pi^0} + 2p_\gamma m_T + m_{\pi^0}^2}{2\epsilon} \tag{D.12}$$

was used.

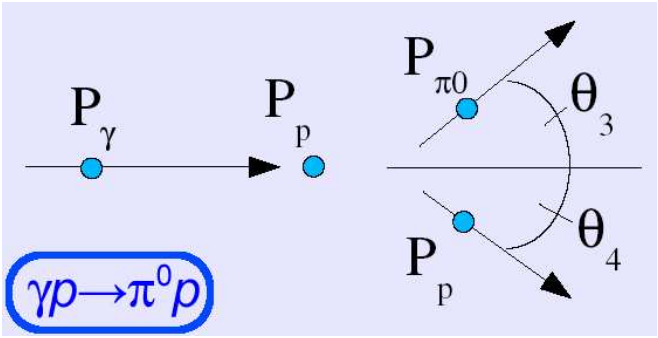

Figure D.2: The kinematics of $\gamma \rightarrow p\pi^0$.

Appendix E

The Extraction of Σ from a $\cos(2\phi)$ Distribution

The extraction of Σ from a $\cos(2\phi)$ asymmetry distribution is discussed here with reference to the unpolarised cross section, to which the orthogonal linearly polarised cross-sections are related.

E.1 Determining Σ

From Section 5.5.3 the photon beam asymmetry Σ is related to the amplitude, A, of a $\cos(2\phi)$ fit by the relation

$$\Sigma = \frac{A}{P} \tag{E.1}$$

For linearly polarised photons with the orientations $\parallel$ and $\perp$, eqn. E.1 becomes:

$$\Sigma = \frac{A}{\left(\frac{2P_{\perp}P_{\parallel}}{P_{\perp}+P_{\parallel}}\right)} \tag{E.2}$$

From Section 3.3, the polarised cross section relates to the unpolarised section as follows:

$$\sigma_{pol} = \sigma_0 \left[1 + A\cos\left(2\phi - \phi_0\right)\right] \tag{E.3}$$

Re-writing E.3 using $A = \Sigma P$:

$$\sigma_{pol} = \sigma_0 \left[1 + \Sigma P \cos\left(2\phi - \phi_0\right)\right] \tag{E.4}$$

Hereon in, the phase term ϕ_0 will be omitted for clarity.

For linearly polarised photons, the parallel and perpendicular cross-sections are given by

$$\sigma_{\parallel} = \sigma_0 \left[1 - \Sigma P_{\parallel} \cos\left(2\phi\right)\right] \tag{E.5}$$

and

$$\sigma_{\perp} = \sigma_0 \left[1 + \Sigma P_{\perp} \cos\left(2\phi\right)\right] \tag{E.6}$$

The photon asymmetry is then defined as

$$\Sigma = \frac{\sigma_{\parallel} - \sigma_{\perp}}{\sigma_{\parallel} + \sigma_{\perp}} \tag{E.7}$$

In order to construct a meaningful asymmetry, both quantities - in this case $\sigma_{\parallel}$ and $\sigma_{\perp}$ - must have the same number of statistics. Due to the nature of data collection it is highly unlikely that this will be exactly the case, and so the distributions must be scaled to each other. Looking at the number of events in the polarised cross-section, equations E.5 and E.6 can be re-written as

$$N_{\parallel}\left(\phi\right) = N_0 \left[1 + \Sigma P_{\parallel} \cos\left(2\phi\right)\right] \tag{E.8}$$

$$N_{\perp}\left(\phi\right) = N_0 \left[1 - \Sigma P_{\perp} \cos\left(2\phi\right)\right] \tag{E.9}$$

In order to ensure that the sample sizes of each of the polarised cross-sections are equal, one is scaled by the polarisation and number of events of the other. This yields

$$N_{\perp} P_{\perp} \sigma_{\parallel} = N_{\perp} P_{\perp} N_0 \left[1 + \Sigma P_{\parallel} \cos\left(2\phi\right)\right] = G_{\parallel}\left(\phi\right) \tag{E.10}$$

$$N_{\parallel} P_{\parallel} \sigma_{\perp} = N_{\parallel} P_{\parallel} N_0 \left[1 - \Sigma P_{\perp} \cos\left(2\phi\right)\right] = G_{\perp}\left(\phi\right) \tag{E.11}$$

The asymmetry can now be expressed as

$$Asym. = \frac{G_{\parallel}(\phi) - G_{\perp}(\phi)}{G_{\parallel}(\phi) + G_{\perp}(\phi)} \tag{E.12}$$

Multiplying out E.10 and E.11:

$$G_{\parallel}(\phi) = N_{\perp}P_{\perp}N_{\parallel}N_0 + N_{\perp}P_{\perp}N_{\parallel}N_0\Sigma P_{\parallel}\cos(2\phi) \tag{E.13}$$

$$G_{\perp}(\phi) = N_{\parallel}P_{\parallel}N_{\perp}N_0 - N_{\parallel}P_{\parallel}N_{\perp}N_0\Sigma P_{\perp}\cos(2\phi) \tag{E.14}$$

gives, cancelling the common factor of $N_{\parallel}N_{\perp}N_0$:

$$Asym. = \frac{P_{\perp} + P_{\perp}\Sigma P_{\parallel}\cos(2\phi) - P_{\parallel} + P_{\parallel}\Sigma P_{\perp}\cos(2\phi)}{P_{\perp} + P_{\perp}\Sigma P_{\parallel}\cos(2\phi) + P_{\parallel} - P_{\parallel}\Sigma P_{\perp}\cos(2\phi)} \tag{E.15}$$

Eqn E.15 then re-arranges to its final form of

$$Asym. = \frac{P_{\parallel} - P_{\perp}}{P_{\parallel} + P_{\perp}} + \frac{2P_{\perp}P_{\parallel}}{P_{\perp} + P_{\parallel}}\Sigma\cos(2\phi) \tag{E.16}$$

It can be seen by comparing eqn. to an asymmetry fitted with a $\cos(2\phi)$ function, the term $\frac{P_{\parallel}-P_{\perp}}{P_{\parallel}+P_{\perp}}$ is the observed offset and should be approximately equal to zero, exactly equalling zero if $P_{\parallel} = P_{\perp}$. The factor $\frac{2P_{\perp}P_{\parallel}}{P_{\perp}+P_{\parallel}}$ allows Σ to be extracted as in eqn. E.1.

Appendix F

Results Tables

Below are presented the values of Σ obtained from the analysis of the experimental data collected. The results are listed by E_γ and $\theta_{\pi^+}^{CM}$ for each data set to allow for easy perusal, the values coming from Figures 6.7 and 6.14. A table of results for the overlapping data follows the main results tables, the values being extracted from Fig. 6.15.

E_γ(MeV)	$\theta_{\pi^+}^{CM}$ (°)	$\Sigma \pm \delta\Sigma_{stat.} \pm \delta\Sigma_{sys.}$
310 ± 10	45 ± 15	0.126281 ± 0.030410 ± 0.006314
	70 ± 10	0.051088 ± 0.080013 ± 0.002554
	90 ± 10	0.117967 ± 0.057005 ± 0.005898
	110 ± 10	0.220950 ± 0.047641 ± 0.011048
	145 ± 25	0.067131 ± 0.069702 ± 0.003357
330 ± 10	45 ± 15	0.223478 ± 0.014983 ± 0.011174
	70 ± 10	0.222676 ± 0.037949 ± 0.011134
	90 ± 10	0.234705 ± 0.027871 ± 0.011735
	110 ± 10	0.264206 ± 0.023413 ± 0.013210
	145 ± 25	0.135279 ± 0.036436 ± 0.006764
350 ± 10	45 ± 15	0.333384 ± 0.011130 ± 0.016669
	70 ± 10	0.344667 ± 0.026429 ± 0.017233
	90 ± 10	0.353151 ± 0.020080 ± 0.017658
	110 ± 10	0.350631 ± 0.017867 ± 0.017532
	145 ± 25	0.252550 ± 0.028886 ± 0.012627
370 ± 10	45 ± 15	0.458974 ± 0.009291 ± 0.022949
	70 ± 10	0.509476 ± 0.020641 ± 0.025474
	90 ± 10	0.510959 ± 0.016630 ± 0.025548
	110 ± 10	0.451919 ± 0.015254 ± 0.022596
	145 ± 25	0.309762 ± 0.025397 ± 0.015488
390 ± 10	45 ± 15	0.588516 ± 0.008804 ± 0.029426
	70 ± 10	0.684594 ± 0.018660 ± 0.034230
	90 ± 10	0.617452 ± 0.015495 ± 0.030873
	110 ± 10	0.557307 ± 0.014549 ± 0.027865
	145 ± 25	0.427317 ± 0.026457 ± 0.021366

Table F.1: Results listed in terms of E_γ for the 400 MeV data, as plotted on Fig. (6.7).

$\theta_{\pi^+}^{CM}$ (°)	E_γ(MeV)	$\Sigma \pm \delta\Sigma_{stat.} \pm \delta\Sigma_{sys.}$
45 ± 15	310 ± 10	0.126281 ± 0.030410 ± 0.006314
	330 ± 10	0.223478 ± 0.014983 ± 0.011174
	350 ± 10	0.333384 ± 0.011130 ± 0.016669
	370 ± 10	0.458974 ± 0.009291 ± 0.022949
	390 ± 10	0.588516 ± 0.008804 ± 0.029426
70 ± 10	310 ± 10	0.051088 ± 0.080013 ± 0.002554
	330 ± 10	0.222676 ± 0.037949 ± 0.011134
	350 ± 10	0.344667 ± 0.026429 ± 0.017233
	370 ± 10	0.509476 ± 0.020641 ± 0.025474
	390 ± 10	0.684594 ± 0.018660 ± 0.034230
90 ± 10	310 ± 10	0.117967 ± 0.057005 ± 0.005898
	330 ± 10	0.234705 ± 0.027871 ± 0.011735
	350 ± 10	0.353151 ± 0.020080 ± 0.017658
	370 ± 10	0.510959 ± 0.016630 ± 0.025548
	390 ± 10	0.617452 ± 0.015495 ± 0.030873
110 ± 10	310 ± 10	0.220950 ± 0.047641 ± 0.011048
	330 ± 10	0.264206 ± 0.023413 ± 0.013210
	350 ± 10	0.350631 ± 0.017867 ± 0.017532
	370 ± 10	0.451919 ± 0.015254 ± 0.022596
	390 ± 10	0.557307 ± 0.014549 ± 0.027865
145 ± 25	310 ± 10	0.067131 ± 0.069702 ± 0.003357
	330 ± 10	0.135279 ± 0.036436 ± 0.006764
	350 ± 10	0.252550 ± 0.028886 ± 0.012627
	370 ± 10	0.309762 ± 0.025397 ± 0.015488
	390 ± 10	0.427317 ± 0.026457 ± 0.021366

Table F.2: Results listed in terms of θ_{π^+} for the 400 MeV data, as plotted on Fig. (6.7).

E_γ(MeV)	$\theta_{\pi^+}^{CM}$ (°)	$\Sigma \pm \delta\Sigma_{stat.} \pm \delta\Sigma_{sys.}$
350 ± 10	45 ± 15	0.430647 ± 0.023544 ± 0.021532
	70 ± 10	0.319580 ± 0.057370 ± 0.015979
	90 ± 10	0.454306 ± 0.043723 ± 0.022715
	110 ± 10	0.525108 ± 0.037543 ± 0.026255
	145 ± 25	0.345117 ± 0.057876 ± 0.017256
370 ± 10	45 ± 15	0.375725 ± 0.013557 ± 0.018786
	70 ± 10	0.383245 ± 0.030723 ± 0.019162
	90 ± 10	0.368078 ± 0.024954 ± 0.018404
	110 ± 10	0.439569 ± 0.022270 ± 0.021978
	145 ± 25	0.263145 ± 0.034889 ± 0.013157
390 ± 10	45 ± 15	0.479694 ± 0.011928 ± 0.023985
	70 ± 10	0.498566 ± 0.025916 ± 0.024928
	90 ± 10	0.536710 ± 0.021579 ± 0.026835
	110 ± 10	0.493468 ± 0.019848 ± 0.024673
	145 ± 25	0.320434 ± 0.032895 ± 0.016022
410 ± 10	45 ± 15	0.569551 ± 0.010980 ± 0.028478
	70 ± 10	0.649444 ± 0.022526 ± 0.032472
	90 ± 10	0.589795 ± 0.019676 ± 0.029490
	110 ± 10	0.579642 ± 0.018676 ± 0.028982
	145 ± 25	0.367499 ± 0.032374 ± 0.018375
430 ± 10	45 ± 15	0.627851 ± 0.009727 ± 0.031393
	70 ± 10	0.751253 ± 0.018702 ± 0.037563
	90 ± 10	0.640407 ± 0.017227 ± 0.032020
	110 ± 10	0.585144 ± 0.016936 ± 0.029257
	145 ± 25	0.441172 ± 0.031607 ± 0.022059

Table F.3: Results listed in terms of E_γ for the 440 MeV data, as plotted on Fig. (6.14).

$\theta_{\pi^+}^{CM}$ (°)	E_γ(MeV)	$\Sigma \pm \delta\Sigma_{stat.} \pm \delta\Sigma_{sys.}$
45 ± 15	350 ± 10	0.430647 ± 0.023544 ± 0.021532
	370 ± 10	0.375725 ± 0.013557 ± 0.018786
	390 ± 10	0.479694 ± 0.011928 ± 0.023985
	410 ± 10	0.569551 ± 0.010980 ± 0.028478
	430 ± 10	0.627851 ± 0.009727 ± 0.031393
70 ± 10	350 ± 10	0.319580 ± 0.057370 ± 0.015979
	370 ± 10	0.383245 ± 0.030723 ± 0.019162
	390 ± 10	0.479694 ± 0.011928 ± 0.023985
	410 ± 10	0.649444 ± 0.022526 ± 0.032472
	430 ± 10	0.751253 ± 0.018702 ± 0.037563
90 ± 10	350 ± 10	0.454306 ± 0.043723 ± 0.022715
	370 ± 10	0.368078 ± 0.024954 ± 0.018404
	390 ± 10	0.536710 ± 0.021579 ± 0.026835
	410 ± 10	0.589795 ± 0.019676 ± 0.029490
	430 ± 10	0.640407 ± 0.017227 ± 0.032020
110 ± 10	350 ± 10	0.525108 ± 0.037543 ± 0.026255
	370 ± 10	0.439569 ± 0.022270 ± 0.021978
	390 ± 10	0.493468 ± 0.019848 ± 0.024673
	410 ± 10	0.579642 ± 0.018676 ± 0.028982
	430 ± 10	0.585144 ± 0.016936 ± 0.029257
145 ± 25	350 ± 10	0.345117 ± 0.057876 ± 0.017256
	370 ± 10	0.263145 ± 0.034889 ± 0.013157
	390 ± 10	0.320434 ± 0.032895 ± 0.016022
	410 ± 10	0.367499 ± 0.032374 ± 0.018375
	430 ± 10	0.441172 ± 0.031607 ± 0.022059

Table F.4: Results listed in terms of θ_{π^+} for the 440 MeV data, as plotted on Fig. (6.14).

E_γ (MeV)	$\theta_{\pi^+}^{CM}$ (°)	Σ_{400MeV}	Σ_{440MeV}
350 ± 10	45 ± 15	0.333384 ± 0.020043	0.430647 ± 0.031906
	70 ± 10	0.344667 ± 0.136305	0.319580 ± 0.059554
	90 ± 10	0.353151 ± 0.026739	0.454306 ± 0.049271
	110 ± 10	0.350631 ± 0.025032	0.525108 ± 0.045813
	145 ± 25	0.252550 ± 0.031526	0.345117 ± 0.060394
E_γ (MeV)	$\theta_{\pi^+}^{CM}$ (°)	Σ_{400MeV}	Σ_{440MeV}
370 ± 10	45 ± 15	0.458974 ± 0.024758	0.375725 ± 0.023167
	70 ± 10	0.509476 ± 0.114760	0.383245 ± 0.223955
	90 ± 10	0.510959 ± 0.030484	0.368078 ± 0.031007
	110 ± 10	0.451919 ± 0.027263	0.439569 ± 0.031289
	145 ± 25	0.309762 ± 0.029747	0.263145 ± 0.037287
E_γ (MeV)	$\theta_{\pi^+}^{CM}$ (°)	Σ_{400MeV}	Σ_{440MeV}
390 ± 10	45 ± 15	0.588516 ± 0.030715	0.479694 ± 0.026787
	70 ± 10	0.684594 ± 0.105726	0.498566 ± 0.186154
	90 ± 10	0.617452 ± 0.034543	0.536710 ± 0.034436
	110 ± 10	0.557307 ± 0.031435	0.493468 ± 0.031666
	145 ± 25	0.427317 ± 0.034007	0.320434 ± 0.036589

Table F.5: Comparisons between Σ for the overlapping regions of the two polarised photon data sets. Values of $\delta\Sigma$ include statistical and systematic uncertainties, as plotted on Fig. (6.15).

Bibliography

[1] S. Eidelman et al. *Review of Particle Physics*, volume 592. July 2004.

[2] N. Bianchi et al. Total Hadronic Photoapsorption Cross-section on Nuclei in the Nucleon Resonance Region. *Phys. Rev. C*, 54(4), October 1996.

[3] T.A. Armstrong et al. Total Hadronic Cross Section of γ Rays in Hydrogen in the Energy Range 0.365-4.215 GeV. *Phys. Rev. D*, 5(7), 1 April 1972.

[4] MAID: Photo- and Electroproduction of Pions, Etas and Kaons on the Nucleon. http://www.kph.uni-mainz.de/MAID.

[5] D. Dreschel, O. Hanstein, S.S. Kamalov and L. Tiator. A Unitary Isobar Model for Pion Photo- and Electro-production on the Proton up to 1 GeV. *Nuclear Physics A*, 645, 1999.

[6] R.A. Arndt, W.J. Briscoe, I.I. Strakovsky and R.L.Workman. Analysis of Pion Photoproduction Data. *Phys. Rev. C*, 66(055213), November 2002.

[7] CNS DAC Service Partial-Wave Analysis Facility (SAID). http://gwdac.phys.gwu.edu.

[8] D. Watts. Lectures given at the UK EPSRC Summer School, Chester. http://www.ph.ed.ac.uk/ dwatts1/EPSRCSumSchChester.pdf, September 2005.

[9] L.S. Cardman. Photon Tagging. Present Practice and Future Prospects. *Report Presented at the Magnetic Spectrometer Workshop, Williamsbugh, VA*, October 1983.

[10] A.W. Sáenz and H. Überall. Coherent Bremsstrahlung at Low Energies. *Physical Review B*, 25(7), April 1982.

[11] A. D'Angelo et al. Generation of Comton Backscattering γ-ray Beams. *Nuclear Instruments and Methods in Physics Research*, A(455), 2000.

[12] I.S. Barker, A. Donnachie and J.K.Storrow. Complete Experiments in Pseudoscalar Photoproduction. *Nuclear Physics*, B(95), 21 April 1975.

[13] R.E. Taylor and R.F. Mozley. Positive Pion Production by Polaised Bremsstrahlung. *Phys. Rev.*, 117(3), February 1 1960.

[14] R.C. Smith and R.F. Mozley. Positive Pion Production by Polarized X Rays between 227 and 373 MeV. *Phys. Rev.*, 130(6), 15 June 1963.

[15] V.A. Get'man et al. Positive pion production from polarized protons by linearly polarized photons in the energy range 280-420 MeV. *Nucl. Phys. B*, 188:397–413, 1981.

[16] G. Audit et al. DAPHNE: A Large-acceptance Tracking Detector for the Study of Photoreactions at Intermediate Energies. *Nuclear Instruments and Methods in Physics Research*, A(301), 1991.

[17] R. Beck et al. Determination of the $E2/M1$ ratio in the $\gamma N \rightarrow \Delta(1232)$ transition from a simultaneous measurement of $p(\overrightarrow{\gamma},p)\pi^0$ and $p(\overrightarrow{\gamma},\pi^+)n$. *Phys. Rev. C*, 61(14):035204, Feb 2000.

[18] G. Blanpied et al. $N \rightarrow \Delta$ transition and proton polarisabilities from measurements of $p(\overrightarrow{\gamma},\gamma)$, $p(\overrightarrow{\gamma},\pi^o)$, and $p(\overrightarrow{\gamma},\pi^+)$. *Phus. Rev. C*, 64(1):025203, 2001.

[19] S. Boffi, C. Giusti, F.D. Pacati, M. Radici. *Electromagnetic Response of Atomic Nuclei.* Oxford Science Publications, 1996.

[20] T. Ericson and W. Weise. *Pions and Nuclei.* Oxford University Press, 1988.

[21] B. Krusche. Meson Photoproduction: Resonance Excitation. http://jazz.unibas.ch/ krusche/photoproduction-basics.html.

[22] G. Ecker and Ulf-G Meißner. What is a low-energy theorem? *arXiv:hep-ph/9409442*, 1994.

[23] S.Scherer, J.H.Koch, J.L. Friar. Systematics of Low-Energy Theorems for Pion Photo- and Electroproduction. *Nuclear Physics*, A(552), 1993.

[24] J.L. Friar and B.F Gibson. Exchange Currents in Nuceli, Threshold Pion Photoproduction from Nucleons, and the Equivalence Theorem. *Phys. Rev. C*, 15(5), May 1977.

[25] A.A. Chumbalov. Photoproduction of Pions off Nucleons and Nuclei. *Czech. J. Phys.*, B(39), 1989.

[26] H. Herminghaus, A. Feder, H. Kaiser, W. Manz, H. v.d. Schmitt. The Design of a Cascaded 800 MeV Normal Conducting C.W. Race Track Microtron. *Nuclear Instruments and Methods*, (138), 1976.

[27] A. Jankowiak. The Mainz Microtron MAMI - Past and Future. *European Physical Journal*, A(28), 2006.

[28] H. Herminghaus et al. Fisrt Operation of the 850 MeV Electron Accelerator 'MAMI'. *Proceedings of the Linear Accelerator Conference, Albequerque*, 1990.

[29] I. Anthony, J.D. Kellie, S.J. Hall, G.J. Miller, J. Ahrens. Design of a Tagged Photon Spectrometer for use with the Mainz 840 MeV Microtron. *Nuclear Instruments and Methods in Physics Research*, A(301), 1991.

[30] S.J. Hall, G.J. Miller, R. Beck, P. Jennewein. A Focal Plane System for the 855 MeV Tagged Photon Spectrometer at MAMI-B. *Nuclear Instruments and Methods in Physics Research*, A(368), 1996.

[31] U. Timm. Coherent Bremsstrahlung of Electrons in Crystals. *Fortschritte der Physik*, (17), 1969.

[32] K. Livingston. The Stonehenge Technique: A New Method of Crystal Alignment for Coherent Bremsstrahlung Experiments. *International Conference on Charged and Neutral Particle Channeling Phenomena, edited by Sultan B. Dabagov*, Proc. SPIE 5974, 2005.

[33] A. Natter, P. Grabmayr, T. Hehl, R.O. Owens and S. Wunderlich. ANB - Analytic Bremstrahlungs Calculation. http://www.pit.physik.uni-tuebingen.de/grabmayr/software/brems/brems-analytic.html.

[34] F. Rambo et al. Enhancement of the Linear Polarsiation of Coherent Bremsstrahlung by Collimation of the Photon Beam. *Phys. Rev. C*, 58(1), July 1998.

[35] K. Livingston. Linearly Polarised Photons at MAMI. Presentation at the 6th CB@MAMI collaboration meeting in Gießen, October 2004.

[36] A. Thomas. Crystal Ball Hydrogen (Deuterium) Target Manual, June 2004.

[37] V. Kashevarov. Private communication.

[38] E. Downie. First Year Ph.D Progress Report. Technical report, University of Glasgow, September 2003.

[39] ELGEN TECHNOLOGY. EJ-204 Plastic Scintillator. Technical report, PO Box 870, Crane Street, Sweetwater, TX 79556, USA.

[40] ELGEN TECHNOLOGY. Acrylic Plastic Light Guide Material. Technical report, PO Box 870, Crane Street, Sweetwater, TX 79556, USA.

[41] P. Pedroni, V. Lisin, S. Scumann. MWPC analysis code for AcquRoot. 2005.

[42] M. Kobayashi et al. Self-supporting Cylidrical Multiwire Proportional Chambers with Two-dimensional Read-out. *Nuclear Instruments and Methods in Physics Research*, A(245), 1986.

[43] B.M.K. Nefkens. The Crystal Ball. Technical report, UCLA, 1995.

[44] J.R.M. Annand. DAQ for Crystal Ball @ MAMI: Prototype ACQU Support for CATCH and CAEN VMEbus ADCs. Technical Report for the CB@MAMI Collaboration, November 2002.

[45] J.R.M. Annand, D. Hornidge, D. Krambrich, S. Schumann. Upgrade of the Crystal Ball Electronics. Technical report, Johannes Gutenburg Universität, Mainz, March 2002.

[46] D. Krambrich. Status of the Electronics for the Crystal Ball. Talk given at the fourth CB@MAMI collaboration meeting, Mainz, March 2004.

[47] R. Novotny et al. The BaF_2 Photon Spectrometer TAPS. *IEEE Trans. on Nucl. Sc.*, 38(2), April 1991.

[48] P. Drexler et al. The New Readout Electronics for the BaF_2 Calorimeter TAPS. *IEEE Transactions on Nuclear Science*, 50(4), August 2003.

[49] J.R.M. Annand. Data Analysis in an AcquRoot Framework. Instruction Manual for AcquRoot Users, December 2005.

[50] CERN. The CERN Program Library 'CERNLIB'. http://cernlib.cern.ch.

[51] R. Brun et al. ROOT: An Object-Oriented Data Analysis Framework. http://root.cern.ch.

[52] R. Gregor. DAQ for TAPS. Talk given at 3rd CB@MAMI ColMeeting in Mainz, January 2003.

[53] C. McGeorge. Private comminications, 2007 - 2008.

[54] K. Livingston. The Mainz Tagger in AcquRoot. Instruction Manual for AcquRoot Users, June 2004.

[55] J.C. McGeorge. Summary of Workings of tagcalv7c and Modifications in modv7c and modv7a. Private communication.

[56] A. Reiter, P.S. Lumsden, J. Ahrens, J.R.M. Annand, R.Beck, J.C. McGeorge, R.O. Owens. A Microscope for the Glasgow Phiton Tagging spectrometer in Mainz. *The European Physical Journal A*, 30(2), November 2006.

[57] A. Nikolaev. The Tagging Efficiency Measurements. Summary Report for the A2 Collaboration.

[58] E. Downie. Private comminication, 2004.

[59] J. Brudvik. PhD thesis, UCLA, 2007.

[60] M. Unverzagt. PhD thesis, Johannes Gutenburg Universität, Mainz, 2008.

[61] R. Gregor. PhD thesis, Justus Liebig Universität, Gießen, 2008.

[62] S. Lugert. PhD thesis, Justus Liebig Universität, Gießen, 2008.

[63] B. Boillat. PhD thesis, University of Basel, 2008.

[64] F. Zehr. PhD thesis, University of Basel, 2008.

[65] D. Watts. Magnetic Moment of the $\Delta^+(1232)$ via the $\gamma + p \rightarrow n + \pi^+ + \gamma'$ reaction. Talk given at the 5th CB@MAMI Collaboration Metting, Gießen, October 2007.

[66] T.D.S. Stanislaus et al. Measurement of Neutron Detection Efficiencies in NaI using the Crystal Ball Detector. *Nuclear Instruments and Methods in Physics Research*, A(462), 2001.

[67] E.J. Downie. *Radiative π^0 photoproduction in the region of the $\Delta(1232)$ resonance.* PhD thesis, University of Glasgow, 2007.

[68] K. Livingston. Private comminication, 2008.

[69] S. Agostinielli et al. GEANT4 - a Simulation Toolkit. *Nuclear Instruments & Methods in Physics Research*, A(506), 2003.

[70] An Introduction to CAMAC. http://www-esd.fnal.gov/esd/catalog/intro/introcam.htm.

[71] H. Fischer et al. Implementation of the dead-time free T1 TDC in the COMPASS detector readout. *IEEE Trans. on Nucl. Sc.*, A(461), 2001.

[72] IEEE standard FASTBUS modular high-speed data acquisition and control system and IEEE FASTBUS standard routines. *IEEE Std 960-1989, Std 1177-1989*, April 1990.

[73] Takahiro Fusayasu. A Fast Integrating ADC Using Precise Time-to-Digital Conversion. *IEEE Nuclear Science Symposium Conference Record*, 2007.

[74] i-tr0nics GmbH. Multi-channel Sampling Analogue-to-Digital Converter Module i-SACDC108032 for the Mainz Crystal Ball Detector. Technical report, October 2003.

[75] VME Technology. http://www.vita.com/vmefaq.html.

[76] H Überall. High-Energy Interference Effect of Bramsstrahlung and Pair Production in Crystals. *Physical Review*, 103(4), 1956.

[77] R. Owens. Private comminications, 2007 - 2008.